In situ mechanical analysis of sludge in hazardous environments

Tomas Fried

Lancaster University, Department of Engineering

A thesis submitted in accordance with the requirements of

Lancaster University for the degree of Doctor of Philosophy

October 2021

Abstract

In situ mechanical analysis of sludge in hazardous environments

Tomas Fried, October 2021

The Sellafield site is the focal point of nuclear decommissioning in the UK as it is made up of several hundred nuclear facilities built for a wide range of capabilities. These facilities are tightly packed in a very small area and are in various stages of their lifecycle. One of the biggest challenges is the presence of legacy storage tanks and silos that contain sludge of uncertain properties. The process of clean out and decommissioning of these vessels is informed by analysing the chemical, radiological and most importantly physical properties of the sludge. Shear behaviour is a key parameter describing the movability of legacy waste that needs to be understood in order to decommission these facilities. Several complicating factors, such as access, congested internal structure of vessels and radioactive and hazardous nature of the substances complicate sampling and prohibit the use of sophisticated and sensitive characterisation devices.

This thesis discusses the development of a novel, low cost, radiation tolerant and compact device designed for the remotely operated analysis of the shear behaviour of highly radioactive sludge *in situ* using rapid prototyping and commercial off the shelf components. Two different prototype designs have been developed, utilising different approaches to rheological assessment of rheological properties of suspensions using rotational viscometry. Radiation testing was performed on the electronic components used in these prototypes to determine their suitability for hazardous environments. Further radiation testing was performed on commercial off the shelf microcontrollers

to determine their performance during irradiation and assess their suitability for use in nuclear decommissioning environments.

The results show that the viscometer designs proposed in this thesis are suitable for further development and deployment in hazardous environments. The first design can be calibrated against any benchtop viscometer or rheometer and can provide data usable for further decision making. The second design is suitable for quality control or monitoring use in hazardous environments and has potential for use in yield stress measurements. Radiation testing has shown high resilience of commercial of the shelf potentiometers and microcontrollers. The method used to test microcontrollers has not been previously used in literature and provides a novel insight into radiation effects on the function of microcontrollers during irradiation.

Declaration

I, Tomas Fried, hereby certify that this thesis has not been previously submitted in support of an application for another degree at this or any other university. It is the result of my own work and includes nothing that is the outcome of work done in collaboration except where specifically indicated. Many of the ideas in this thesis were the product of discussion with my supervisors Dr Stephen D. Monk, Dr David Cheneler and Dr Jonathan M. Dodds.

The work described in this thesis was published and submitted for publication in these works:

- Fried, T.; Cheneler, D.; Monk, S.D.; Taylor, C.J.; Dodds, J.M. Compact Viscometer Prototype for Remote In Situ Analysis of Sludge. *Sensors* **2019**, *19*, 3299. https://doi.org/10.3390/s19153299
- (Under review) T. Fried, A. Di Buono, D. Cheneler, N. Cockbain, J. M. Dodds, P. R. Green, B. Lennox, C. J. Taylor, S. D. Monk. Radiation testing of low cost, commercial off the shelf microcontroller board. *Nuclear Engineering and Technology* (2021)
- (Pending submission) Fried, T.; Cheneler, D.; Monk, S.D.; Taylor, C.J.; Dodds, J.M. Radiation Tolerant Viscometer Design for Remote Analysis of Sludge. *Sensors.*

This work was also presented at the following events:

- Fried, T, Cheneler, D, Monk, SD, Taylor, CJ & Dodds, J 2019, 'In Situ Mechanical Analysis of Sludge in Hazardous Environments' Waste

Management Symposia 2019, Phoenix, United States, 3/03/19 - 7/03/19. (Conference poster)

- Presentations
    - NNL Decontamination and decommissioning workshop, September 2018
    - CINDe, NDA, NNL and SL waste management and decommissioning PhD event, November 2018
    - Universities' Nuclear Technology Forum (UNTF), July 2019
    - NNL decontamination science workshop, September 2019
    - CINDe, NDA, NNL and SL waste management and decommissioning PhD event, November 2019
    - TRANSEND NDA NWDRF Virtual conference, December 2020

Word count: 46613

Acknowledgements

I would like to thank my academic supervisors Dr Stephen D. Monk, Dr David Cheneler and Professor C. James Taylor for their supervision and guidance during this project. I am also grateful to my industrial supervisor Dr Jonathan M. Dodds of the National Nuclear Laboratory for his guidance and support throughout all the challenges I encountered.

I appreciate the opportunity to collaborate with Mr Antonio Di Buono, the valuable feedback from Professor Peter R. Green of the University of Manchester, and the support from the staff at the Dalton Cumbrian Facility. Furthermore, I am very happy to have been part of Centre for Innovative Nuclear Decommissioning (CINDe) and work with everyone involved in the consortium and the staff of the NNL Workington facility.

I am thankful to my parents, my sister and the rest of my family for always being here for me even when we were far apart. Last but not least, none of this work would be possible without the support of my brilliant partner Rosie, my brightest star in the darkest nights.

Table of Contents

Abstract 1

Declaration 3

Acknowledgements 5

List of Figures 10

List of Tables 18

List of Acronyms 19

1 Introduction 21

1.1 Thesis Structure 21

1.2 Introduction, Aims and Objectives 22

2 Nuclear Industry and Decommissioning 25

2.1 The Nuclear Fuel Cycle 25

2.2 Nuclear Industry in the UK 28

2.2.1 Use of Nuclear Power for Electricity Generation 28

2.2.2 Fuel Reprocessing 28

2.2.3 Nuclear Waste Types 30

2.3 Nuclear Decommissioning 31

2.3.1 Decommissioning in the UK 31

2.3.2 Decommissioning Outside of the UK 33

2.3.3 Technologies Aiding Decommissioning 35

2.4 Conclusions 40

3 Rheology of Suspensions in the Context of the Nuclear Decommissioning Industry 43

3.1 Flow Defining Parameters and Types of Flow 43

3.1.1 Defining Parameters and Newtonian Behaviour 43

3.1.2 Non-Newtonian Behaviour of Liquids and Suspensions 45

3.2 Viscoelasticity 47
3.3 Effects Caused by Particles in Suspensions 49
3.3.1 Dilute Suspensions 49
3.3.2 Suspensions Influenced by Interparticle Interactions 50
3.3.3 The Drawbacks of Theoretical Prediction of Rheology 51
3.4 Mathematical Models used to Describe Rheological Behaviour of Suspensions 52
3.5 Benchtop Instruments and Techniques for Rheology of Suspensions 55
3.5.1 Rotational and Oscillation Rheometry 55
3.5.2 Falling Ball Method 66
3.5.3 Capillary Rheometry 66
3.5.4 Quartz Crystal Microbalance 67
3.6 Yield Stress Measurements 68
3.6.1 Existence of Yield Stress 68
3.6.2 Common Yield Stress Determination Methods 69
3.7 Rheology of Suspensions in the Nuclear Industry 73
3.8 Conclusions 74
4 Shear Rate Ramp Prototype 77
4.1 Overview of the Device 77
4.1.1 Torque Measurement 78
4.1.2 Materials Used to Manufacture the Prototype 80
4.1.3 Outer Case 83
4.1.4 Measurement Geometries 84
4.1.5 Drive 86
4.1.6 Electronics of the Device 88
4.2 Calibration Procedure 92
4.2.1 Non-linearity Compensation Procedure 96

4.2.2 Onset of Secondary Effects 98
4.3 Measurement Results with Test Materials 99
4.3.1 Test Materials Used 99
4.3.2 TiO_2 Results 103
4.3.3 ZM Results 106
4.4 Conclusions 108
5 Shear Stress Ramp Prototype 111
5.1 Overview of the Device 111
5.1.1 Measurement Procedure 117
5.2 Benchtop Rheometer Modification 119
5.3 Data Collected Without a Sample and with Water 121
5.4 Simulation of the Mechanism 124
5.4.1 Simulation Overview 124
5.5 Silicone Oil Measurement and Simulation Results 129
5.5.1 1 Pa·s Calibration Oil 129
5.5.2 10 Pa·s Calibration Oil 131
5.6 TiO_2 Suspension Measurements 133
5.7 ZM Suspension Measurements 135
5.8 Conclusions 138
6 Radiation Damage to Electronics and Prototyping Materials 140
6.1 Interaction of Radiation with Matter 140
6.2 Radiation Damage to Structural Prototyping Materials 141
6.3 Radiation Damage to Conductors and Insulation 143
6.4 Radiation Damage to Passive Electronic Components 144
6.4.1 Resistors 144
6.4.2 Inductors 145
6.4.3 Capacitors 145

6.5 Radiation Damage to Semiconductors 146
6.6 Radiation Damage to Microcontrollers 149
6.7 Radiation Testing Considerations 150
6.8 Experimental Work 152
6.8.1 Continuous Turn Potentiometer of the Shear Rate Ramp Prototype ... 152
6.8.2 Continuous Potentiometer of the Shear Stress Ramp Prototype 157
6.8.3 Teensy 3.6 Microcontroller 160
6.9 Conclusions 178
7 Conclusions and Future Work Suggestions 181
7.1 Conclusions 181
7.2 Suggestions for Future Work 183
References 187
Appendices 204

List of Figures

Figure 3-1 Element of liquid deformed by shear stress caused by force F. 44

Figure 3-2 Newtonian, shear thinning and shear thickening behaviour illustrated using **a)** Shear stress curves; **b)** Viscosity curves. 46

Figure 3-3 **a)** Thixotropic behaviour in a ramp up and down test; **b)** Rheopectic behaviour in a ramp up and down test. 47

Figure 3-4 Illustration of common mathematical models describing shear behaviour of substances. 55

Figure 3-5 The most common geometries used in rotational rheometry, from left to right: parallel plates, cone and plate, concentric cylinders (or bob and cup) and vane and cup. 56

Figure 3-6 Standard cup and bob geometry, the inner cylinder is orange, outer cup is blue, sample is green and the connecting stem is red. 57

Figure 3-7 End effect correction designs in concentric cylinders, from left to right; uncorrected, air gapped design, conical end design. 60

Figure 3-8 Four bladed vane (orange) in a sample (green and purple) with an outer cup (blue) connected to the instrument with a stem (red) 61

Figure 3-9 Diagram of a modern Brookfield viscometer [86]. 66

Figure 3-10 The effect of instantaneous application and removal of stress on an elastic material (blue), viscous material (red) and viscoelastic material (purple). 70

Figure 3-11 Example curves obtained when measuring a viscoelastic substance using the creep-recovery method, where $\sigma_1 < \sigma_2 < \sigma_3 < \sigma_4$. 71

Figure 3-12 Example of stress growth data illustrating the deviation from linear response (1) and an overshoot of stress (2) before the stress starts to equalise. 72

Figure 4-1 Overview of the shear rate ramp prototype. 78
Figure 4-2 Motor placement withing the prototype. 79
Figure 4-3 Upper portion of the prototype mechanism..... 80
Figure 4-4 Top: cups printed with silver PLA, from left to right – 3, 2, 1, ISO. Bottom: geometries printed with XSTRAND^{TM} GF30-PP, from left to right – 3, 2, 1, ISO V25 Vane, ISO C25 bob. 85
Figure 4-5 Layout of the electronic components of the prototype and the associated devices. Red illustrates components exposed to harsh environment, blue is clean environment with the operator, green components are operator facing/controlled [115]. 89
Figure 4-6 The complete layout of the prototype and auxiliary devices during measurement. 92
Figure 4-7 Shear stress as a function of rotational velocity of the calibration silicone oil as measured on the commercial benchtop rheometer using a C25 standard bob and cup geometry and a V25 standard vane and cup geometry [115]. 93
Figure 4-8 Raw data obtained with the prototype when measuring the calibration silicone oil using the C25 standard bob and cup geometry [115]. 94
Figure 4-9 Raw data obtained with the prototype when measuring the calibration silicone oil using all vane and cup geometries [115]. 94
Figure 4-10 Example of final calibration curve. Vane 3 data collected and converted into shear stress including the standard deviation of five runs [115]. 96
Figure 4-11 Example of final calibration curve for Vane 3 with linear X-axis. 96
Figure 4-12 Example of compensation curve showing results for Vane 3 including fitted function parameters [115]. 97

Figure 4-13 Taylor number calculated for all measurement points acquired with the prototype using the calibration oil [115]. 98
Figure 4-14 Reynolds number calculated for all measurement points acquired with the prototype using the calibration oil [115]. 98
Figure 4-15 Shear stress as a function of shear rate of various concentrations of TiO_2 powder in de-ionised water, measured on a Bohlin CVO100 rheometer at temperatures between 21-23 °C. 100
Figure 4-16 Viscosity as a function of shear rate of various concentrations of TiO_2 powder in de-ionised water, measured on a Bohlin CVO100 rheometer at temperatures between 21-23 °C. 100
Figure 4-17 Shear curves of the TiO_2 and ZM test materials used to test the prototype with Vane 3. 101
Figure 4-18 Viscosity curves of the TiO_2 and ZM test materials used to test the prototype with Vane 3. 101
Figure 4-19 Torque required to shear a sample of zirconium molybdate suspension as a function of rotational velocity at different measurement times measured on a Lamy RM200 Plus at 20 °C. 102
Figure 4-20 PSD of the TiO_2 and ZM test materials used to test the prototype [115]. 103
Figure 4-21 Shear stress measured with the commercial benchtop rheometer compared to the results obtained using the prototype with ISO Vane, Vane 1 and Vane 2 before using the compensation procedure. 104
Figure 4-22 Shear stress measured with the commercial benchtop rheometer compared to the results obtained using the prototype with ISO Vane, Vane 1 and Vane 2 after using the compensation procedure. 104

Figure 4-23 Shear stress measured with the commercial benchtop rheometer compared to the results obtained using the prototype with Vane 3 both with and without a compensation procedure [115]. 105
Figure 4-24 Results of the calculation of potential secondary effects occurring in the test material measurements when using Vane 3 on the prototype with TiO_2 [115]... 106
Figure 4-25 Shear stress measured with the commercial benchtop rheometer compared to the results obtained using the prototype with Vanes 1, 2 and 3 before using the compensation procedure [115]. 106
Figure 4-26 Shear stress measured with the commercial benchtop rheometer compared to the results obtained using the prototype with Vanes 1, 2 and 3 after using the compensation procedure [115]. 107
Figure 4-27 Results of the calculation of potential secondary effects occurring in the test material measurements when using Vanes 1-3 on the prototype with ZM [115]. 108
Figure 5-1 The working principle of the second prototype. 112
Figure 5-2 Simplified overview of the construction of the second prototype. 112
Figure 5-3 Upper portion of the prototype. 113
Figure 5-4 Middle portion of the prototype. 115
Figure 5-5 Lower portion of the prototype. 116
Figure 5-6 Testing of the potentiometer to determine the deadzone of the measurement. 118
Figure 5-7 Example of raw data obtained with the prototype..... 119
Figure 5-8 Example of processed data after removal of deadzone and conversion to cumulative angle. 119

Figure 5-9 Custom geometry assembly made for the Lamy RM200 rheometer. Left: 3D model of the cup (red), vane (blue) and centring guard (orange). 120
Figure 5-10 Shear behaviour of water measured with the Lamy rheometer using custom geometry. 121
Figure 5-11 Output velocity as a function of measurement progress at three different input rotational velocities without a sample loaded in the prototype. 122
Figure 5-12 Output velocity as a function of measurement progress at three different input rotational velocities with water loaded as the sample..... 123
Figure 5-13 Simplified diagram of the simulation of the second prototype. 125
Figure 5-14 Average cumulative angle of the vane over five runs in 10 Pa·s calibration oil at 100 rpm input rotational velocity. Standard deviation of the data in red. 129
Figure 5-15 Output rotational velocity of the prototype at different input rotational velocities compared with the simulation results using the 1 Pa·s oil. 130
Figure 5-16 Shear behaviour of the 1 Pa·s calibration oil measured using the Lamy rheometer. 131
Figure 5-17 Output rotational velocity of the prototype at different input rotational velocities compared with the simulation results using the 10 Pa·s oil. 132
Figure 5-18 Shear behaviour of the 10 Pa·s calibration oil measured using the Lamy rheometer. 132
Figure 5-19 Torque output of the prototype with different calibration oils at different input velocities 133
Figure 5-20 Titanium dioxide suspension shear behaviour measured using the Lamy rheometer. 134
Figure 5-21 Output rotational velocity of the prototype at different input rotational velocities with a TiO_2 sample. 134

Figure 5-22 Shear rate ramp measurements performed on the Lamy rheometer with a ZM suspension. 135
Figure 5-23 Comparison of the ZM and 1 Pa·s oil data obtained with the Lamy rheometer. 136
Figure 5-24 Data obtained with the prototype using the ZM sample. 136
Figure 5-25 Comparison of the ZM and 1 Pa·s oil datasets obtained with the prototype. 137
Figure 6-1 Diagram of the testing layout for the first potentiometer 153
Figure 6-2 Example output values of rotating potentiometer sample number 1 as a function of time. 154
Figure 6-3 Data from sample 1. 155
Figure 6-4 Data from sample 5. 156
Figure 6-5 Comparison of the appearance of samples of potentiometers. From left to right: Control sample, non-irradiated; sample number 3, irradiated to 120 kGy; sample number 5, irradiated to 289 kGy. 157
Figure 6-6 Potentiometers after first irradiation with TID illustrated above each group. 158
Figure 6-7 Potentiometers after second irradiation with TID illustrated above each group. 159
Figure 6-8 Illustration of the physical layout of all the experiments performed in a top-down view. The circles marked A, B and C represent the ^{60}Co rods of the irradiator, red colour represent first, green colour second and red colour third experiment connectors and equipment. Dotted lines represent power supply wiring, dashed lines USB cable and solid lines signal wires. [162] 162

Figure 6-9 Digital test sequence as it is output by the microcontroller before irradiation. [162] 165
Figure 6-10 Reference signal used in the analog read test. [162] 167
Figure 6-11 Voltage output of the on-board voltage regulator of the microcontroller boards, supplied with 4.75 V under irradiation. [162] 168
Figure 6-12 Output voltage and current measured on the secondary board of sample C4 as a function of total dose received by the microcontroller. [162] 169
Figure 6-13 Example of the digital data output during irradiation of sample B2. [162] 170
Figure 6-14 Comparison of the digital output performance of all samples during irradiation. Red dashed line indicates 75% of the supply voltage of 3.3 V. [162] 171
Figure 6-15 Example of the analog hold data output of one of the output pins during irradiation of sample B2.[162] 172
Figure 6-16 Comparison of the analog hold output performance of all samples during irradiation. [162] 173
Figure 6-17 Example of the analog hold data output of one of the output pins during irradiation of sample B2. [162] 174
Figure 6-18 Comparison of the analog ramp output performance of all samples during irradiation. [162] 174
Figure 6-19 Example of data collected during analog read test on one of the output pins of sample C3. [162] 175
Figure 6-20 Summary of all of the analog read test data. [162] 176
Figure 6-21 Digital pin output of the sample C3 after failing to output the programmed data after a total dose of approximately 2307 Gy. [162] 177

Figure 6-22 Digital pin output of the sample C2 after failing to output the programmed data after a total dose of approximately 1421 Gy. [162] 178

List of Tables

Table 4-1 Comparison of mechanical properties of readily available 3D printing materials for prototyping [110]–[113]. 83

Table 4-2 Overview of the different geometries with the prototype. 86

Table 4-3 Overview of calibration data obtained with the prototype and commercial benchtop rheometer [115]. 95

Table 5-1 Comparison of the mean output rotational velocity of the prototype at different input velocities. 123

Table 6-1 Comparison of dose rates and total doses the samples have been exposed to 154

Table 6-2 Linear fit data for potentiometer measurements 155

Table 6-3 First irradiation experiment summary of dose rates and TIDs. 158

Table 6-4 Second irradiation experiment summary of dose rates and TIDs. 159

Table 6-5 Summary of irradiation testing results of potentiometers used in the shear stress ramp prototype. 160

List of Acronyms

ACRONYM	EXPLANATION
ABS	Acrylonitrile Butadiene Styrene
ADC	Analog to Digital Converter
AGR	Advanced Gas-cooled Reactor
ALARA	As Low As Reasonably Achievable
BAT	Best Available Techniques
BEIS	Department for Business, Energy and Industrial Strategy
BJT	Bipolar Junction Transistor
BWR	Boiling Water Reactor
COTS	Commercial Off The Shelf
DAC	Digital to Analog Converter
DAQ	Data Acquisition
DC	Direct Current
ELDRS	Enhanced Low Dose Rate Sensitivity
FDM	Fused Deposition Modeling
FGMSP	First Generation Magnox Storage Pond
GDF	Geological Disposal Facility
HAL	Highly Active Liquor
HAST	Highly Active Storage Tanks
HAZOP	Hazard and Operability
IC	Integrated Circuit
L/I/HLW	Low/Intermediate/High Level Waste
LIDAR	Light Detection and Ranging
LLWR	Low Level Waste Repository
MBU	Multiple-Bit Upset
MOSFET	Metal–Oxide–Semiconductor Field-Effect Transistor
MSSS	Magnox Swarf Storage Silos
NDA	Nuclear Decommissioning Authority

P/N/CMOS	P-type/N-type/Complementary Metal-Oxide-Semiconductor
PFSP	Pile Fuel Storage Pond
PLA	Polylactic Acid
POCO	Post Operational Clean Out
PSD	Particle Size Distribution
PTFE	Polytetrafluorethylene
PVC	Polyvinyl Chloride
PWR	Pressurised Water Reactor
QCM	Quartz Crystal Microbalance
ROV	Remotely Operated Vehicle
SEB	Single Event Burnout
SEE	Single Event Effects
SEFI	Single Event Functional Interrupt
SEGR	Single Event Gate Rupture
SEL	Single Event Latchup
SES	Single Event Snapback
SET	Single Event Transient
SEU	Single Event Upset
SIXEP	Site Ion Exchange Plant
THORP	Thermal Oxide Reprocessing Plant
TID	Total Ionising Dose
UTS	Ultimate Tensile Strength
WVP	Waste Vitrification Plant
YM	Young’s Modulus

1 Introduction

1.1 Thesis Structure

This thesis is structured in the form of seven chapters. Chapter 1 provides and introduction to the context of the work undertaken and the aims and objectives that have been identified and pursued during this project.

Chapter 2 provides an overview of the nuclear industry and decommissioning to provide the necessary background for the decisions undertaken during the course of the project.

Chapter 3 provides an overview of the field of rheology, commonly used methods and devices and the fundamental processes and science influencing the work undertaken during the project.

Chapter 4 describes the work undertaken to design, develop and test the first prototype based on a shear rate ramp measurement type and the results obtained while testing the device.

Chapter 5 describes the work undertaken to design, develop and test the second prototype based on a shear stress ramp measurement type and the results obtained while testing the device and simulating the mechanism that was developed.

Chapter 6 provides a literature review of radiation damage and testing of electronic components, work undertaken to irradiate and test the performance of components used in chapters 4 and 5 and discussion of the results obtained during the testing.

Chapter 7 provides the conclusions to the work described in this thesis and offers potential future work suggestions for both industrial and academic work.

1.2 Introduction, Aims and Objectives

In 2019 nuclear power in the UK delivered approximately 17 % of total electricity supply through 15 reactors across eight power plants [1]. All of these reactors have been in operation for over 20 years and all of them are expected to be shut down within the next 15 years. Furthermore, there are fuel reprocessing facilities such as Sellafield and research facilities that have entered decommissioning stages of their lifecycle. Nuclear decommissioning has faced challenges in lowering costs of operations. Nuclear decommissioning often entails unique challenges not often encountered in other industries to draw inspiration from. The state of the nuclear industry is discussed in more detail in the second chapter and provides further context for the industrial application of this research.

One of the key areas of nuclear decommissioning is the clean-up of legacy facilities, as seen on the Sellafield site in Cumbria. These often include hazardous environments and remote analysis is often the only approach possible to gather information. The nuclear waste in the form of suspension, or sludge, is difficult to analyse using conventional sampling methods and remotely operated, *in situ* analysis of it could reduce costs of clean-up procedures. The key scientific approach is the rheological assessment of the suspensions. Rheology is indicative not only of the physical behaviour of the suspension, providing information on how movable it is during clean-up, but also of the processes that the waste has undergone during storage. Both are key for planning and undergoing clean-up and decommissioning but also for process design in waste management, reprocessing and design of new facilities.

Rheology traditionally utilises sampling in order to analyse substances. In a nuclear decommissioning environment however, sampling may prove extremely difficult to

perform and often the costs due to risk make sampling impossible. Rheology, commonly used methods and further context are discussed in chapter 3.

The considerations outlined in this chapter and discussed in more detail in later chapters informed the aims of this research which are as follows:

- Propose an alternative approach to sampling based rheological assessment of hazardous substances in order to lower risk, costs and lead times required to develop and deploy new technologies in hazardous environments, particularly in nuclear decommissioning.
- Determine the suitability of novel rapid prototyping techniques, such as 3D printing and use of commercial off the shelf (COTS) electronics for hazardous environments and the development of novel technologies.

Based on the aims of the project the objectives of this research are as follows:

- Design and develop a measurement device capable of ascertaining rheological properties of suspensions of viscosity between 0.1 and 50 Pa·s with the following constraints:
    - Compact design capable of being able to be deployed through smaller than 75 mm diameter opening.
    - Minimal amount of electronic and other sensitive components.
    - Ability to be controlled remotely.
    - Design that enables further development for use in hazardous environments, such as *in situ* nuclear decommissioning scenarios.
- Further the development of prototypes using novel rapid prototyping techniques, such as 3D printing and commercial off the shelf electronics.

- Perform radiation testing on commercial off the shelf electronic components utilised in the prototypes and the microcontrollers used to control them and determine their resilience and potential for use in hazardous environments.

This thesis provides two novel viscometer designs specifically tailored for the needs of the nuclear decommissioning industry. They utilise minimal amount of electronic components, are extremely compact. can be operated remotely and utilise commercial off the shelf and rapidly prototype components which makes them low cost and quick to manufacture. Furthermore, testing of the electronic components showed very high resilience to gamma radiation and specifically in the case of microcontroller irradiation this thesis delivers a novel approach to testing the functionality of these components and provides a dataset that has not been found in literature so far.

2 Nuclear Industry and Decommissioning

This chapter aims to provide the necessary context for the work described by this thesis by discussing the nuclear industry and the role of nuclear decommissioning in the nuclear fuel cycle.

2.1 The Nuclear Fuel Cycle

The most commonly used fuel in nuclear power plants is uranium. The fuel cycle starts with mining and milling ore that commonly contains uranium in relatively low quantities – low-grade ore contains 0.1 % uranium and high grade ore contains 2 % uranium. Some ore contains exceptionally high quantities (predominantly in Canadian deposits) and poses more challenges for maintaining safety for operators during mining. Standard grade ore however does not require any special precautions compared to mining other types of ore [2].

Uranium can be found naturally occurring in three isotopes – ^{238}U, ^{235}U and ^{234}U. The first isotope is the most common and accounts for more than 99 % of natural supply of uranium. While some reactor types can use natural uranium as fuel (such as Magnox or Pressurised Heavy Water Reactors (predominantly found as CANDU type reactors)) the majority of currently used reactors uses low enriched uranium. Low enriched uranium consists of a higher-than-natural proportion of the fissile isotope of uranium – ^{235}U. The uranium oxide is leached after being crushed and ground and a solution is used to separate the uranium from the rest of the ore. The finished uranium oxide is only mildly radioactive and is often referred to as “yellowcake”. The fuel is then purified and converted into uranium hexafluoride in order to be enriched. Enrichment is a process that increases the amount of ^{235}U in the fuel to 3-5 % which

enables its use in other types of reactors, such as Pressurised Water Reactors (PWR), Advanced Gas-cooled Reactors (AGR) or Boiling Water Reactors (BWR) [2].

There is a wide variety of reactor types used around the world, however they all use principally identical components. All reactors use steam to drive a turbine that in turn drives an electric generator. There are several criteria that help differentiate between reactor types. The first has already been mentioned – the fuel. Some reactors can use non-enriched uranium (for example in the form of natural uranium metal) while others require enriched uranium. The differences go further, some require only uranium in the form of an enriched oxide (UO_2), some use mixed oxide (MOX), that combines uranium and plutonium oxides.

The second differentiating factor is coolant type and condition. Reactor cores are predominantly cooled by water or gas. In BWRs the water cooling the reactor core also drives the turbine to generate electricity, before being condensed using a secondary circuit and redirected back to the core for cooling. In PWRs the water cooling the reactor core does not boil – instead it is pressurised so it reaches higher temperatures and heats up water in the secondary circuit that is then evaporated and the steam drives the turbine before being released into the environment. Similarly to the PWR design, CANDU reactors and AGRs use a secondary circuit of water to drive a turbine with steam, with the main difference between them being the coolant. AGRs use gas coolant in the reactor core, namely CO_2 and CANDU reactors use heavy water. The higher temperature the coolant can reach compared to water-cooled reactors means AGRs are thermodynamically more efficient than water-cooled reactors [2].

The third differentiating factor is the type of moderator the reactors use. Moderators reduce the neutron speed, making the neutrons more likely to enable nuclear fission. In PWR and BWR designs the cooling water is the moderator, CANDU reactors use the cooling heavy water as moderator and AGRs use graphite rods as moderators [2].

There are of course more nuanced differences in different reactors of the same type. Furthermore, novel types of reactors are discussed as part of the Generation IV reactor debate. Several different designs, such as Molten Salt Reactors or Very High-Temperature Reactors have been proposed as part of this discussion and show promising results for the future of the nuclear industry. Increasingly, the focus has also shifted towards the potential of using small modular reactors. All of these developments are made to increase the safety and efficiency of the reactors while decreasing the costs of new builds [2], [3].

The last part of the nuclear fuel cycle is reprocessing, recycling and disposal. The main goal of reprocessing is separating waste products from the used fuel and retaining the reusable substances still present in the fuel, such as uranium and plutonium. Recycling is focused on the reuse of spent fuel to create new fuel. Finally, disposal is the permanent storage of nuclear waste with no intention of retrieval. All of these steps present their own challenges. While it is not directly part of the nuclear fuel cycle, the decommissioning of nuclear facilities after the operations cease is closely linked to the nuclear fuel cycle. As such, they will be further described in the following chapters.

2.2 Nuclear Industry in the UK

2.2.1 Use of Nuclear Power for Electricity Generation

The use of nuclear power for the purpose of generating electricity in the UK began in 1956 when the first reactor in Calder Hall was connected to the grid. The power station at Calder Hall consisted of four Magnox type reactors serving a dual purpose of electricity generation and producing plutonium for nuclear weapons. The reactors have been fully defueled in 2019 [4]. The nuclear reactors built until 1965 have all been made as Magnox type reactors. None of these stations generate electricity anymore and they are in various stages of defueling and decommissioning.

The current fleet of operating civil nuclear power plants in the UK consists of 14 AGRs across seven sites and one PWR. Two more PWRs at one site are under construction and several more reactors of various designs are planned to be constructed. Nuclear power accounted for approximately 21% of electricity production capacity in 2015 and was planned to increase to 33% by 2030 [5].

2.2.2 Fuel Reprocessing

There are two main workstreams of nuclear waste reprocessing in the UK, both based at the Sellafield site. The first is Magnox reprocessing, which started operations in 1964. The site reprocesses fuel from Magnox type reactors. The fuel is first stored for 180 days in a pool to cool down while short lived fission products decay before the cladding is removed from the fuel itself in the Fuel Handling Plant. The pool water and sludges are processed by the Site Ion Exchange Plant (SIXEP) and the swarf from the Fuel Handling Plant is encapsulated in the Magnox Encapsulation Plant. The decanned fuel is dissolved in nitric acid and the fission products, uranium and plutonium are separated. The intermediate level waste (ILW) is processed by the Enhanced Actinide Removal Plant (EARP), the Highly Active Liquor (HAL) is

processed in Highly Active Evaporators and the Low Active Effluent is sent to the Segregated Effluent Treatment Plant. Plutonium and Uranium go through finishing and are made into their oxide products in the form of cans and drums. With the end of use of Magnox reactors the reprocessing was scheduled to cease reprocessing in 2020 and begin transition into preparation work for decommissioning, however due to the COVID-19 pandemic this was postponed until 2021 [6], [7].

Fuel from AGR is processed in the Thermal Oxide Reprocessing Plant (Thorp). Unlike Magnox fuel, AGR fuel is used around the world and therefore Thorp reprocessed fuel from both UK and overseas sources. The plant began processing fuel in 1994 and ceased operation in 2018 [8]. Similarly to Magnox, the received fuel is temporarily stored in ponds to allow it to cool further before processing. It is then sheared into smaller sections and the fuel is dissolved in nitric acid. In reprocessing the waste is separated from the uranium and plutonium, both of which can be reused to make new fuel. The high level waste is processed in the same HAL workstream as Magnox high level waste and the ILW is processed by the Waste Encapsulation Plant. Since 2018 no shearing of new spent fuel has been taking place, Thorp entered Post Operational Clean Out (POCO) state and stores spent fuel in the ponds. It is expected to receive spent fuel until 2034, pending the disposal of it in a Geological Disposal Facility (GDF) [6], [9].

Because of the end of all reprocessing operations, the nature of work performed on the Sellafield site is changing. One of the steps after end of operations and before decommissioning is POCO. Several sites on Sellafield are currently undergoing POCO, some are currently being decommissioned and some have been or are in the process of being demolished. The decommissioning works on Sellafield will be further described in chapter 2.3.1.

2.2.3 Nuclear Waste Types

Nuclear waste arising from reprocessing, decommissioning but also other industries such as medical applications is classed as low, intermediate or high level waste (L/I/HLW). A sub-category of LLW called very low level waste is sometimes discussed too – this is waste that can be disposed of along with for example municipal waste where permitted. More than 90% of volume of waste worldwide and in the UK is classed as LLW. While accounting for a very small fraction of the total volume of waste (less than 0.1 %), HLW still accounts for the majority of radioactivity associated with nuclear waste (over 75 %) [10]–[12].

Short term storage of spent nuclear fuel is predominantly done by depositing it into pools. Storage in this context means temporary placement of fuel before final disposal, after which no intention of retrieval is expected. During short term storage, ILW and HLW are cooled in pools that also serve as shielding during storage.

LLW is currently available to be disposed of at the Low Level Waste Repository (LLWR) in the UK. Furthermore, ILW is often immobilised to reduce the amount of radioactive waste within a waste package and the immobilising material further serves as shielding from the encapsulated nuclear waste [13]. Final disposal of waste is planned to happen using a GDF.

HLW predominantly exists in the form of a suspension. This is often referred to as liquor, specifically HAL in the UK reprocessing plants. In the UK, this liquor is temporarily stored and cooled down in Highly Active Storage Tanks (HAST) – large vessels with complex internal cooling systems designed to extract the heat of radioactive decay of the liquor. The liquor is then processed in the Waste Vitrification Plant (WVP), where the liquor volume is significantly reduced, forms a vitrified

product and encapsulated in stainless steel containers. These containers are either sent back to the overseas customers or temporarily stored at the Vitrified Product Store awaiting disposal in a GDF [6], [13].

2.3 Nuclear Decommissioning

2.3.1 Decommissioning in the UK

Decommissioning in the UK is overseen by the Nuclear Decommissioning Authority (NDA). It is a public body reporting to the Department for Business, Energy and Industrial Strategy (BEIS). The NDA does not decommission directly, but rather through its subsidiaries, such as Sellafield Ltd or other companies [14].

The NDA owns 17 nuclear sites and its subsidiaries often work as the site licence companies responsible for the sites. 11 of the sites are Magnox power generating sites placed across the UK[1] and managed by Magnox Ltd – a subsidiary of NDA as of 2019. These sites go through five phases in their lifecycle before they undergo decommissioning. Two sites are currently undergoing defueling and the rest is in "Care and maintenance preparations" phase. It should be noted that the final phase completion is currently conditional on the existence of a GDF.

The Dounreay site in Scotland is currently undergoing decommissioning operations and is the facility expected to finish decommissioning works first. LLWR located in Cumbria is still functioning as repository of LLW from various sources around the UK [14].

The Springfields facility is the UK's primary nuclear fuel manufacturer. It still manufactures fuel for both AGR and PWR facilities, but it is also a decommissioning

[1] England: Berkeley, Bradwell, Calder Hall, Dungeness A, Hinkley Point A, Oldbury, Sizewell A; Scotland: Chapelcross, Hunterston A; Wales: Trawsfynydd, Wylfa.

site. Some of the older parts of site are undergoing POCO and clean-up and decommissioning started in 1990 [15].

The Capenhurst facility stores most of the UK's depleted uranium and is currently owned and operated by Urenco Nuclear Stewardship Ltd [14]. It serves as an enrichment facility and deconversion facility for uranium hexafluoride.

The Sellafield site is the most significant decommissioning facility in the UK and it also contains the Calder Hall Magnox facility in its premises. It is not exclusively a decommissioning site as work undertaken there is classified into four distinct categories:

- Decommissioning
- Spent fuel reprocessing
- Waste treatment and packaging
- Storage of radioactive waste

The site is scheduled to be fully decommissioned, demolished and the land remediated over the next 100 years at a total cost exceeding £100 bn [16]. This budget is divided into four value streams – waste retrievals, remediation, spent fuel management and special nuclear material management [17].

There are four legacy ponds and silos on the Sellafield site which present some of the biggest challenges for retrievals and decommissioning [6], [9], [17]:

- First Generation Magnox Storage Pond (FGMSP) – although final fuel has been received in 1992 it still contains waste materials fuel fragments and corrosion products from the fuel cladding. Bulk fuel is expected to be retrieved by 2031.

- Pile Fuel Storage Pond (PFSP) – similarly to FGMSP the pond has been used to store Magnox fuel, later it has been used to store contaminated items and also operational waste. Currently it contains used nuclear fuel, sludge, ILW and the water itself. The pond is expected to be emptied by 2029.
- Magnox Swarf Storage Silos (MSSS) – initially serving as underwater storage facility for the swarf waste created by de-cladding Magnox fuel prior to processing, the silo has been extended several times and contains a variety of waste types, mostly ILW in dry form.
- Pile Fuel Cladding Silo – the silo consists of six compartments holding ILW. The waste is predominantly de-canning waste from processing Magnox waste. It is situated in a highly congested area on the site, complicating access and retrieval operations. Bulk retrievals are expected to be finished by 2030.

Another important section of the site that will have to undergo decommissioning and presents a large challenge is the HAL workstream. Vitrification was expected to stop in 2022 and after that retrievals and POCO of HASTs and the vitrification plant are expected to finish by 2034, enabling the decommissioning of this part of the Sellafield site. Although most plans are focused on reducing the amount of structures, interim plans often include construction of new facilities to aid and enable decommissioning. An example of this is the construction of a new evaporator unit for the HAL workstream – Evaporator D – which has been finished in 2017.

2.3.2 Decommissioning Outside of the UK

There are many examples of nuclear decommissioning around the world. Most of them are end-of-life, planned works on nuclear power plants and other facilities. The most challenging work is dealing with legacy sites that have not been designed with

decommissioning in mind or have operated beyond their planned lifetime. Two important overseas examples are the Hanford and Savannah River sites in the USA.

The Hanford site was established in 1943 to produce material for nuclear weapons. The site has produced plutonium and electricity until 1987 when the operations ceased and the site transitioned into the decommissioning phase. There are 177 tanks that contain HLW created during the operation of the site. Material is being transferred from the single-shell tanks into the double-shell tanks and the waste is pending vitrification in the Waste Treatment and Immobilization Plant that is currently being constructed. However, settled material remains in the single shelled tanks that will require retrieval operations before decommissioning [18].

The Savannah River Site has been producing materials for nuclear weapons for over 60 years now and still continues to do so. It also stores spent nuclear fuel and just like the Hanford site it houses large amounts of HLW in underground storage. It also contains a functioning vitrification plant processing the HLW into glass waste packages [19]. The main difference between the Sellafield site and the US sites is their size – Sellafield site covers 6 km^2 whereas Savannah River Site covers over 802 km^2 and Hanford even a larger area of over 1517 km^2.

The second kind of decommissioning is unplanned work – most commonly in response to incidents. The two most prominent cases are the Chernobyl site and the Fukushima Daiichi decommissioning efforts. In 1986 during a safety test, the fourth reactor of the Chernobyl nuclear power plant exploded. In 2011 due to an earthquake and the consequent tsunami three reactor cores have been damaged at the Fukushima Daiichi nuclear power plant. Immediately after both incidents significant efforts have

been focused on emergency response, characterisation, decontamination and decommissioning at both sites.

Each of these sites requires different decommissioning approaches and different technologies to aid that work. The Chernobyl site served as the first point of real-world deployment for robotic platforms in nuclear environments. While this led to a great deal of failures it provided valuable feedback for the development of these technologies. There is some crossover between these facilities and even the Sellafield facility – for example underwater Remotely Operated Vehicles (ROV) have been developed for deployment on the Sellafield site but have found use on the Fukushiima site as well. Identical aerial ROVs can be used for several different purposes without modifications to the platform itself or the sensor bundle – the same radiation detection system can be used to monitor waste disposal sites, track released contamination or decontamination efforts and find contamination remotely [20], [21]. The following section summarises the technologies used across nuclear decommissioning sites.

2.3.3 Technologies Aiding Decommissioning

Clean-up and decommissioning activities are much easier on sites that have been designed to be decommissioned and are undergoing planned work. As witnessed on legacy sites and dealing with the aftermath of accidents however, that is not always the case. In such cases, decommissioning presents unique challenges not encountered in other industries, which promotes the design and use of novel technologies. While there are more types, two dominant categories of important decommissioning technologies can be created: characterisation and decontamination techniques. An auxiliary branch enabling both of these is the deployment technologies.

2.3.3.1 Deployment

Some decommissioning facilities are very difficult to access and will often limit access to remote devices only in order to minimise risk. For that reason a wide variety of robotic platforms have been developed across the world to tackle these issues. These can be classed into three distinct categories – underwater, land based and aerial robotic platforms. Furthermore, they commonly serve two main functions – exploratory, where they aim to enter and analyse unknown or poorly defined areas, and monitoring, where they provide a continuous stream of data to maintain appropriate working conditions.

Underwater devices have been developed and used for deployment in ponds, tanks and other filled vessels. A good example is the AVEXIS robot – a device for *in situ* exploration and characterisation of environment underwater. It was designed using rapid prototyping techniques and carries a camera and a scintillator to characterise the contents of ponds, for example on the Sellafield site [22], [23]. This category could also include devices used on the surface of ponds, for example to help inspect and decontaminate the walls of ponds on the Sellafield site [24]. The devices are often tethered to ensure recovery in case of failure and ensure data transmission.

Land based devices have been tasked with entering hazardous environments and carrying a variety of sensors and imaging systems. Some are designed to enter through compact openings like pipes [25], others are designed as heavy-duty carriers of sensor bundles [26]. There are more specialised robots too, such as wall-climbing or pipe-crawler platforms [27], [28]. The robots are not limited to exploration, automated monitoring of contamination is also appealing to many facilities and has lead to the development of compact wheeled robots to perform this task [29].

Aerial robots, often referred to as drones, have gained a lot of popularity not only in the professional applications but for recreational use too. That has significantly lowered the prices of commercial off the shelf (COTS) drone systems and allowed for more research to be performed with them. Most research is focused on using the drones to carry sensor bundles, but some work is aimed at enhancing their control and localisation for other tasks such as surface analysis and decontamination [30].

Usage of rapid prototyping and COTS components has become an observable trend in developing these platforms. Several of the examples listed above use 3D printing for crucial components and COTS electronics to run them. This approach significantly reduces prototyping costs and manufacturing times and several designs have proven to be capable of handling nuclear environments.

2.3.3.2 Characterisation

Radiation detectors are probably the most common sensor type used on deployment platforms discussed above. They serve two different purposes – they ascertain the risk associated with the environment and help decide further strategies based on the activity levels or they provide a more complex analysis of the radiation providing information about the materials present. Some designs combine an optical imaging dataset with a Compton camera dataset to provide a more complex picture of the radiation sources and their location [31], other systems will provide a simpler radiation dose measurement in a more compact package that can be deployed more easily [32].

As witnessed in [25], imaging technologies have evolved beyond using cameras to visualise remote areas. Light Detection and Ranging (LiDAR) is a method of scanning environments using a combination of lasers and detectors and provides a robust

overview the environment it is scanning. Unlike conventional cameras, the 3D image generated using the LiDAR can be used to validate the environment against records and allows for a more robust approach in planning decommissioning. It should not be seen as a replacement for a visual inspection using conventional cameras, rather an addition. It also offers a lot of potential for remote operation of instruments, using Virtual or Augmented Reality approaches, which are increasingly more appealing to the nuclear industry [33].

In situ characterisation tools have been developed for a range of properties and applications across the nuclear industry. Acoustic backscatter systems can be used to monitor suspension concentration and settling conditions [34]. Radiation detectors have been used to not only determine the activity levels inside storage tanks, but also to infer the position and depth of sludge within them based on the data [35]. Laser-induced breakdown spectroscopy is a relatively novel method capable detection of materials but also their concentration [36]. [37] suggests that optical fibres can be used to measure several properties, such as temperature, strain, radiation dose and hydrogen detection at nuclear facilities. Quartz crystal microbalance has been proposed as a method to measure physical properties of suspensions such as nuclear slurries [38].

Despite a varied range of techniques used in nuclear decommissioning i*n situ* analysis of mechanical properties of sludge is not reported on in literature. This is due to the extremely complex nature of deployment and data acquisition but also potentially due to data not being publicly available. The most closely related report on an instrument to analyse mechanical properties of sludge *in situ* is [39], where the authors propose a prototype device based on a handheld vane borer Geonor H60 connected to an electric motor. The publication does not describe deployment results.

2.3.3.3 Decontamination

Decontamination of surfaces is an important part of POCO and decommissioning. An appropriate decontamination technique can vastly lower the amount of waste during decommissioning operations, as only the removed contaminated surface becomes the hazardous waste. There is a vast variety of surface types that require decontamination, from the internal surfaces of pipes to the surfaces of vessels and even buildings. Choosing an appropriate decontamination technique is an incredibly challenging task that depends on the properties of the surface, but also environmental conditions, ease of access and other factors [40].

Fundamentally, there are three types of decontamination approaches that are currently used. Chemical decontamination uses chemical reagents to extract the contamination. While it is often designed in order not to damage the material itself often some damage to the surface of the decontaminated material occurs. It can be an obvious choice for some systems – for example pipelines that are already designed to allow flow of materials and have pumps and systems to provide the flow of reagents. The main disadvantage is the need to recycle the reagents, otherwise the amount of secondary waste can render the method inefficient [40], [41].

Electrochemical decontamination is in principle a subset of chemical decontamination. It uses reagents and electrical current to remove layers from the surface of materials. It is a very efficient method allowing decontamination of whole components. The main drawbacks are the necessity for the decontaminated material to be conductive and the practical limitations of having to immerse the component in a reagent bath. The most common applications for this method are smaller steel components such as valves. Furthermore, the necessity to handle the components may prove to be impossible due to risk mitigation [40], [42].

Lastly, mechanical decontamination is the simplest method as it is the process of physically removing the contaminated layers of material while preserving the non-contaminated bulk of the component. This includes a wide variety of methods, from simple cleaning procedures to more complex methods using abrasive materials and extraction mechanisms to contain waste. Laser ablation is one of the most novel methods that could be classed as a subset of mechanical decontamination. This is a very promising method that can be adjusted to be used with almost any material but requires a lot of work to select appropriate working conditions. Mechanical decontamination methods are not suitable for complex surfaces, making them most appealing for structural materials and large surface areas [40], [43].

2.4 Conclusions

Nuclear decommissioning efforts come at a high price mainly due to the unprecedented challenges they often present. In the case of accidents the importance of quick reaction while not compromising safety is the main source of high costs. In the case of decommissioning legacy sites the challenge is mostly due to the fact that the sites have not been built to be decommissioned and there are few historical decommissioning efforts to use as references. The age of some sites presents further challenges, such as imperfect inventory records and aging infrastructure. At the same time, the nuclear industry is under pressure to reduce costs of all operations – the Nuclear Sector Deal published by the UK government sets out the goal of reducing the cost of new builds by 30% and the cost of decommissioning by 20% by 2030 [3].

There is a wide range of deployment platforms available for all types of applications. Robotic devices capable of going through small openings like pipes, aerial ROVs and ground robots capable of traversing almost any type of obstacle are present in literature. Floating and underwater robots have also been developed and successfully

deployed at several decommissioning sites. The sensors and mechanisms they carry however are more limited in the literature in comparison.

Radiation detection and analysis is well established. Various devices providing complex visualisation of radiation activity distribution or very compact scintillators have been developed and presented. Visualisation techniques including modern methods such as LiDAR have also been developed and their capability demonstrated. Other properties can be investigated such as temperature or strain using optical fibres. Mechanical analysis of sludge however is very limited. Most techniques will use different kinds of measurements to infer the composition and behaviour of suspensions in vessels, such as acoustic backscatter and radiation activity [44].

The biggest contributor to cost is risk. Risk is often mitigated by using remote operations where possible, including *in situ* characterisation to gain a more complex picture of the situation. Nuclear industry in England has many processes in place to ensure a safe and responsible development and deployment of new technologies. Best Available Techniques (BAT) guidance provided in [45] helps illustrate some of this approach in nuclear decommissioning and waste management. One of the aims of the guidance is to ensure that the exposure to public is As Low As Reasonably Achievable (ALARA). This approach is used to ensure compliance with legislations such as the Energy Act 2010, the Environmental Permitting Regulations 2010 and the Radioactive Substances Act 1993 through evidence based development and implementation of processes, methods and facilities. BAT studies often include, or are included in Hazard and Operability (HAZOP) studies that are used to identify risks to personnel and equipment that could prevent operation of processes and facilities.

The use of this complex and rigorous approach to new technology explains a relative lack of COTS and rapid prototyping tools in the nuclear industry. However, it also presents the case for one use designs using COTS platforms. This approach can reduce costs directly – due to the decreased cost of components and indirectly as the manufacturing times necessary to make prototypes are lower. Rapid prototyping techniques are also a relatively new but promising tool to use when developing technologies for nuclear decommissioning. In-house manufacturing significantly decreases the cost of prototyping and novel 3D printing materials are increasingly more resilient, even to very harsh environments. It also enables the use of sacrificial designs – platforms designed to maintain their performance for a single use before being decontaminated, decommissioned and disposed of. As their cost can be orders of magnitude lower than using conventional methods this can be of great use for some applications.

3 Rheology of Suspensions in the Context of the Nuclear Decommissioning Industry

The field of rheology, named by Eugene Bingham [46], focuses on studying the flow and deformation of materials. As such, it can be considered a subset of mechanics, dealing with both fluids and solids. Rheology is most often discussed in the context of describing and analysing the behaviour of substances with complex microstructure, such as polymers and suspensions, as they often exhibit complex behaviour.

The aim of this work is to determine whether the most commonly used techniques can be adjusted for use *in situ* and produce usable results when compared with the commonly used benchtop instruments. In this chapter, an overview of what rheology is and how it describes suspensions will be provided, followed by commonly used rheometry methods in order to provide the necessary context for the development of viscometer prototypes.

3.1 Flow Defining Parameters and Types of Flow

3.1.1 Defining Parameters and Newtonian Behaviour

In order to describe the consequences of forces being applied to induce flow one has to define several parameters. The first two definitions describe the difference between solid and liquid behaviour when subjected to forces. In solids, the following equation is referred to as Hooke's law:

$$\sigma = G\gamma \tag{3.1-1}$$

where σ is normal stress applied to the material (reported in Pa), G is the elastic modulus (Pa) and γ is strain (dimensionless, as it is relative deformation). The analogue equation for liquids, referred to as Newton's law of viscosity is:

$$\tau = \eta\dot{\gamma} \tag{3.1-2}$$

Where τ is the shear stress in the material (Pa), η is the viscosity of the liquid (Pa·s) and $\dot{\gamma}$ is the change of strain per unit of time referred to as shear rate (reported in s^{-1}). The simplest example of shear in liquids is illustrated in Figure 3-1 - in this example the material is sheared only in one direction by force *F*.

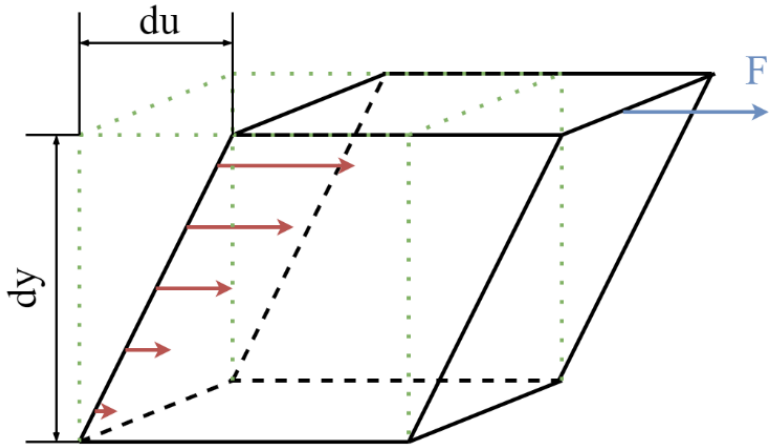

Figure 3-1 Element of liquid deformed by shear stress caused by force F.

In this case, shear rate can be calculated as the velocity gradient in the liquid:

$$\dot{\gamma} = \frac{du}{dy} \tag{3.1-3}$$

Hooke's law describes the deformation of an ideally elastic solid and can only be applied for small strains. The material recovers from the elastic strain after the force applied to it is stopped and returns to its initial state. Newton's law of viscosity establishes what is known as Newtonian liquids, where the shear stress is linearly proportional to the shear rate applied to the liquid, in other words, the viscosity of the material remains constant irrespective of the shear rate applied [47].

This linear, or Newtonian response to shear rate applies in some liquids and perfectly Newtonian flow behaviour is only a theoretical model, just like perfectly elastic solid behaviour. Solids dispersed in liquids, or suspensions, rarely exhibit Newtonian

behaviour and some of the deviations from linear response they exhibit will be described in section 3.1.2.

3.1.2 Non-Newtonian Behaviour of Liquids and Suspensions

In shear thinning materials the viscosity of the material decreases as the shear rate applied to it increases. These materials are also referred to as pseudoplastic and different mechanisms have been described as the cause of this behaviour. In suspensions, breakdown of particulate clusters is one of the mechanisms discussed when observing shear thinning behaviour [48]. Further research suggests that layering and alignment of the particles is also one of the mechanisms causing shear thinning [49], [50].

In shear thickening materials the viscosity of the material increases as the shear rate applied to it increases. These materials are also referred to as dilatant. The literature suggests that the mechanisms attributed to this behaviour are the formation of hydroclusters [51] or other forms of aggregation of particles into clusters as a consequence of the flow induced in the system, for example due to enhanced magnetic interactions [52]. It is also very common for materials to exhibit shear thickening behaviour after exhibiting shear thinning behaviour - in the context of a shear rate ramp the layers causing shear thinning start breaking up as the shear rate keeps increasing, causing the viscosity to rise [53].

Shear thinning and thickening are only dependent on shear rate, not time. The effects of the history of the material being sheared are described by different terms. Thixotropic behaviour describes materials that exhibit lowering viscosity as they are being sheared with a constant shear rate. This has further implications on rheological

measurements. First, any shear thinning behaviour observed when performing experiments could actually be thixotropic effects observed.

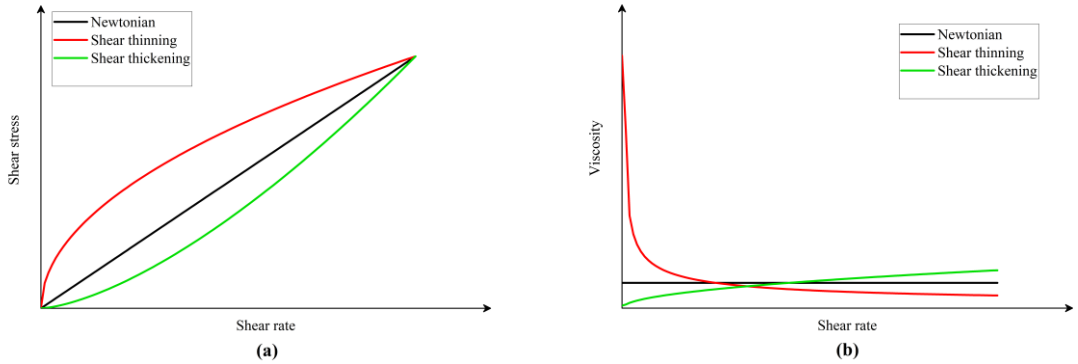

Figure 3-2 Newtonian, shear thinning and shear thickening behaviour illustrated using **a)** Shear stress curves; **b)** Viscosity curves.

It is obvious there is certain overlap between the two effects and that can complicate interpretation of the measurement results. Second, this implies that the history of the material, not only due to previous measurements but also due to sampling, transport and storage can have observable impact on the measurement results [48].

A material that exhibits an increase in viscosity as it is being sheared with a constant shear rate is described as rheopectic, or anti-thixotropic. This behaviour has been observed with coal-water dispersions for example [54]. Literature suggests that at certain shear rates, the collisions promoted by the shear cause aggregation of particles which consequently increases the viscosity of the material. When the shearing is stopped, these aggregates are broken down by random Brownian motion in the suspension [48].

Thixotropic and rheopectic behaviour can be observed in shear rate ramp tests that include a ramp up as well as a ramp down or a constant shear rate test. Under constant shear rate tests, the behaviour will be observable as gradually decreasing or increasing shear stress. In ramp tests, this behaviour causes a hysteresis loop in the measurement data, as shown in Figure 3-3.

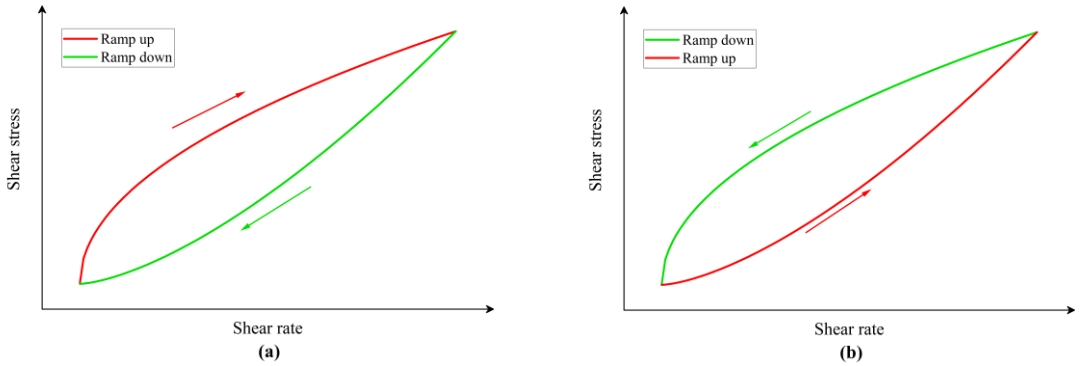

Figure 3-3 **a)** Thixotropic behaviour in a ramp up and down test; **b)** Rheopectic behaviour in a ramp up and down test.

It is apparent that these kinds of behaviours increase the complexity of interpretation of the obtained results. The main issue these effects present is the importance of how the sample has been treated before measurement. Making a representative measurement of complex materials *ex situ* is complicated by all the forces a sample is subjected to before being analysed. Even *in situ* measurements must be made carefully as not to change the properties of the sample by deployment.

3.2 Viscoelasticity

Viscoelastic materials exhibit both solid and liquid-like behaviour, in that they exhibit both elastic properties like a solid would and viscous properties like a liquid would. The main consequence is that these materials can recover from shear. From a practical perspective, this behaviour influences yield stress measurements the most and will be further elaborated on in chapter 3.6..

Viscoelastic behaviour is mostly observed in solids, polymers (including their liquid state) and in some suspensions. In the context of suspensions, viscoelastic behaviour is mostly discussed when using oscillatory techniques for rheological measurements. The effects of viscoelasticity is often considered to be lower in suspensions than in polymeric liquids [53].

Aside from yield stress measurements, most literature deals with viscoelasticity in the context of polymer rheology. Under small deformations, the behaviour of these substances can be described with linear viscoelasticity. The most important models describing their behaviour are the Maxwell model (a spring and a dashpot connected in series) and the Kelvin model (a spring and a dashpot connected in parallel). The models are the founding blocks of other, more complex models more accurately describing viscoelastic substances at low deformations [55].

Non-linear viscoelasticity is a much more complex subject dealing with substances undergoing large deformations. Two main models describing the behaviour of materials under these conditions are the differential and integral viscoelastic models [55].

Furthermore, two dimensionless numbers are often used when dealing with viscoelastic substances. The Deborah number was proposed by Marcus Reiner and it describes the effect of time on the deformation of materials, or their fluidity in other words [55]:

$$De = \frac{\lambda}{T} \tag{3.2-1}$$

where λ is the relaxation time of the material (s), a characteristic of the substance and T is the characteristic time of the process of deformation (s), sometimes referred to as time of observation. A material with a Deborah number equal to zero can be considered a fluid and a material with a Deborah number equal to ∞ can be considered a solid [55].

The second dimensionless number used in the context of viscoelasticity is the Weissenberg number, describing the deformation of the material:

$$We = \lambda\dot{\gamma} \tag{3.2-2}$$

Using both Deborah and Weissenberg numbers helps ascertain what type of flow and behaviour one can expect in a system. The scope of viscoelasticity, especially non-linear viscoelasticity is significantly broader than described here, but is not commonly discussed in the context of suspensions in the nuclear industry beyond yield stress measurements.

3.3 Effects Caused by Particles in Suspensions

3.3.1 Dilute Suspensions

The foundation of suspension rheology lies with Einstein's work on what he refers to as "internal friction" in very dilute suspensions containing hard spheres. This work makes many assumptions about the investigated material, for example, it assumes a Newtonian liquid suspending rigid, spherical particles that are always spaced far apart enough to prevent the influence of one particle on any other. In his paper [56] and a later correction [57], Einstein proposes that the viscosity of a suspension can be calculated as:

$$\eta = \eta_s(1 + \frac{5}{2}\phi) \tag{3.3-1}$$

where η_s is the viscosity of the suspending medium (Pa·s) and ϕ is the volume fraction of the particles (dimensionless). It is apparent that in this model the suspension is still Newtonian even after the addition of the particles and the particle size does not affect the viscosity. Other authors further elaborated on this work, trying to quantify under which conditions particle migration becomes observable in Couette and Poiseuille flows [58]. Further work has been performed analysing the effect of non-spherical particles and challenges other assumptions in Einstein's model to further develop it. It is however rare to deal with very dilute suspensions exhibiting Newtonian behaviour,

even in the nuclear industry. In more concentrated suspensions, interactions between particles become more prominent.

3.3.2 Suspensions Influenced by Interparticle Interactions

Once the volume fraction reaches a point where interparticle interactions have observable influence on the viscosity of the liquid, Einstein's model is not applicable. Several interaction forces can exist in suspensions and depending on the concentration and composition of the suspension they have varying levels of influence on the viscosity.

3.3.2.1 Brownian Motion

In the simplest expansion of Einstein's model of hard spheres, the only interaction between particles exists in the form of Brownian motion. In this case, the particles only interact in the moment they come into contact. Batchelor proposed, that the contribution of Brownian interactions can be quantified to expand Einstein's model as [59]:

$$\eta = \eta_s(1 + \frac{5}{2}\phi + 6.2\phi^2) \tag{3.3-2}$$

This model maintains a number of Einstein's assumptions and its applicability is still limited. Some of these assumptions have been challenged, such as the effect of non-spherical shaped particles or the use of non-Newtonian fluids.

3.3.2.2 Colloidal Suspensions

In real materials, Brownian motion is not the only interparticle interaction. Generally, these can be classified as repulsive or attraction forces. In colloidal suspensions, the influence of repulsive forces outweighs that of attraction forces which makes the

suspension stable - or in other words, maintains the spacing between particles. This stability can usually be electrostatic or polymeric [46].

As this thesis does not deal with polymers, focus will be given to electrostatic stability. In these suspensions, dispersion forces are balanced by electrostatic repulsive forces. These are influenced by the particle size distribution and shape as well, bringing more complexity in the ability to predict the viscosity of material based on the composition. Most crucially, electrostatic forces in the context of nuclear suspensions are discussed as they describe the aggregation of suspensions. Aggregation further complicates assessment of samples, especially after their removal from source and thus disrupting their aggregation.

Krieger and Dougherty introduced an equation valid for suspensions of hard spheres allowing one to calculate viscosity as a function of volume fraction [60]. It has since been adjusted and used for particles of various shapes, for example by [53] as:

$$\eta = \eta_s \left(1 - \frac{\phi}{\phi_m}\right)^{-[\eta]\phi_m} \tag{3.3-3}$$

where ϕ_m is the maximum packing fraction of the suspension (dimensionless) and $[\eta]$ is intrinsic viscosity (Pa·s). The intrinsic viscosity varies with the shape of the particle and has been tabulated for use with some suspensions.

3.3.3 The Drawbacks of Theoretical Prediction of Rheology

As seen in the previous section, all of these models rely heavily on assumptions. Various studies and modern models help incorporate more factors into the calculations, however, the main issue in the context of the nuclear decommissioning lies within obtaining data for the mathematical models. Sampling opportunities are extremely limited and handling active samples makes sampling procedures expensive.

Wide range of properties that impact rheological behaviour further complicates modeling rheological properties of nuclear sludges.

The particle size is a good example of how difficult it can be to adopt known calculations. First, the very complex particle size distribution often observed with nuclear slurries poses an immediate mathematical challenge. Second, the uneven distribution of particle sizes across the entirety of a theoretical vessel holding nuclear sludge further complicates not only calculation but also increases the amount of sampling necessary to obtain a representative measurement. This factor also applies to other properties influencing rheological behaviour of suspensions, such as pH or temperature. Lastly, the measurement itself presents errors that can propagate into the calculation results. This is all assuming that the particle size distribution (PSD) can be ascertained at all, which itself presents its own challenge.

3.4 Mathematical Models used to Describe Rheological Behaviour of Suspensions

Various mathematical models have been developed to describe the behaviour of fluids from a rheological perspective. The simplest model one can use is the Newtonian model, shown in (3.1-2). The model assumes perfectly linear response in shear stress to shear rate and can only be applied to some substances, usually in a limited range of shear rates. It is apparent that Newtonian behaviour is the simplest model used to describe fluids, analogous to the behaviour of Hookean solid. Best examples of Newtonian substances are calibration oils, specifically manufactured to have a Newtonian response to shear rate over a range of shear rates as high as possible, however even these substances exhibit Newtonian behaviour only in limited measurement ranges and conditions. Newtonian suspensions are usually very low

volume fraction suspensions where the influence of particles in the liquid remains low. Most suspensions will exhibit non-Newtonian behaviour.

Possibly the simplest model describing non-Newtonian materials is the power law model, depicted in (3.4-1) [53]:

$$\sigma = K\dot{\gamma}^{n-1} \tag{3.4-1}$$

where K (Pa.s^{-n}) is a parameter referred to as consistency index and n (dimensionless) is a parameter referred to as the power law index. For 0<n<1 the fluid can be described as shear thinning, for n=1 the material is Newtonian and for 1<n it exhibits shear thickening behaviour. As it is quite simple, it offers an easy approximation but only rarely are materials shear thinning or thickening consistently across a wide range of shear rates. Two commonly used models try to extend the usable range of the power law model. They assume that at both low shear rates and high shear rates the viscosity asymptotically reaches different values. These assumptions are incorporated into the power law model by introducing two more parameters: η_0 (Pa.s) which describes the viscosity of the material at low shear rates and η_∞ (Pa.s) which describes the viscosity of the material at high shear rates. The Cross model is shown in (3.4-2) and the Carreau model in (3.4-3). It is apparent that while these models expand on the power law model they have certain limitations, mainly in the assumption of asymptomatic behaviour outside of the power law region [61], [62].

$$\eta = \eta_\infty + \frac{(\eta_0 - \eta_\infty)}{(1 + (K\dot{\gamma})^m)} \tag{3.4-2}$$

$$\eta = \eta_\infty + \frac{(\eta_0 - \eta_\infty)}{(1 + (K\dot{\gamma})^2)^{\frac{m}{2}}} \tag{3.4-3}$$

One further consideration that all the models mentioned above omit is the existence of yield stress in some materials. Yield stress in the context of non-Newtonian fluids is a highly debated property. The topic of yield stress will be further elaborated on later in this section, several frequently used models will be described here that incorporate yield stress. The simplest example of this is the Bingham model, as shown in (3.4-4). σ_y is the yield stress (Pa), or the stress needed to induce any shear rate whatsoever. It is also apparent that the model assumes a linear response to shear rate once the yield stress is overcome [53], [63].

$$\sigma = \sigma_y + \eta_p \dot{\gamma} \tag{3.4-4}$$

Other models elaborate on the Bingham model. The Casson model shown in (3.4-5) for example extends the applicability of the model to fluids exhibiting non-linear response in shear stress to shear rate after overcoming the yield stress. A similar and possibly more often used model is the Herschel-Bulkley, as shown in (3.4-6). This model incorporates yield stress as well as potential for shear thinning or shear thickening, effectively being a power law model with a yield stress [64].

$$\sqrt{\sigma} = \sqrt{\sigma_y} + \sqrt{k\dot{\gamma}} \tag{3.4-5}$$

$$\sigma = \sigma_y + k\dot{\gamma}^n \tag{3.4-6}$$

These models are compared in Figure 3-4, showing examples of Newtonian, both power law variations, Bingham, a shear thinning Casson and shear thickening Herschel-Bulkley examples.

There is a range of other models that describe complex behaviours of fluids. Some are varieties of the ones mentioned above such as the Sisko [62] model, that omits the low shear rate viscosity of the Cross model. Furthermore, there are some models taking time dependent behaviour into consideration as well as shear rate dependent

behaviour, such as the Tiu-Boger [63] and other models that can be useful for specific industries.

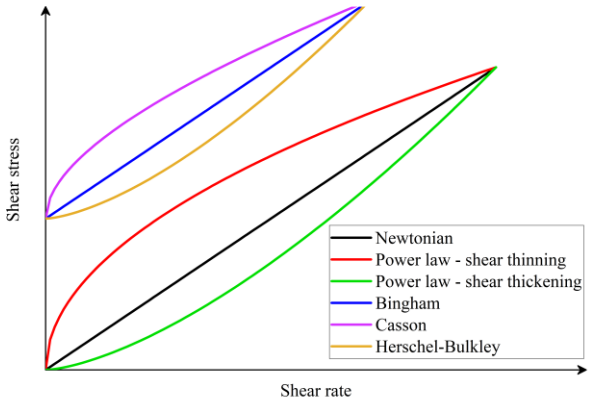

Figure 3-4 Illustration of common mathematical models describing shear behaviour of substances.

All of these models found their use and while they can provide useful information for comparison of materials, there appears to be no universally applicable model for all different materials exhibiting a range of behaviours.

3.5 Benchtop Instruments and Techniques for Rheology of Suspensions

Ascertaining the shear behaviour of suspensions is important not only from a research perspective but also for a wide variety of industries, not only the nuclear industry. As such, different techniques and methods have been developed. This section will provide an overview of commonly used rheological techniques and assess their suitability for suspensions in the nuclear industry.

3.5.1 Rotational and Oscillation Rheometry

Possibly the most widespread instruments are those employing rotational and oscillation shear rheometry techniques. These utilise two pieces of geometry, with one usually being stationary and containing the measured sample and the other being rotated in the sample, thus inducing shear rate. The most common geometries are parallel plates, cone and plate, concentric cylinders and vane and cup geometries,

illustrated in Figure 3-5. All the geometries use a rotating component (orange) connected to the instrument itself with a stem (red) submerged or in contact with the sample (green) contained in a stationary cup (blue).

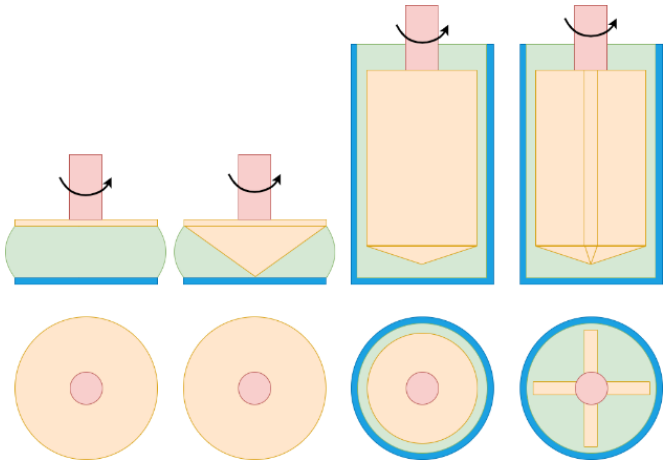

Figure 3-5 The most common geometries used in rotational rheometry, from left to right: parallel plates, cone and plate, concentric cylinders (or bob and cup) and vane and cup.

The parallel disks and cone and plate geometries are popular mainly due to very small sample volume needed for measurements and a high range of shear rates usable with them. The cone and plate geometry has been first proposed as two cones of different angles by Mooney and Ewart [65]. They are not easy to use with suspensions as they are more susceptible to the effects of settling in the material and particle size can dictate the size of the gap between geometries. They are also quite sensitive to misalignment and their design is not particularly suitable for conversion into a non-sampling *in situ* setup, mainly as they require the least amount of torque to shear the material out of all the named geometries, but also due to the most precise sample loading and isolation procedure of all the displayed geometries.

Cup and bob geometry, or concentric cylinder is more prevalent in suspension rheometry, particularly because it is less susceptible to settling effects and is not as sensitive to misalignment. It has been pioneered by Couette in the late 20th century [66]. Throughout the years, different configurations have been used with regards to

which component is the rotor and which one is stationary. These construction differences can be explained by construction convenience, as the mathematical models for all combinations have been developed. Concentric cylinder arrangement is often referred to as Couette flow and several assumptions are made when analysing the flow in the system [46]:

- The flow of the substance is assumed to be steady, laminar and happens at a constant temperature.
- The effects of gravity and end effects can be considered negligible.
- The only displacement is due to the rotating cylinder and/or cup.
- The angular displacement of the sample is symmetric.

The concentric cylinder arrangement is illustrated in Figure 3-6. In this system, L is the length of the cylinder (mm), r_i is the radius of the internal cylinder (mm) and r_o is the radius of the outer cup (mm). The ratio of the internal cylinder radius to the outer cup radius is often referred to as κ (dimensionless). As the most common arrangement is rotating cylinder and a stationary cup, all calculations will be presented for that arrangement.

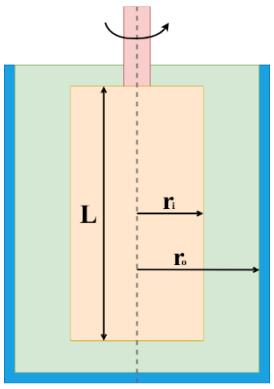

Figure 3-6 Standard cup and bob geometry, the inner cylinder is orange, outer cup is blue, sample is green and the connecting stem is red.

The equations describing the shear rate and shear stress calculations have been extensively described by [46] for example. Using a torque balance, the governing

equation for calculating the shear stress in the gap between the cylinder and the cup has been established as:

$$\tau_{r_i} = \frac{M_i}{2\pi r_i^2 L} \tag{3.5-1}$$

where M_i is the torque on the cylinder (N·m). An assumption is made that when the gap is very narrow (κ>0.99) one can neglect the curvature and consider the shear to be calculated the same way as in parallel plates. The shear strain can be calculated as follows:

$$\gamma = \frac{\theta \bar{r}}{r_o - r_i} \tag{3.5-2}$$

where θ is the angular displacement of the bob and $\bar{r}$ is the midpoint of the gap between the cup and the cylinder (mm):

$$\bar{r} = \frac{r_o + r_i}{2} \tag{3.5-3}$$

From this, one can calculate the shear rate in the gap between the components as:

$$\dot{\gamma} = \frac{\Delta v}{\Delta r} = \frac{\Omega \bar{r}}{r_o - r_i} \tag{3.5-4}$$

where v is the velocity of the cylinder on its surface (mm·s^{-1}) and Ω is the rotational velocity of the cylinder (s^{-1}). Gaps as narrow as κ>0.99 are not common in instruments, and in wider gaps the shear rate varies across the gap. As such, to re-evaluate the shear rate calculations one must measure the velocity profile in the gap or consider the shear rate a function of shear stress. In this case, shear rate can be expressed from the deformation tensor as:

$$\dot{\gamma} = \frac{\delta v}{\delta r} - \frac{v}{r} = r\frac{\delta \Omega}{\delta r} \tag{3.5-5}$$

and it can be made a function of shear rate as:

$$\dot{\gamma} = r\frac{d\Omega}{dr} = 2\tau\frac{d\Omega}{d\tau} \tag{3.5-6}$$

For a rotating cylinder and a stationary cup this can be integrated to express the rotational velocity:

$$\Omega = \int_{\tau_{r_o}}^{\tau_{r_i}} \frac{\dot{\gamma}(\tau)}{2(\tau)} d\tau \tag{3.5-7}$$

For power law fluids in the gap and the gap of a size κ>0.5, assuming the power law index does not change within the gap, the true shear rate at the rotating cylinder can be expressed as:

$$\dot{\gamma} = \frac{2\Omega}{n(1-\kappa^{\frac{2}{n}})} \tag{3.5-8}$$

where n is the power law index that can also be expressed using the rotational velocity and torque on the cylinder:

$$n = \frac{d \ln M_i}{d\, ln\, \Omega_i} \tag{3.5-9}$$

The main consideration with measuring concentrated suspensions using the cup and bob geometry is wall slip. Wall slip occurs mostly with suspensions, polymers and other non-Newtonian substances. A thin layer of lower viscosity material forms around the rotating cylinder due to the reduction of concentration of suspension near the walls, causing the instrument to output seemingly lower viscosity. An extreme case of wall slipping is material fracture, when the rotating bob simply slips on the surface of the material without shearing it [46], [53]. Smooth cylinders are most

susceptible to this and because of this reason, two alternative geometries can be used. First, a roughened cylinder is a useful alternative to a smooth surface cylinder and helps to lower slipping. Second, a vane has become a very commonly used tool for concentrated suspensions, as it lowers slip susceptibility significantly but also presents a second beneficial characteristic – due to the smaller cross-section, it is much easier to insert into materials and disturbs samples less than a cylinder that has to displace the sample much more [67].

A second issue with rotating cylinder is the end effects – the shearing occurring at the bottom of the geometry contributing to the torque output. There are several ways commonly used to minimise or account for these effects illustrated in Figure 3-7. The first is simply calculating the contributing torque caused by the effect and using it in data processing. The issue is the unequal shear rate across the diameter of the bottom surface. The second option is using a recess on the bottom of the geometry that traps air. This air serves as insulation from the material and the friction contribution of the cylinder bottom rotating in air is considered negligible. Lastly, using a conical surface on the bottom of the cylinder with an appropriate angle helps equalise the shear rate across the entire surface of the cone with the shear rate in the gap between the walls [46], [53] .

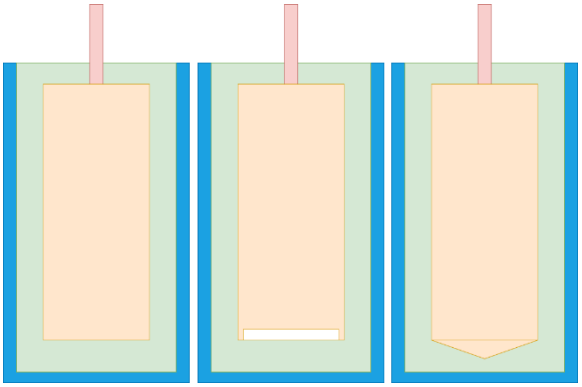

Figure 3-7 End effect correction designs in concentric cylinders, from left to right; uncorrected, air gapped design, conical end design.

The most common vane construction is a thin walled four-bladed vane, illustrated in Figure 3-8. From a shear stress and shear rate calculation perspective, the vane is treated as a cylinder of equal diameter (indicated with a dashed line). An assumption is made that the volume of sample within this assumed cylinder is not sheared and simply rotates with the vane (purple). The shearing is assumed to take place outside of this assumed cylinder instead (green).

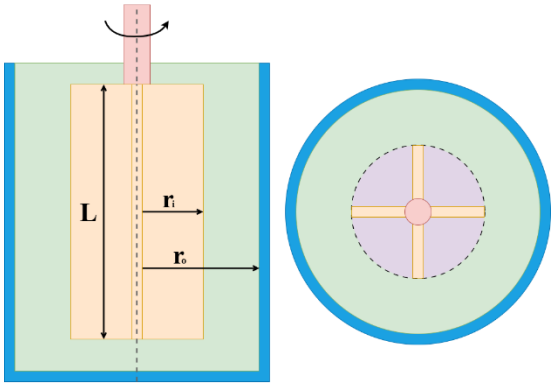

Figure 3-8 Four bladed vane (orange) in a sample (green and purple) with an outer cup (blue) connected to the instrument with a stem (red).

The main disadvantage of using vanes is increased susceptibility to secondary flow effects [46], [68]. This can limit the measurement range when using the vane, as the secondary flow effects appear above a certain shear rate. The onset of these effects has been investigated with concentric cylinders, but the literature is lacking in terms of vanes and especially suspensions. This topic is further discussed in chapter 3.5.1.1. The low susceptibility to wall slip and performance at low shear rates make it a popular tool for yield stress measurements. Some of the most recent literature focuses on the optimisation of the vane shape, opening a discussion about non-standard blade arrangements [69]. Another disadvantage can be a larger volume of sample necessary to conduct a measurement compared to other geometries.

3.5.1.1 Secondary Flow Effects in Rotational Rheometry

Assumptions introduced in the previous section include simple shear flow only due to the rotating geometries. However, in real life applications other motions can occur in rotating shear flows. These are described as secondary flows and their existence can affect the measurement output. The first type of these motions are Taylor vortices. These have been described by Taylor in [70] where the author observed and quantified the onset of secondary flow effects in two rotating cylinder arrangement. These occur due to the inertial forces in the fluid and can be observed as small vortices symmetric around the axis of rotation. A dimensionless number has been established to quantify the onset of these vortices and is referred to as Taylor number (dimensionless). The number can be calculated as [46]:

$$Ta = \frac{\rho^2 \Omega^2 (r_o - r_i)^3 r_i}{\eta^2} \tag{3.5-10}$$

It has been established that for Taylor numbers lower than 3400 the motion is considered to be stable and free of Taylor vortices. It is worth noting however, that this applies to Newtonian fluids in narrow gaps and concentric cylinders. Research investigating the effects in suspensions using vanes is not available, perhaps because using vanes in rheology is still considered a more practical rather than academic approach. Manufacturers often suggest that vanes are more susceptible to secondary flow effects and limit their use to lower shear rates. This means that the stability defining value is likely to be different from 3400.

A second method of defining flow stability in concentric cylinders is the Reynolds number (sometimes referred to as rotational Reynolds number in this context) using the same assumptions as in calculating the Taylor number. The Reynolds number can be calculated as [46]:

$$Re = \frac{\rho\Omega(r_o - r_i)r_i}{\eta} \tag{3.5-11}$$

Since both of these calculations have been developed for concentric cylinders, Newtonian substances and narrow gaps with standard geometries and there is a noticeable lack of literature specific to the conditions outlined in this thesis, it is hard to draw conclusions about potential values indicating the onset of secondary flows. It is still worth calculating both Taylor and Reynolds numbers however, as they are not computationally difficult to ascertain and can provide baseline data for future research.

3.5.1.2 Summary of Common Rotational Viscometer and Rheometer Designs

The distinction between viscometers and rheometers is not very well defined and it appears the difference is mostly due to manufacture's decision to make a distinction between their offered devices. Some sources make the distinction in the capability of the device, for example in the available range of shear rates the device can output or the measurement types it can perform. The most concise differentiation possibly is that a rheometer can measure the flow properties of substances whereas a viscometer can only measure viscosity [71], [72].

The first electronically driven viscometers acquired the torques applied to the sample. The viscosity was then ascertained as the function of the resistance the sample has when a component is rotated in it. Some of the oldest designs, as expected, used dials or gauges to indicate viscosity [73], a simple method that has survived on some cheap viscometers to this day [74].

Most viscometers measure the torque supplied to a rotating cylinder and have a stationary cup [75], [76]. More modern designs output data electronically and enable measurement of rotational velocities as well, often with the capability to control them

precisely [77]. The torque measurement method has evolved as well, but remained fundamentally the same to this day even in portable designs [78], and designs for remote measurement in hazardous environments [79].

There are portable viscometers available, however they are often not suitable for suspensions and can be very sensitive to mechanical damage due to improper use. They are generally made for quick quality control checks on the spot at the cost of lower precision and measurement range [80], [81].

Rheometers are generally larger and more complex in construction than viscometers. While they are not vastly different from viscometers, the increased emphasis on measurement capabilities drives the use of more complex and precise components. Some designs drive the outer cup and use the bob or other geometry to sense the torque transmitted through the material [82]. However, the more prevalent design layout is a driven bob with a stationary outer cup. These are benchtop instruments with rigid frames and a breadth of complex, sensitive electronics used to obtain the best possible accuracy and repeatability. These systems include mechanisms and sensors to enable normal force measurements for automated loading and other measurements and high precision angle encoders used to enable closed-loop measurements [83]. Rheometers often use air bearings in order to lower friction as much as possible, thus improving the sensitivity of the mechanism [84]. Furthermore, they often use various heat exchange technologies to control and maintain the temperature of the sample [85].

It is apparent that rheometer design has evolved in order to improve the accuracy and repeatability of the measurements. This introduces its own drawbacks. First, high accuracy components such as optical encoders are expensive to manufacture and very

sensitive to harsh environments. Second, lowering friction using air bearings is very effective, but also expensive, sensitive to damage due to improper use and requires auxiliary systems to provide compressed air. Lastly, controlling sample properties from a temperature or pressure perspective is crucial in order to normalise results across various samples, but requires precise sampling procedures and more auxiliary systems and sensors.

Viscometer design has evolved in a similar trend, quality of components has improved and enabled higher precision measurements of desired properties. Viscometers found their place in quality control applications, as their capability is not substantial but are cheaper to manufacture and can be tailored relatively easily to specific ranges expected. While they could be considered more robust than rheometers in terms of harsh environments and improper use, the available modern designs are still focused on precision and user convenience, increasing the amount of electronics and highly sensitive components.

Probably the most relevant viscometer example are the Brookfield viscometers. Although they have evolved from their initial design, fundamentally they still perform the same function. They supply rotational velocity to a geometry, such as a vane, and measure the torque required to rotate it in a sample. An example of how this is achieved can be found in [86]. The design depicted in Figure 3-9 outlines the function of this device. A stepper motor drives a spindle through a gearbox, dial assembly and a pivot assembly. This way the output torque is measured through the output shaft and can be read using the dial. While relatively mechanically simple, this design only allows reading of data using the dial, is relatively large and some components, such as the jewelled bearing, make it relatively fragile.

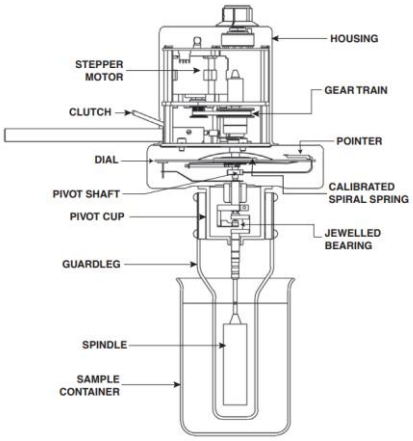

Figure 3-9 Diagram of a modern Brookfield viscometer [86].

3.5.2 Falling Ball Method

Falling ball and similar rheometry methods are possibly the simplest rheometry methods one can use. Other variations of this method include falling cylinder/piston and rolling ball method. The falling ball method involves allowing a weighted ball to travel through a container of sample due to gravitational acceleration. The speed can either be measured or calculated from the time it takes the geometry to travel through a defined distance. It is apparent that the viscosity of the material will be inversely proportional to the speed of the ball. As the method is incredibly simple it does not provide very comprehensive assessment of the shear properties of material and is more of an indicative test rather than a complex measurement method [46].

Even though it is potentially relatively easy to modify this method for an *in situ* measurement mechanism the limited measurement output it provides makes it less usable than rotational viscometry and the interpretation of results is not as straightforward as the method suggests [87], [88].

3.5.3 Capillary Rheometry

Capillary rheometry is an example of a different type of rheometry to rotational shear rheometry. It falls under a category often referred to as pressure driven methods. Fundamentally, all of the variations of this method utilise pressure to drive the

material through an opening of a certain shape and size, observing the flow rate and pressure. The shear rate is calculated using the geometry of the opening the material flows through and the flow rate of material. The shear stress is calculated using the geometry of the opening the material flows through and the pressure in the system [46].

Capillary rheometers are often very similar to process lines in a lot of industries, making them very relevant to, for example, the polymer industry. For the same reason, they can also be used as in-line measurement devices. They reach high shear rates and are relatively simple in construction. However, they can suffer from wall slip issues that are not easily corrected. Loading them with samples makes them a difficult candidate for use *in situ* and in one measurement cycle they only provide a limited amount of data. Furthermore, pressure driven systems heavily relying on sampling pose a number of contamination and retrieval issues for the nuclear decommissioning industry. All of these considerations make the capillary rheometry method an unlikely candidate for this work [89]–[91].

3.5.4 Quartz Crystal Microbalance

Quartz Crystal Microbalance (QCM) is one of the newest methods used for rheological measurements. This is a novel method observing the oscillation frequency of materials in order to determine density and viscosity is very similar to microcantilever devices. Only a limited amount of research discusses them in a context applicable to this work and it suggests this technology is in very early stages of development. The compact size of the devices makes it appealing for *in situ* applications, however data interpretation is relatively complicated. At this stage, it seems unlikely this technology can be developed using rapid prototyping techniques [38], [92].

3.6 Yield Stress Measurements

3.6.1 Existence of Yield Stress

The existence of yield stress in liquids and suspensions is a debated topic. As discussed above, some mathematical models readily adopt yield stress and assume its existence. The existence of yield stress however appears to contradict what defines liquids as it is an inherently solid quality. Some sources, such as [93] argue that yield stress is a concept used to idealise how materials behave and that liquids always flow, albeit extremely slowly at low shear rates. Other sources argue against this statement, using, for example, falling ball experiments to show that even after very long observation times, in some substances the falling ball will not show any observable movement and thus prove the existence of yield stress [94], [95]. The author of original thesis about non-existence of yield stress later wrote another publication [96] where he addresses various articles and continues the discussion. The main factors that contribute to the lack of agreement can be summarised by two main points:

First, some definitions used in the discussion are up for discussion themselves – such as what is ‘flow’? The theoretical/mathematical view would be different from the engineering perspective. This is connected to technical limitations of experiments we perform, highlighted in the point below.

Second, there are limits to what one can observe using state of the art equipment and proving indefinite effects is hindered by finite amount of time available and the inability to absolutely ensure defined and stable conditions.

One thing remains true, regardless of how yield stress is defined and used, it has been accepted by various industries as it serves a real purpose – initiating flow is important

in pump design for suspensions for example. As such, different methods have been created to measure yield stress that will be outlined below.

3.6.2 Common Yield Stress Determination Methods

First, one can use the mathematical models described in previous sections to extrapolate the shear stress curves to $\dot{\gamma}$=0. The point where this curve intercepts the y-axis can then be considered as the yield stress. It is apparent however that depending on the model used, the yield stress extrapolated using this method will differ. It is a simple method useful when no more data is available but produces reliable results only for well-defined substances. This is sometimes referred to as an indirect method for ascertaining yield stress.

3.6.2.1 Stress Relaxation Method

In this method, the measured substance is sheared at a constant shear rate or shear stress. The applied shear is then stopped. The residual stress being applied to the measurement geometry (for example a vane as discussed in section 3.5.1) is then measured. This stress is considered to be the yield stress according to this method [67]. The method has been further refined by applying increasingly high shear stress values and allowing the substance to relax after each cycle while observing the residual stress [97]. There are several drawbacks in this method, mainly the fact that the sample is sheared before yield stress is measured. Unless the sample is not affected by shear history, this will have direct impact on the quality of the measurement. Further issues include inertial and damping effects that are not easily reconciled.

3.6.2.2 Creep-Recovery Method

In this method, a constant shear stress is applied to the substance and the strain is observed, until after the shear stress is stopped. Figure 3-10 shows the effect of this on purely viscous and purely elastic substances. Viscous materials flow and as such their strain (sometimes referred to as creep angle in this method) increases and then remains constant upon removal of stress. In elastic materials the substance immediately deforms and remains deformed before fully recovering upon removal of stress. Viscoelastic materials exhibit a mixture of these properties. The material can be described as both flowing under stress and elastically recovering after the removal of stress [67].

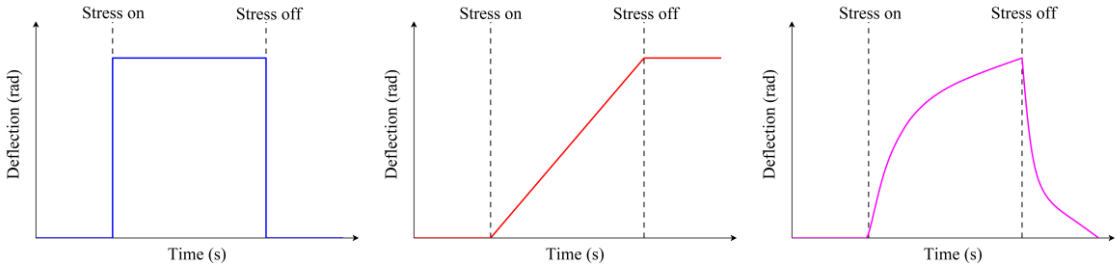

Figure 3-10 The effect of instantaneous application and removal of stress on an elastic material (blue), viscous material (red) and viscoelastic material (purple).

In non-Newtonian samples, this procedure is done in incremental steps of shear stress and an example response is shown in Figure 3-11, where $\sigma_1 < \sigma_2 < \sigma_3 < \sigma_4$. In this example, when the sample is exposed to shear stress of σ_1 and σ_2 the sample reaches a strain where it stops flowing, as noted by the lack of further deflection before the stress stops. It can be seen that the response is not purely viscous, it is often referred to as visco-elastic behaviour, which applies to the recovery as well. At higher shear stresses (σ_3 and σ_4) it flows without reaching a point where the substance stops flowing even when subjected to shear stress. It can therefore be inferred that the yield stress falls somewhere between σ_2 and σ_3. The main disadvantage of the method can be significant time frames associated with acquiring observable strain under very low

stresses with some substances. This links closely to the existence of yield stress being a discussed topic. Inertial and damping effects can be observed in this method as well and while the deformation of material is less significant than in stress relaxation method it can still play a role in shear-history sensitive materials.

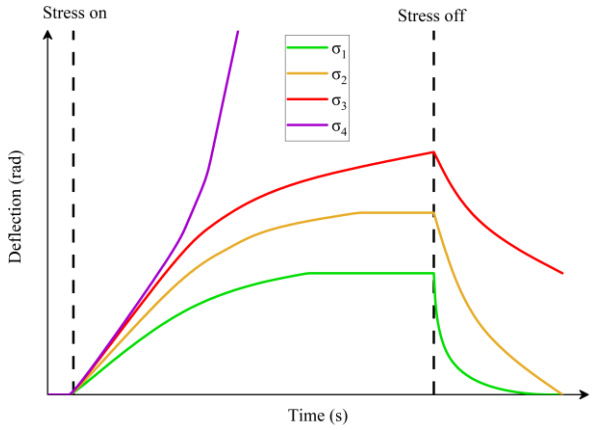

Figure 3-11 Example curves obtained when measuring a viscoelastic substance using the creep-recovery method, where $\sigma_1 < \sigma_2 < \sigma_3 < \sigma_4$.

3.6.2.3 Stress Growth Method

In this method, the measured substance is sheared with a constant shear rate and the shear stress response is observed. The shear rate tends to be very low in these measurements and the method can be considered analogous to tensile strength testing on universal testing machines for solids.

The interpretation of the results is similar to tensile strength testing as well. Two different interpretations of results are usually discussed and used in literature and in technical documentation for rheological instruments. An example of measurement data is illustrated in Figure 3-12. Some sources propose that the start of deviation from a linear response (point 1 in Figure 3-12) to a constant shear rate is the yield stress. This argument is usually supported by the view of viscoelastic behaviour and the linear portion of the response being indicative of the elastic region. The other approach is that the peak stress observed (usually manifested as an overshoot as

illustrated in the example as point 2) is the yield stress of the substance. This approach is used in some official standards as well, although it appears to be dependent on the shear rate used. The drawbacks of the method are similar to the previous ones, with inertial effects being the main one.

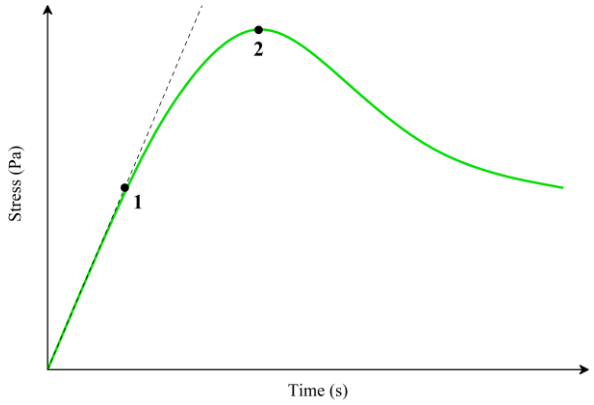

Figure 3-12 Example of stress growth data illustrating the deviation from linear response (1) and an overshoot of stress (2) before the stress starts to equalise.

3.6.2.4 Stress Ramp

Modern rheometers that offer precise control of rotational velocity and/or torque and often support closed-loop control. Two options are then possible to provide a stress ramp. In a torque-controlled rheometer this is achieved by supplying incremental steps of torque and monitoring the rotational velocity as the output. In a strain-controlled rheometer the device uses the torque output as feedback control to precisely control the rotational velocity in order to obtain the shear stress ramp.

In both cases, the output rotational deflection or velocity (recalculated as shear strain or shear rate) is displayed as a function of torque (recalculated as shear stress). The yield stress is then the maximum value of shear stress at zero shear strain or rate. The limitations of this is the rotational position sensing precision and the torque resolution. The main consideration is how quickly this shear stress ramp is performed. This leads back to the initial question - if observed for long enough, would the material flow

when subjected to stress we would call yield stress? For practical reasons, the measurement time must be limited. The best practice is then to use the same measurement time across all samples to enable comparison. This is also why it can be difficult to compare date from different sources and devices.

3.7 Rheology of Suspensions in the Nuclear Industry

Available literature dealing with the rheology of non-active suspensions in the context of the nuclear industry is predominantly focused on simulants (or test materials). Data describing active materials is rare. Some literature uses rheological data as a basis for the development and optimisation of decommissioning technologies [98] or to inform strategies and decision making in a wider context [99].

Literature focused directly on the rheology of suspensions in the context of decommissioning activities discusses mostly Hanford and Sellafield sites. Rheological data is often included as part of a wider range of analytic methods employed to describe a novel test material in a robust way or draw conclusions about the connection between the different properties of the suspension [100]–[104]. The investigations vary, [100] investigates the yield behaviour as a function of pH which is valuable in terms of re-suspending the suspensions if needed. [101] provides a complex analysis of several test materials such as TiO_2, zirconium molybdate and caesium phosphomolybdate (CPM) from a variety of viewpoints, including rheology. [102] provides a comparative dataset between predicted and actual rheological behaviour. [103] investigates the concentration effect of CPM on the rheological properties and analyses the time depended and yielding behaviour of the suspensions too. Some literature focuses on specific properties and their influence on the rheological properties, predominantly the concentration of solids in the suspension as seen in [105], [106], and zeta potential and pH [107]. Yield stress is also discussed in

some of the literature. While the method is usually outlined, the details of the measurement necessary for comparison of data are rarely provided. This makes it difficult to put the datasets mentioned above for direct comparison.

Literature discussing the rheology of suspensions as the main topic is not as common. Some literature aims to analyse the specific rheological properties of test materials, such as time-dependent properties [108] or attempting to ascertain what mathematical model describes the test material appropriately [109]. As nuclear suspensions do not appear to behave any differently than other suspensions, purely rheological investigations on nuclear suspensions and test materials are not common.

One important aspect to note about nuclear suspension rheology is that it is heavily focused on the analysis of test materials and sampled material. *In situ* measurements are not reported on in the available literature.

3.8 Conclusions

A wide array of instruments and methods for rheological measurements is available for use, not only in the nuclear industry. The understanding of rheological behaviour of suspensions is well established and most up-to-date literature on nuclear suspensions focuses on outlining their behaviour rather than proposing novel theories or discovering new phenomena. This indicates that nuclear suspensions do not exhibit any unusual behaviour and the main challenge in ascertaining their properties is due to the hazards associated with acquiring and performing measurements on samples.

There is also a lack of *in situ* instruments used to ascertain the rheology of nuclear suspensions. The most commonly used instruments used for measuring nuclear suspensions are rotational rheometers and viscometers, relying on sampling the materials or using test materials. Current development of commercially available

instruments is focused on increasing precision, measurement ranges and automation – all of which are appealing to most industries focused on production. That however does not remedy the challenges of sampling and handling hazardous materials. New methods, such as QCM have been proposed as viable for this application, but they have not been used in active environments yet. Rotational rheometry is the most viable method to be incorporated into an *in situ* instrument, as it provides best comparison with *ex situ* methods and poses the least amount of risk while not sacrificing the available precision.

It is apparent that yield stress in suspensions is surrounded by many questions and discussion, from the very existence of it to the methods of determining it and interpreting the data. It appears that from an application perspective, industries have adapted to this by adopting a certain technique and using in to compare samples between themselves rather than establish absolute measurements. To an extent that seems to be the case for rheology overall, as different industries have needs for different ranges of data. This can however make it difficult to compare data from various sources if all the necessary details of the measurement procedures are not outlined.

Fundamentally, not one method provides a more established or precise yield stress measurement than the others. From an application perspective, stress ramp method is possibly the most representative method to illustrate how movable the tested material is. It is also not very time consuming and is potentially one of the least complex methods to implement. Creep-recovery method can provide a more complex picture of the yield behaviour of the suspension but is also very time consuming and requires a more complex mechanical and sensor system. The stress growth method is possibly the easiest method to implement at the cost of providing only limited amount of data.

Stress relaxation method is the least usable method, as it requires pre-shearing the material. That makes it inappropriate during *in situ* measurement in hazardous environments, as one can expect a limited amount of time and measurement attempts with undisturbed material.

4 Shear Rate Ramp Prototype

This chapter presents the first prototype design made to ascertain rheological properties of sludge remotely in a compact package while using a minimal amount of potentially sensitive electronics. It was developed using novel prototyping techniques and the design allows further modifications that would allow for deployment in hazardous environments. In summary, the aim design specifications for the developed prototypes described in chapters 4 and 5 are:

- Compact design that would allow the device to fit through a 50 mm diameter opening.
- Overall prototype mass of less than 1 kg to maximise deployment capabilities.
- Remote operation and data acquisition.
- Sealed design allowing complete submersion if necessary.
- Non-sampling measurement technique to minimise contamination and material removal from measurement location.
- Measurement method that allows direct comparison with commonly used laboratory equipment and provides a measurement focused on analysing the movability of suspensions of viscosity between 0.1 and 50 Pa·s.

4.1 Overview of the Device

The first prototype developed is fundamentally a rotational viscometer using a selection of measurement geometries. The prototype has been developed using COTS components, 3D printing of various components and rapid prototyping electronic platforms. This approach makes the device very cheap and quick to prototype and manufacture. The prototype diagram is shown in Figure 4-1.

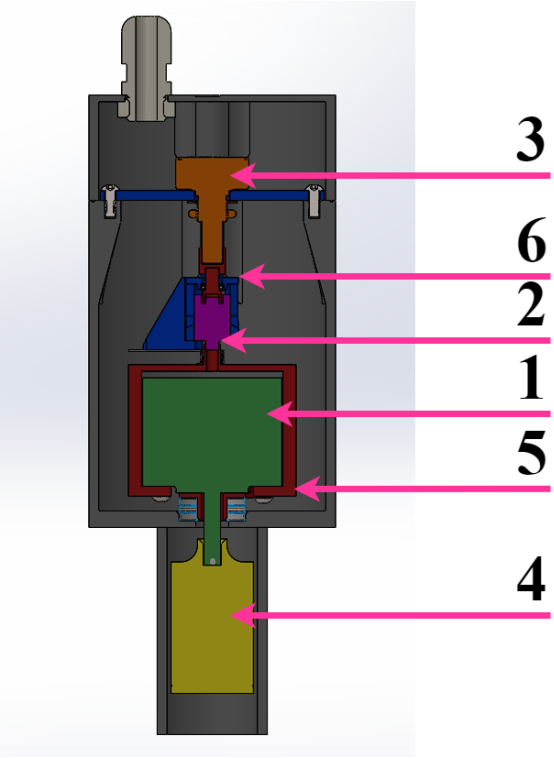

Figure 4-1 Overview of the shear rate ramp prototype.

As depicted in Figure 4-1, the mechanism consists of the following key components: stepper motor (1), slip ring (2), potentiometer (3), measurement geometry (4), rotating frame components (5), static frame components (6). The prototype rotates the measurement geometry in a sample and the mechanism is used to determine the torque required to perform the rotation[2]. The data is then interpreted in order to determine the shear properties of the sample.

4.1.1 Torque Measurement

There is a wide variety of methods available for measuring torque. The main considerations when developing a way to measure torque in this example were spatial limitations and the inability to use sensitive and complex electronics. Spatial constraints stem from the specified size limits placed on the device and rule out the vast majority of commercially available load cells. The inability to use sensitive components further limits the option of using very common methods of force and

[2] Larger size pictures can be found in the Appendix at the end of this document.

torque measurement such as strain gauges and piezoelectric elements. These limitations steered the development toward a more mechanical approach.

There are two options used in rotational viscometry used to ascertain torque in the system caused by shearing the sample. The first option is to measure the torque on the rotating geometry, the second option is to measure the torque on the static outer cup. As the cup is surrounded by the sample on both sides it is significantly more complex to design a torque measurement system on the cup side. For this reason, the torque is measured on the rotating geometry.

As seen in Figure 4-2 the stepper motor (1) is held by a bracket (2) that is connected to the frame using an axial bearing (3) at the bottom end and to a slip ring (4) at the top end. The slip ring allows the stepper motor to continuously rotate around the same axis as the axis of rotation of the output shaft of the motor without twisting or deflecting the connector cables. The slip ring housing is fixed to the frame using a bracket (5). Lastly, there is a torsion spring (marked 6, model Associated Spring Raymond T017-270-156-R) attached to the slip ring bracket (5) on one end and to the stepper motor bracket (2) on the opposite end.

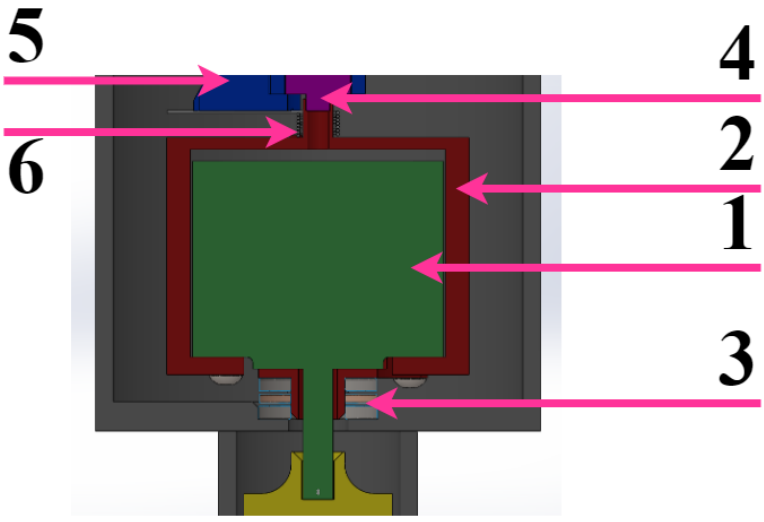

Figure 4-2 Motor placement withing the prototype.

As shown in Figure 4-3 the upper side of the rotating part of the slip ring (1) is connected to a potentiometer (2) shaft. The potentiometer itself is also affixed to the frame using a bracket (3). In this configuration, as the stepper motor (4) rotates the measurement geometry in the sample, the reaction torque on the geometry from the sample due to the viscosity of the sample rotates the stepper motor in the opposite direction. Assuming the stepper motor rotates the geometry with a constant rotational velocity and the viscosity of the sample does not change, the mechanism reaches an equilibrium when the spring is increasingly deflected until the torque is equal to the reaction torque from the material. The deflection of the mechanism is measured using the potentiometer, as the potentiometer shaft is connected to the rotating components inside of the case.

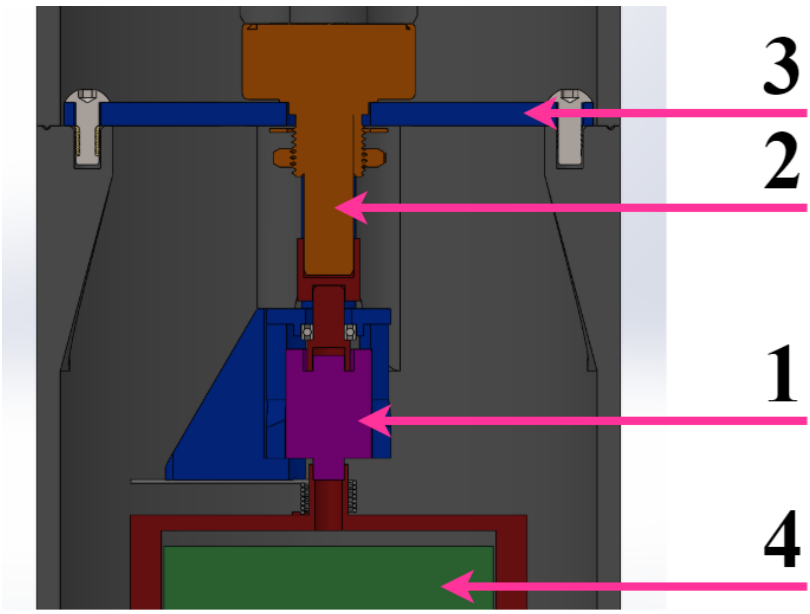

Figure 4-3 Upper portion of the prototype mechanism.

4.1.2 Materials Used to Manufacture the Prototype

3D printing has seen tremendous growth over the past several years, allowing users to rapidly prototype components much quicker and cheaper than using conventional methods. It also allows for creating complex shapes and internal structures not possible to be manufactured without compromises when using conventional methods.

Recently, 3D printing has become widely available to the general public and consequently a variety of materials useful for a wide range of applications have become readily available for use in research as well.

Possibly the most widely used 3D printing material is Polylactic Acid (PLA) based filament. The popularity of this material stems from three main points – it is cheap, easy to use and biodegradable. Biodegradability is both a benefit and a drawback, it enables an environmentally conscious approach to early prototypes but prevents the use of PLA in long term applications. The material has good build plate adhesion and has very good mechanical properties. The main drawback of PLA is the very low glass transition temperature, meaning PLA gets soft at very low temperatures. The combination of all these factors make PLA most suitable for early prototypes and components not exposed to harsh environments. As such, in the first prototype PLA has been used for a wide range of components utilising its stiffness and ease of use such as the casing and internal linkages.

Acrylonitrile Butadiene Styrene (ABS) has been a very common polymer used in various industries since the 1950s, made using injection moulding or machining. As a 3D printing material, ABS quickly became recognised as a very good material for functional prototypes. The mechanical properties are not as good as those of PLA or even injection moulded components made with ABS and the material is more complicated to print with. However, the thermal stability of the material and good chemical resistance make it a better choice than PLA in some applications.

Co-polyester (CPE) made by Ultimaker is a good example of “transparent” 3D printing filament. While often referred to as “transparent”, when used in 3D printing the components made with CPE are translucent, as the layering of the material has an

impact on the optical properties. Nevertheless, this translucency can often be beneficial not only for presentation purposes but functional too - for example to monitor material level when used to make containers. CPE exhibits good mechanical properties but is not as resistant to elevated temperatures as ABS. It is not particularly easy to print with, but it has very good chemical resistance making it useful for a wide range of applications.

Lastly, an example of a very specialised material is XSTRAND^{TM} GF30-PP. This is glass-fibre reinforced polypropylene offering very high chemical resistance, highest thermal stability of all the materials discussed so far and very good mechanical properties. These properties however mean the material is much more expensive than the previous materials. The presence of glass fibres in the material also makes it very abrasive, which means the 3D printer must use specialised components to prevent accelerated wear of the nozzles and extruders. Post-processing of the material (such as filing and polishing) is also complicated, as the glass fibres are very dangerous when inhaled. All of these considerations make this the most useful material for specific components exposed to very harsh environments and short run manufacturing, such as development of applications for harsh environments.

Table 4-1 Comparison of mechanical properties of readily available 3D printing materials for prototyping [110]–[113].

	Ultimaker			XSTRAND™
	PLA	**ABS**	**CPE**	**GF30-PP**
Tensile strength at yield (MPa)	49.5	39.0	41.1	60.0
Flexural strength at yield (MPa)	103.0	70.5	79.5	83.0
Maximum usable temperature (°C)	50	85	70	120
Chemical resistance	Low	Medium	High	High
Manufacturing considerations	Low	Medium	Medium	High

Generally speaking, structural components were printed with a layer height of 0.2-0.4 mm and 100% infill using a 0.4 mm nozzle. Moving, small and press-fit components were printed with a layer height of 0.1 mm and 100% infill using a 0.25 mm nozzle. Components made with XSTRAND™ GF30-PP have been printed using a specialised 0.4 mm nozzle at 0.4 mm layer height and 100% infill.

4.1.3 Outer Case

The outer case serves also as the frame, providing a fixed point to anchor stationary components. In this initial prototype it is not sealed but is designed to enable easy sealing for potential future versions. It is entirely portable and is made from PLA, as the only requirement for the case is sufficient stiffness. It consists of two sections, the main frame and a lid that can be bolted to the frame. The frame houses the lower race of the axial bearing further mentioned in the following sections and has mounting points for the potentiometer bracket. The lid has a cable gland bolted to it fixing the wiring in place to prevent it from interfering with the moving components. In a

deployment scenario it would also serve as a physical tether allowing or providing a backup method of recovery – important for deployment in any nuclear facility.

4.1.4 Measurement Geometries

Five different measurement geometries have been made to be used with the prototype with corresponding outer cups that can be mounted to the main frame of the prototype. The dimensions of two of the measurement geometries and their complementing outer cups are based on the ISO 3219 [114] standard conventionally used with commercially available instruments. Their dimensions are the equivalent of C25 bob and cup and V25 vane and cup configurations on the benchtop, laboratory scale Bohlin CVO100 rheometer. Three more four-bladed vanes have been designed and manufactured as well, as depicted in and outlined in Table 4-2. These non-standard geometries have been created for two reasons. First, the torque required to shear the material can be too low to be detected by the proposed mechanism and increasing the torque measurement sensitivity may require use of more sensitive electronic devices or expensive, bespoke manufacturing. Second, from a deployment perspective there is no guarantee as to the material height that is to be assessed. Partial submersion of the measurement geometries prevents the acquisition of usable data. The standard ISO geometries require a substantial material height to be fully submerged which may prove to be prohibitive in some deployment scenarios in the context of deployment on nuclear sites.

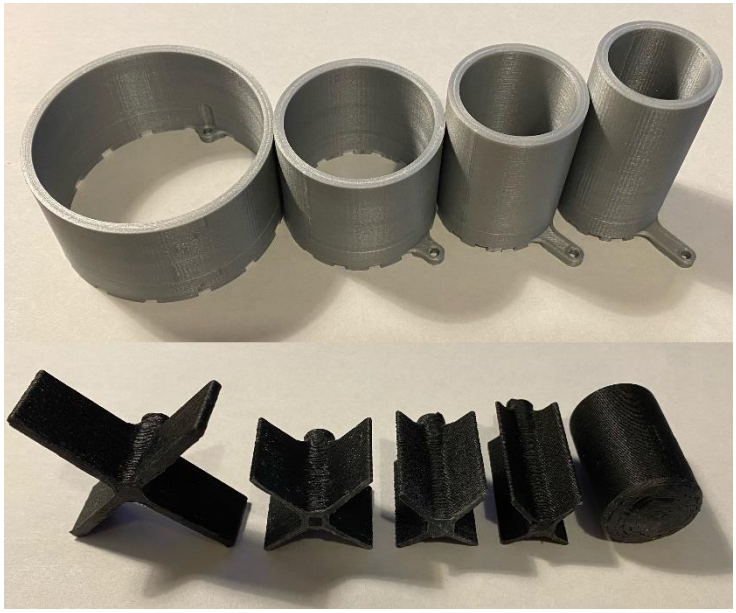

Figure 4-4 Top: cups printed with silver PLA, from left to right – 3, 2, 1, ISO. Bottom: geometries printed with XSTRAND™ GF30-PP, from left to right – 3, 2, 1, ISO V25 Vane, ISO C25 bob.

It has been discussed in the rheology chapter that the main parameter that governs the conversion of rotational velocity to shear rate is the ratio of cup radius and geometry radius. To that extent all of the used geometries have the same ratio in order to make them as comparable as possible. To lower the material height requirements the non-standard vanes have been shortened and the diameter of the vanes has been increased to increase the torque necessary to shear the material.

All of the geometries, including the ones based on ISO standards deviate from this standard in several regards. The device can only be deployed by inserting it into the sample and so the bottom of the cup is open to allow the sample to fill the outer cup and submerge the measurement geometry. The outer cups are mounted to the frame and as such the cup is closed at the top, unlike the traditional benchtop arrangement that has the cup closed in an inverse fashion. The outer cups also have openings at their very top edge to allow air to escape the measurement volume when inserting the instrument into the sample.

Table 4-2 Overview of the different geometries with the prototype.

	ISO Bob	ISO Vane	Vane 1	Vane 2	Vane 3
Cup radius r_o (mm)	13.75	13.75	16.50	22.00	33.00
Geometry radius r_i (mm)	12.50	12.50	15.00	20.00	30.00
Geometry length L (mm)	37.50	37.50	30.00	20.00	15.00
L/r_i (-)	3.00	3.00	2.00	1.00	0.50
Necessary sample height (mm)	52.50	52.50	42.50	32.50	27.50

4.1.5 Drive

There are four fundamental options for supplying energy to the system to provide rotational movement of the geometries:

- Electrical
- Mechanical
- Pneumatic
- Hydraulic

In harsh environments, especially radioactive environments the main consideration for deployment of any technology is risk mitigation, mainly in the context of contamination. This immediately points to hydraulic and pneumatic systems not being suitable for these environments. The risk of using these power supply methods is twofold. First, any failure of systems that leads to introducing more material to the radioactive environment - such as leaking hydraulic systems - increases the amount of radioactive waste and creates a risk of adverse reactions between the hydraulic medium and the waste itself. Second, any failure that leads to change in environmental

conditions - such as increase in vessel pressure due to leaking pneumatic systems - creates more risk that was not necessarily present before the attempted deployment.

This leaves mechanical and electronic power supply and drive options. Mechanical option, such as a spring-loaded mechanism is a robust choice for harsh environments as it is inherently less susceptible than electronic devices to damage due to radiation. However, in the context of an *in situ* rheological tool for hazardous environments there is little to no research that has been undertaken to explore this option. For a first prototype of such a device it is more appropriate to use a well-established drive mechanism.

All of the considerations above lead to electrical-type drive mechanism to be used in the first prototype. The most common, readily available electronic drive mechanisms that fit within the specified size limits are direct current (DC) motors and stepper motors.

There are two considerations when choosing between the two motors for this application - rotational velocity control and available torque. The requirement for the drive mechanism is to supply rotational velocity in the range of 1 to 200 rpm with sufficient torque across the entire range. The torque is estimated not exceed 13 N·mm based on the test materials and geometries described in following chapters. The velocity range covers the pre-defined shear rate range using the geometries described in previous sections, allowing direct comparison to the benchtop rheometer.

Due to the construction of the stepper motor rotational velocity control is much easier than with DC motors. As long as the stepper motor does not slip, precise timing of the pulses guarantees desired rotational velocity without the need to use external sensors. The main disadvantage is the smoothness of the output, as the movement of the output

shaft is always a series of discrete steps. Using microstepping helps rectify the lack of smoothness and increases control of the output at the expense available torque. Furthermore, the torque decreases as the rotational velocity increases, limiting the maximum rotational velocity of the stepper motor. Stepper motors are able to supply zero velocity torque, allowing for a very smooth transition from no movement to low rotational velocity.

DC motors have the benefit of smoother motion than stepper motors and higher sustained torque with rising rotational velocity. Speed control without sensors is not as easy as with stepper motors and they also perform poorly at low rotational velocities, making transition from no rotational velocity to motion much less smooth than stepper motors.

Due to these considerations a stepper motor controlled using a microcontroller and a stepper motor driver has been selected as that selection minimises the amount of electronics in the prototype itself and allows for easier control of rotational velocity.

The motor has been selected based on a variety of criteria. First, it must fit within the working envelope of the working prototype. Second, it must provide the highest step resolution available. Third, the voltage and current rating should be as low as possible to minimise the power required and amount of electronics needed to run the selected configuration. Lastly, the torque the stepper motor provides must be sufficient across the entire measurement range with all the proposed geometries.

4.1.6 Electronics of the Device

The necessity of ensuring no components sensitive to radiation are present inside of the prototype has been repeated several times and applies to the electronic design as well. One could divide the electronics used into two areas, depending on where they

are located. The majority of components are detached from the prototype itself in order to prevent their degradation due to radiation. In deployment scenarios these components would be with the operator of the instrument and have been concentrated in a housing made from PLA. This set of components will be referred to as the control unit.

Two of the electronic components are physically present inside of the prototype that would be exposed to harsh environments and potentially radiation too. These components are the stepper motor driving the mechanism and the potentiometer measuring the deflection of the mechanism. Radiation tolerance is discussed in more detail in chapter 6 and the radiation testing performed on the potentiometer used in the prototype is described in section 6.8.1 and the radiation testing of the microcontroller in section 6.8.3.

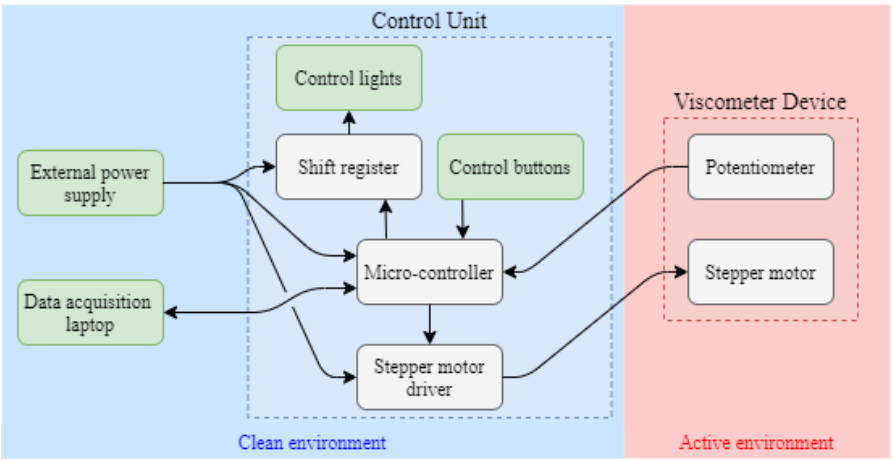

Figure 4-5 Layout of the electronic components of the prototype and the associated devices. Red illustrates components exposed to harsh environment, blue is clean environment with the operator, green components are operator facing/controlled [115].

4.1.6.1 Circuitry

The core of the control unit is the micro-controller, in this case the Cortex®-M4F based Teensy® 3.6 platform. This represents a readily available COTS solution enabling both control and data acquisition for the prototype. The programming was done through using the Arduino language and IDE with the control code for this

prototype using three open-source libraries to facilitate the function of the Arduino language on the microcontroller board (using the Arduino.h library [116]), communication with the stepper motor driver (using the DRV8834.h library [117]) and timing without using blocking functions (using the Chrono.h library [118]). These libraries have been used in the other chapters of this thesis as well. The microcontroller is connected to a COTS stepper motor driver board (Pololu DRV8834), the potentiometer (Bourns 6630S0D-C28-A103), a shift register (74HC595) and two buttons. The main requirements for the potentiometer were small size, continuous turning and low turning torque – these have narrowed down the available units significantly. The shift register is then connected to four LED indicators mounted in the lid of the control unit and the stepper motor driver board is connected to the stepper motor itself. The indicators display the different states of the device. The signal noise from the potentiometer is lowered by using a small capacitor, specifically a 0.1 μF ceramic capacitor. The external power supply provides power to the stepper motor driver, shift register and the microcontroller. The complete control unit is approximately 100x80x53 mm in dimensions.

The stepper motor driver is supplied with 5.8 V and the microcontroller limits the current the stepper motor can draw to 250 mA. While this decision limits the amount of torque the motor can transfer, it lowers the vibrations produced by the motor when running. It has also not proved to be detrimental during the experiments described below, as no slip of the stepper motor has been observed.

4.1.6.2 Measurement Procedures

Two main procedures have been programmed to the microcontroller. The first is a zeroing procedure helping to eliminate all deflections inflicted by deploying the device in order to establish the zero-tension position. The procedure rotates the

geometry in the sample in an opposite direction to the measurement rotational direction until it deflects the mechanism to a set point. It then slows down to zero and indicates measurement readiness using the LED on the control unit. The procedure is triggered by one of the control buttons.

The second main procedure is the measurement, during which the prototype supplies a range of rotational velocities to the geometry in a logarithmically spaced, increasing values from a look-up table. Every rotational velocity step is maintained for 12 seconds, allowing the mechanism to settle for six seconds before acquiring data from the potentiometer in the remaining six seconds every 400 ms. Both the time since the start of the measurement and the value from the potentiometer are then saved in the microcontroller memory and then automatically relayed to the DAQ laptop through the serial port connection to be saved.

Microstepping has been used with the stepper motor to increase the step precision and lower the vibrations of the drive. The stepper motor driver is capable of providing up to 32 microsteps per step. It is preferable to use the highest microstepping setting possible and so the device has been tested across the entire used rotational velocity range to determine what microstepping setting can be maintained. The testing showed that 32 microsteps can be maintained between 0-45 rpm, 16 microsteps up to 90 rpm, 8 microsteps up to 180 rpm and 4 microsteps up to 360 rpm. While it would be preferable to use the maximum possible microstep setting across the entire range, under high rotational velocity the impact of lower microstep setting on the vibrations has not been observable. Furthermore, as the highest necessary torque is likely to be necessary at the highest possible rotational velocity, using a lower microstep setting helps improve the available torque.

The complete setup of the prototype and all the used components and devices when running an experiment is shown in Figure 4-6. From left to right, the devices used are: data acquisition laptop, external power supply powering the control unit, the control unit and the prototype immersed in a TiO_2 sample in a beaker.

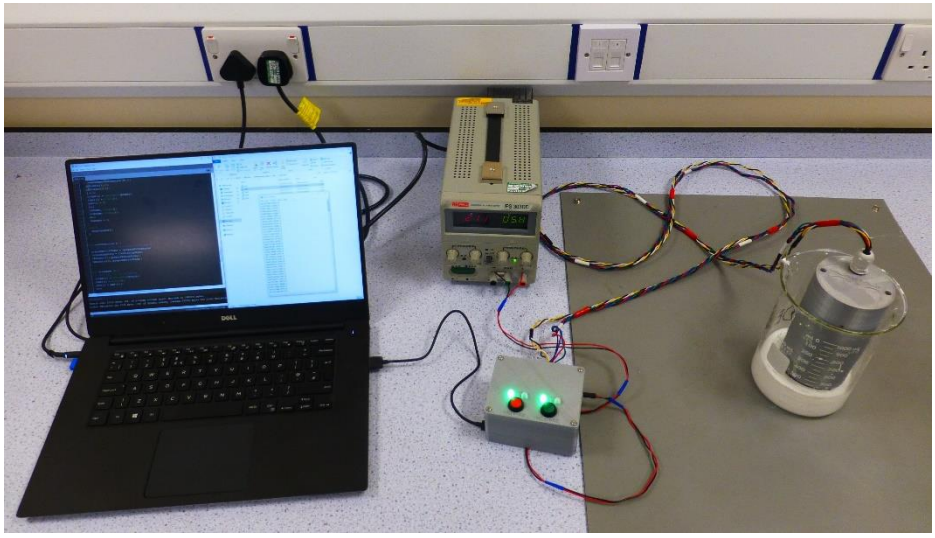

Figure 4-6 The complete layout of the prototype and auxiliary devices during measurement.

4.2 Calibration Procedure

The device is calibrated against a benchtop rheometer, specifically a Bohlin CVO100 rheometer using a silicone viscosity standard oil. The standard used was a 1 Pa.s oil manufactured by Paragon Scientific (VIS-RT1K-600). The shear stress/shear rate curves have been measured using the rheometer with a shear rate ramp of logarithmically spaced values between 0.1 to 100 s^{-1} over 30 s at temperatures of 21 °C ± 1 °C. First measurement was made using a C25 bob and cup configuration, the second using a DIN standard V25 vane and cup configuration. Each measurement consisted of five runs for each geometry and the averaged results and fitted curves can be seen in Figure 4-7. In these measurements the quality of fit is better than $R^2 = 0.99$ indicating almost perfectly linear response of the material to increasing shear rate. The shear rate was converted into the rotational velocity of the geometries using the calibration constants (10.524 for the ISO bob and 4.699 for the ISO vane) obtained

from the benchtop rheometer. This is done in order to enable comparison with the developed prototype using non-standard geometries as will be further elaborated on later in this chapter.

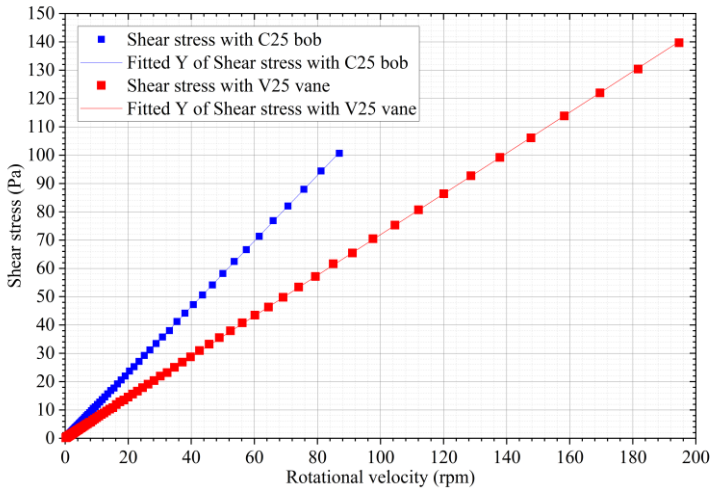

Figure 4-7 Shear stress as a function of rotational velocity of the calibration silicone oil as measured on the commercial benchtop rheometer using a C25 standard bob and cup geometry and a V25 standard vane and cup geometry [115].

The calibration shear rate ramp measurements have been performed with the prototype with all of the proposed geometries. The device supplied rotational velocity in roughly logarithmically spaced[3] values ranging from 1 to 100 rpm on the bob and cup configuration and 2 to 200 rpm on the vane and cup configurations at temperatures of 21 °C ± 1 °C. These ranges correspond to the rotational velocity ranges used on the commercial benchtop rheometer. The torque measurement is read from the potentiometer and saved in bit values ranging from 0 to 65535. These values correspond to the electrical angle range of the potentiometer of 340°, meaning a bit value of 0 equates to approximately 0° of deflection and a bit value of 65535 means approximately 340° of deflection. Values deflecting the mechanism over 1 turn are calculated as 65535 + measured value, although this only happens in vane 3 at very

[3] Deviations from perfectly spaced values are caused by using integer values of rotational velocities in order to simplify and lower the requirements of the code running the prototype.

high rotational velocities. The raw values obtained with the prototype are pictured in Figure 4-8 and Figure 4-9 as a function of rotational velocity. All measurements consist of five runs and the data displayed shows the average value obtained and the standard deviation between all five measurements and the data has also been fitted with linear functions.

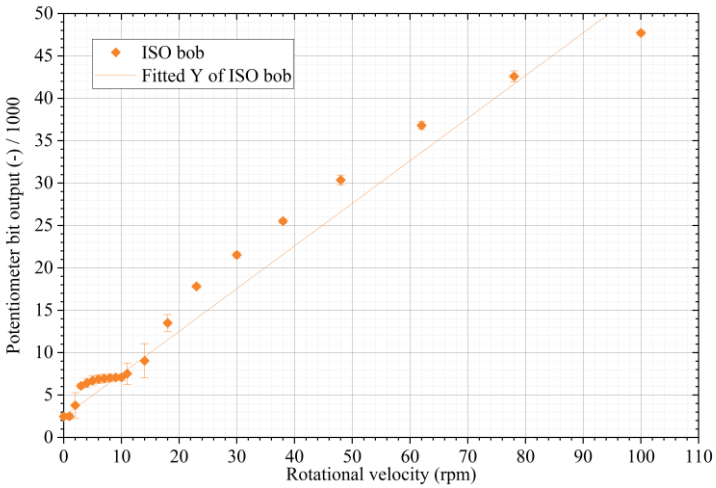

Figure 4-8 Raw data obtained with the prototype when measuring the calibration silicone oil using the C25 standard bob and cup geometry [115].

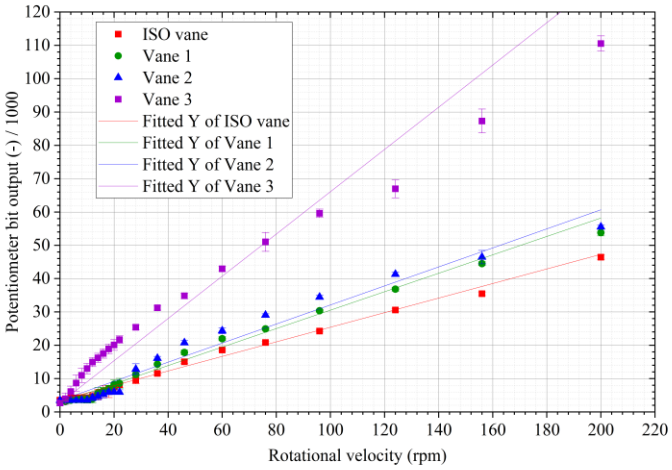

Figure 4-9 Raw data obtained with the prototype when measuring the calibration silicone oil using all vane and cup geometries [115].

Relationship between the data obtained with the prototype and with the commercial benchtop rheometer has been determined by calculating the conversion parameters from raw data obtained with the prototype to shear stress obtained with the rheometer. The overview of the results and quality of fit of these calibration parameters is

provided in Table 4-3. The results indicate that linear functions are suitable for use in the calibration calculation but may require further calculations increase the quality of the data.

Table 4-3 Overview of calibration data obtained with the prototype and commercial benchtop rheometer [115].

	ISO Bob	**ISO Vane**	**Vane 1**	**Vane 2**	**Vane 3**
R^2 of raw data fit (-)	0.9826	0.9970	0.9968	0.9786	0.9793
Slope of raw data fit (-)	502.73	218.72	276.74	285.94	633.86
Slope of benchtop rheometer data fit ($Pa.rpm^{-1}$)	1.1614		0.7197		

After calibration the results of measurements with the calibration viscosity oil have been recalculated from raw data to shear stress and depicted as a function of rotational velocity of the geometry in example in Figure 4-10 and Figure 4-11. The data for other geometries can be found in the appendix. The results indicate that the poorest results overall are obtained with the ISO bob and Vane 2 geometries. The ISO vane and Vane 1 offer good fit and repeatability at higher rotational velocities but provide poor sensitivity to low shear stresses. Vane 3 remedies this low shear stress sensitivity but offers lower accuracy in higher rotational velocities. These results are in line with the expected behaviour, apart from anomalously poor performance of Vane 2.

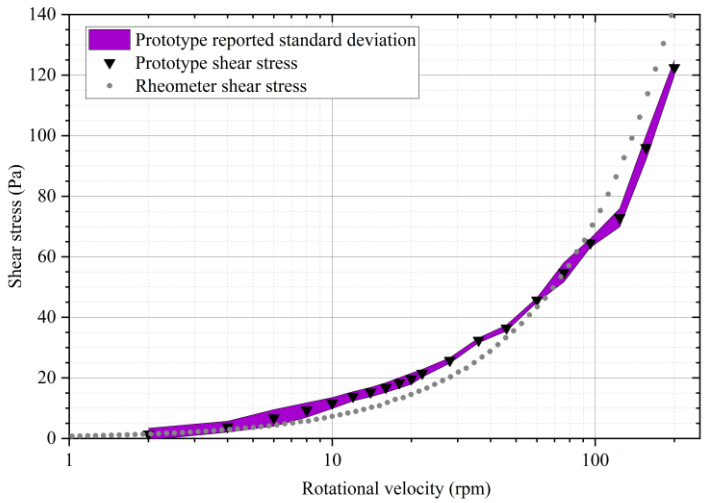

Figure 4-10 Example of final calibration curve. Vane 3 data collected and converted into shear stress including the standard deviation of five runs [115].

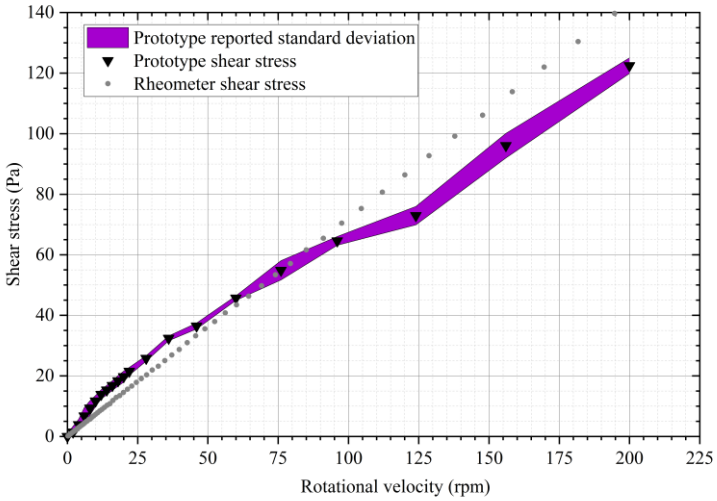

Figure 4-11 Example of final calibration curve for Vane 3 with linear X-axis.

4.2.1 Non-linearity Compensation Procedure

It can be seen from the results in Figure 4-8 and Figure 4-9 that all of the geometries report repeatable deviations from a perfectly linear fit when measuring the calibration oil. The repeatability of these deviations indicates a potential for mathematical compensation. For all of the geometries used the relative deviation from the fitted functions has been plotted against the shear stress measured by the prototype. This illustrates how the prototype under or over-reports based on the value it is outputting. Polynomial functions have then been used to fit the data. High order polynomials are not suitable for this procedure as they introduce errors of their own and as such, the

lowest order polynomial possible has been used on the data only in the necessary range (i.e. in the range of shear stressed observed when measuring test materials as discussed later in this chapter). These fitted functions can then be used to determine the compensation values, for example if the prototype over-reports they can help calculate the necessary value to subtract from the results to output a more appropriate result. The compensated shear stress can then be defined as the measured shear stress minus the value of the compensation polynomial function at that measured value.

It needs to be noted that this compensation procedure must be used with care and only in the range in which the polynomial has been calculated. The range has been selected to cover the widest possible range where measurements have been taken but kept as narrow as possible to minimise the order of the polynomial necessary for a usable fit. Even then it is important to report both compensated and original data. An example of the compensation curve is shown in Figure 4-12 and shows Vane 3 results, including the fitted function parameters (data for Vane 1 and 2 can be found in the appendix).

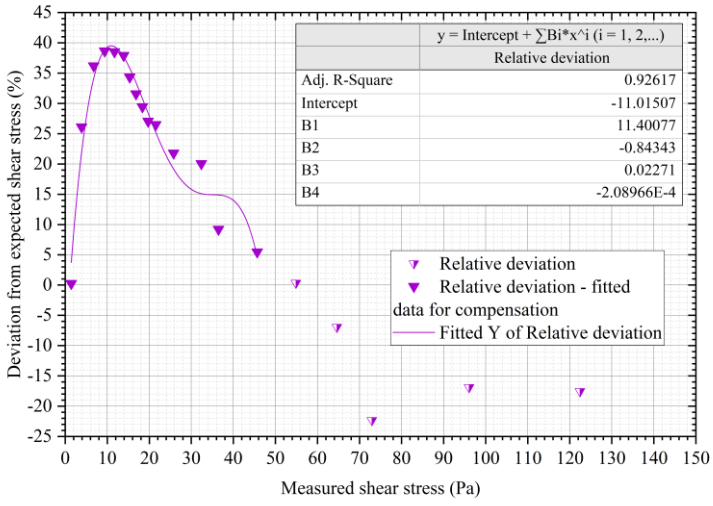

Figure 4-12 Example of compensation curve showing results for Vane 3 including fitted function parameters [115].

4.2.2 Onset of Secondary Effects

The potential influence of secondary flow effects when using rotational rheometry to obtain shear behaviour data has been discussed in chapter 3. While there appears to be no evidence indicating the onset of secondary flow effects in the calibration measurements both Taylor number and rotational Reynolds numbers have been calculated for all data points acquired. These results are indicated in Figure 4-13 and Figure 4-14.

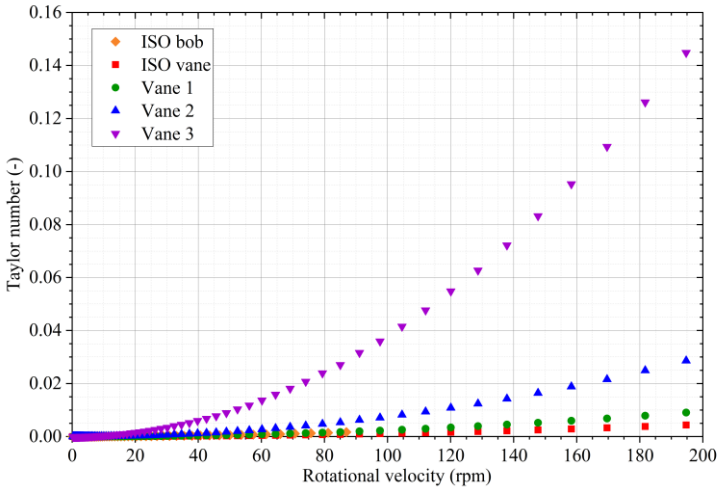

Figure 4-13 Taylor number calculated for all measurement points acquired with the prototype using the calibration oil [115].

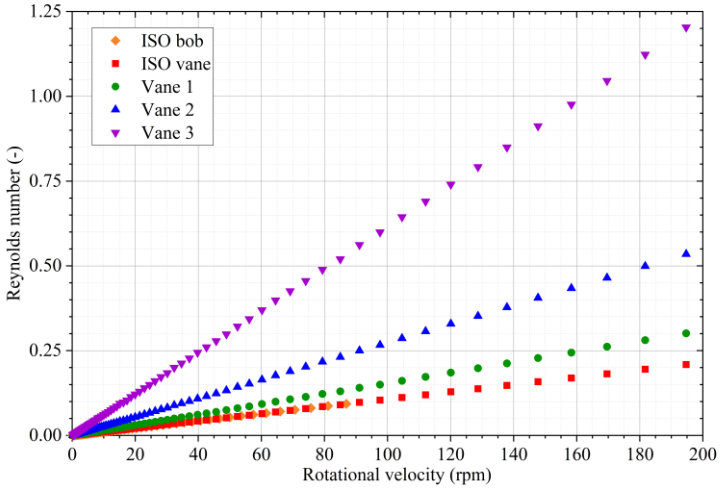

Figure 4-14 Reynolds number calculated for all measurement points acquired with the prototype using the calibration oil [115].

It is apparent both Taylor and Reynolds number are very low across the entire measurement range, which is as expected given the very low rotational velocities involved.

4.3 Measurement Results with Test Materials

4.3.1 Test Materials Used

The first test material used with the prototype was titanium dioxide (TiO_2) in the form of anatase, supplied by Sigma-Aldrich (ID number 248576). The material was supplied as powder which was dried in an oven and then dispersed in de-ionised water in quantities to achieve various volume fractions. This material has been previously used in the nuclear industry as a very safe test material and an example of a low viscosity suspension [101]. While it has been superseded by more complex and representative materials it still remains a good example of lower viscosity suspension (as compared to the following material) and remains a good starting point for the application.

The results performed using a Bohlin CVO100 rheometer on varying volume fractions of the TiO_2 suspensions can be seen in Figure 4-15. The maximum volume fraction that was possible to reach was approximately 0.45. It is apparent that increasing the volume fraction increased the necessary shear stress required to shear the material. Another phenomenon illustrated with this suspension is more obvious when the viscosity is plotted as a function of shear rate and displayed on a logarithmic scale, as seen in Figure 4-16. All concentrations exhibit shear thinning behaviour, but at the very start of the measurement the volume fractions of 0.25 and 0.45 exhibit some shear thickening behaviour. This could also be viewed as an indication of yield stress behaviour.

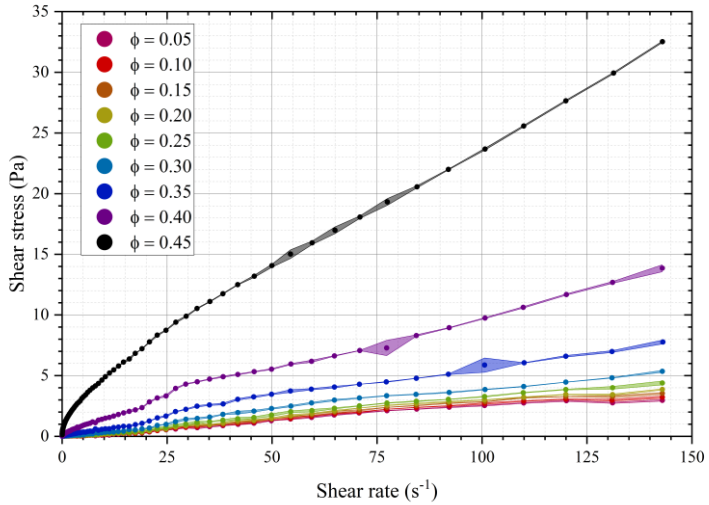

Figure 4-15 Shear stress as a function of shear rate of various concentrations of TiO_2 powder in de-ionised water, measured on a Bohlin CVO100 rheometer at temperatures between 21-23 °C.

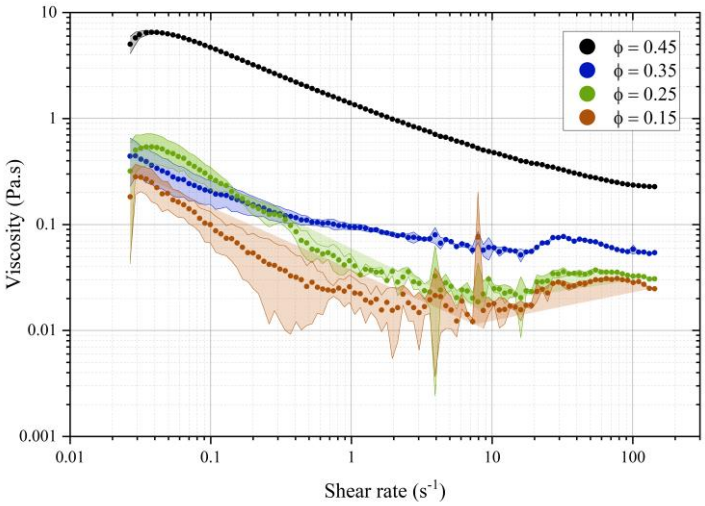

Figure 4-16 Viscosity as a function of shear rate of various concentrations of TiO_2 powder in de-ionised water, measured on a Bohlin CVO100 rheometer at temperatures between 21-23 °C.

Only several volume fractions are depicted to increase the readability of the graph in Figure 4-16 as the standard deviation of measurements at lower volume fractions is relatively high. This also points to the decision to use the highest volume fraction achievable in the testing of both prototypes described in this thesis (ϕ=0.44 in the case of the first prototype). The noise associated with lower viscosity volume fractions would complicate the testing of the prototypes. Furthermore, as the aim for this work is to describe the movability of suspensions that are potentially difficult to move, the

low viscosity concentrations are not representative of the behaviour this work investigates.

The second test material used with the prototype was zirconium molybdate (ZM) suspended in 0.5 M nitric acid. The sample was used as provided in the form of suspension, synthesised by Johnson Matthey for NNL. The supply of the material was limited, but a drying test showed that the mass fraction of the tested material was ϕ_m=0.38. It is a good example of a comparatively higher viscosity suspension with very apparent shear thinning properties. It is one of the most novel test materials used in the nuclear industry [119].

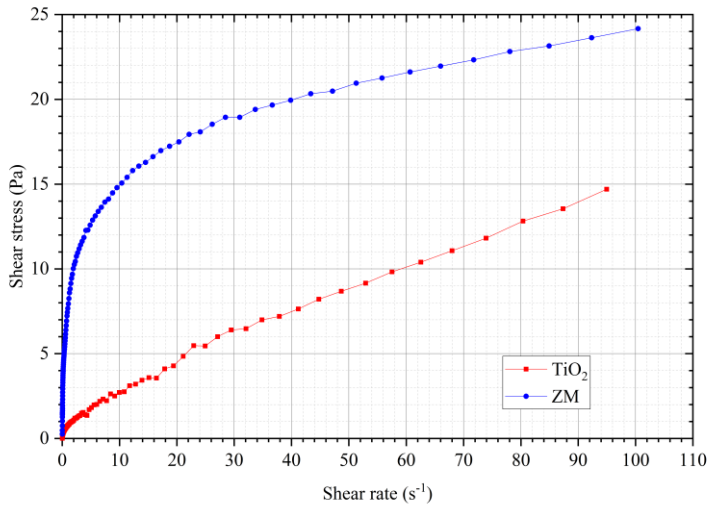

Figure 4-17 Shear curves of the TiO_2 and ZM test materials used to test the prototype with Vane 3.

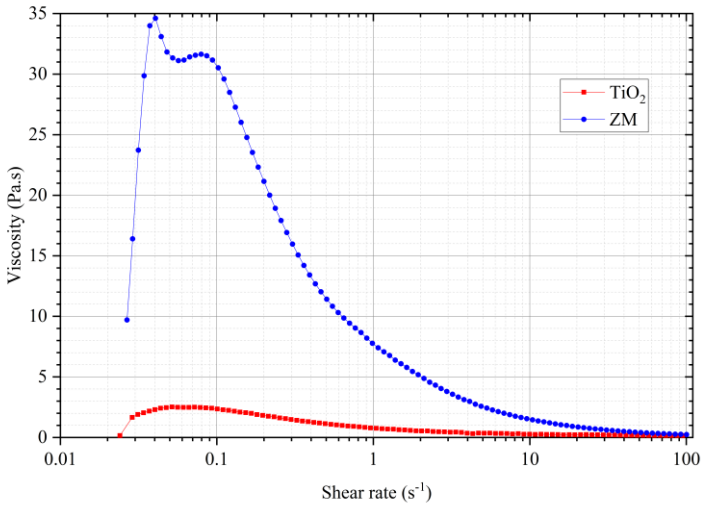

Figure 4-18 Viscosity curves of the TiO_2 and ZM test materials used to test the prototype with Vane 3.

Furthermore, ZM exhibits time history effect behaviour. This is illustrated in Figure 4-19. It is apparent that the time it takes to perform the ramp has an effect not only on the performance of the rheometer (as discussed in more detail in chapter 5) but also on the rheological properties of the material. The quickest measurement reports the least repeatable and also lowest viscosity of the sample, while the slowest indicates the highest, most repeatable measurement.

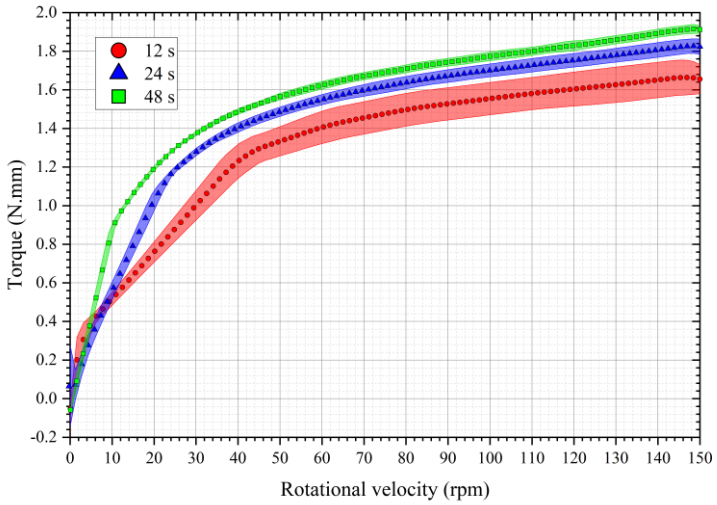

Figure 4-19 Torque required to shear a sample of zirconium molybdate suspension as a function of rotational velocity at different measurement times measured on a Lamy RM200 Plus at 20 °C.

The PSD of both materials has been ascertained using a Malvern Mastersizer 3000 characterisation system using a Hydro EV wet dispersion unit. The measurement with TiO_2 used the stirrer system set to 1800 rpm and was performed at laser obscuration of approximately 3.7%, refractive index 2.493 and absorption index 1. The measurement with ZM used the stirrer system set to 2400 rpm and was performed at laser obscuration of approximately 30.7%, refractive index 1.19 and absorption index 0. The results of the measurements can be seen in Figure 4-20.

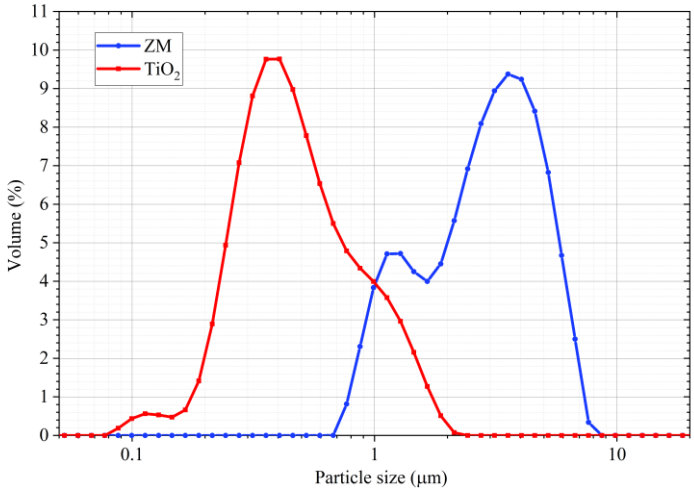

Figure 4-20 PSD of the TiO_2 and ZM test materials used to test the prototype [115].

4.3.2 TiO_2 Results

It has been mentioned that the TiO_2 is an example low viscosity suspension, which as expected proved to be problematic for the smaller size geometries. The shear stress measured in the rotational velocity range has been too low for the ISO Vane, Vane 1 and 2 geometries, limiting the usefulness of the output, as seen in Figure 4-21. With the ISO Vane, the viscosity is below the detection level of the mechanism across the entire range. The compensation procedure has little effect on this. Vane 1 only output usable data in one run out of five while over-reporting significantly. The lack of repeatability causes the wide standard deviation of the measurements. The compensation procedure improves the quality of the data, it cannot however compensate for the poor repeatability. Vane 2 did output some usable data in higher rotational velocities with decent repeatability. The compensation procedure does not seem applicable to these results as they lie outside of the region where the compensation procedure has been calculated. This consequently causes the prototype to under-report as seen in Figure 4-22.

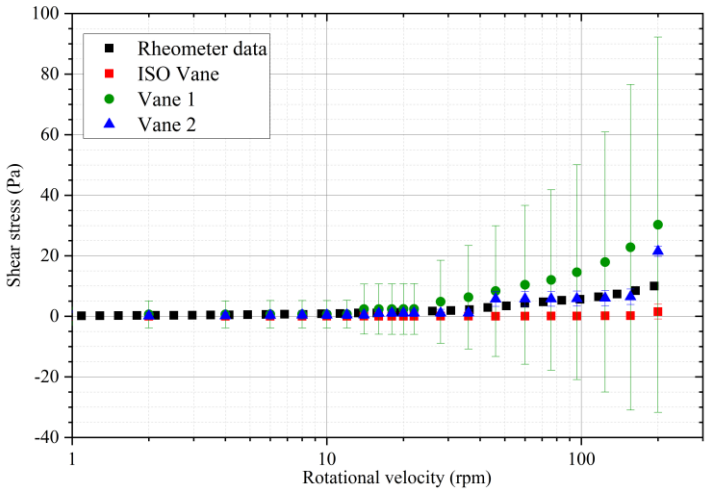

Figure 4-21 Shear stress measured with the commercial benchtop rheometer compared to the results obtained using the prototype with ISO Vane, Vane 1 and Vane 2 before using the compensation procedure.

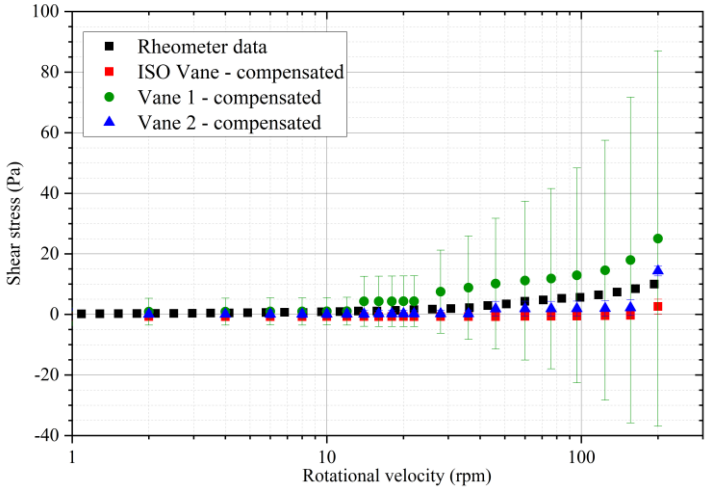

Figure 4-22 Shear stress measured with the commercial benchtop rheometer compared to the results obtained using the prototype with ISO Vane, Vane 1 and Vane 2 after using the compensation procedure.

The results with the ISO Bob are nearly identical to the results obtained with the ISO Vane. The torque is below the detection range of the mechanism and the mechanism only reacted at the highest rotational velocity. This is consistent with the expectations set at the start of the chapter and further reinforces the necessity for non-standard geometries to improve the sensitivity of the prototype.

The Vane 3 results are applicable however, as illustrated in Figure 4-23. The data shown is average of five measurement runs and the standard deviation of the results is displayed in the error bands. It is apparent that the data obtained with the prototype

aligns better with the expected results without using the compensation procedure. The data diverges from the data obtained with the Bohlin at approximately 80 rpm and higher, where both raw and compensated data diverges from the expected results. It is possible that these effects are a result of secondary flows appearing in the measured substance, seemingly increasing shear stress required to rotate the geometry in the sample. The compensation procedure does not change this effect, in fact, it does not seem to be particularly appropriate for a lower viscosity sample like the one measured.

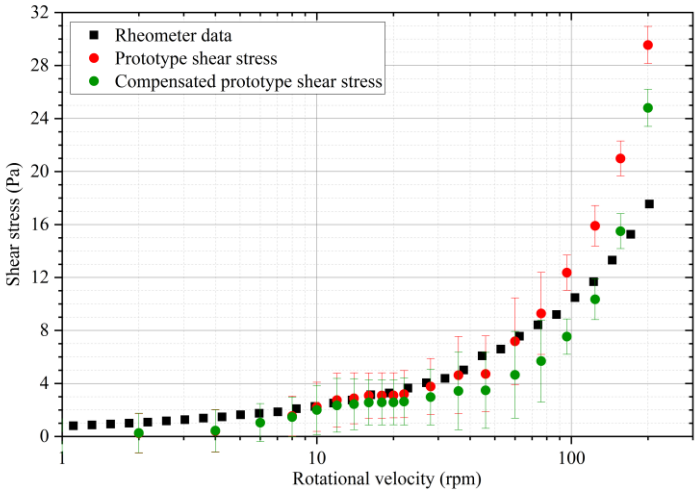

Figure 4-23 Shear stress measured with the commercial benchtop rheometer compared to the results obtained using the prototype with Vane 3 both with and without a compensation procedure [115].

Taylor and Reynolds numbers have been calculated using the data collected with the rheometer but using the dimensions of the used Vane 3. These results are shown in Figure 4-24. The potential secondary flow effects appear at approximately 80 rpm which corresponds to $Ta = 6$ and $Re = 7.5$. These are very low values, mainly compared to the commonly used thresholds for onset of secondary effects in literature (3400 for Taylor number, 50000 for Reynolds number [46]), but that is not unexpected as these calculations have not been used in this context before.

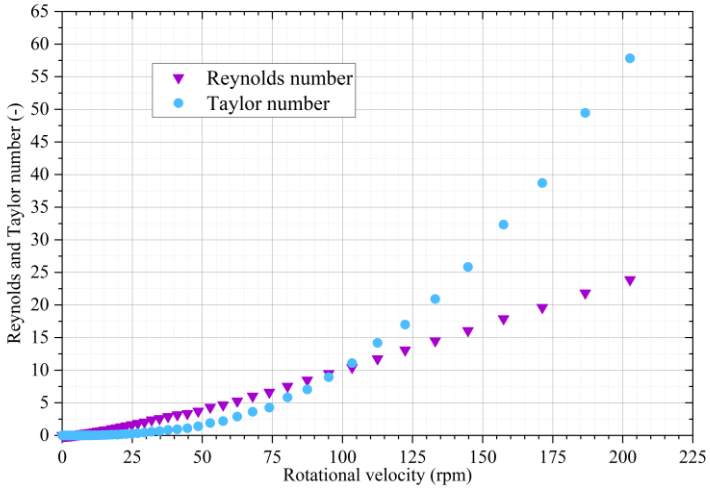

Figure 4-24 Results of the calculation of potential secondary effects occurring in the test material measurements when using Vane 3 on the prototype with TiO_2 [115].

4.3.3 ZM Results

The main expectation from the prototype when measuring the ZM was to capture the shear thinning behaviour. The viscosity of the sample overall is higher than the viscosity of TiO_2 mainly in the low rotational velocity region. The measurements performed with Vane 1, Vane 2 and Vane 3 all provided usable outputs as shown in Figure 4-25.

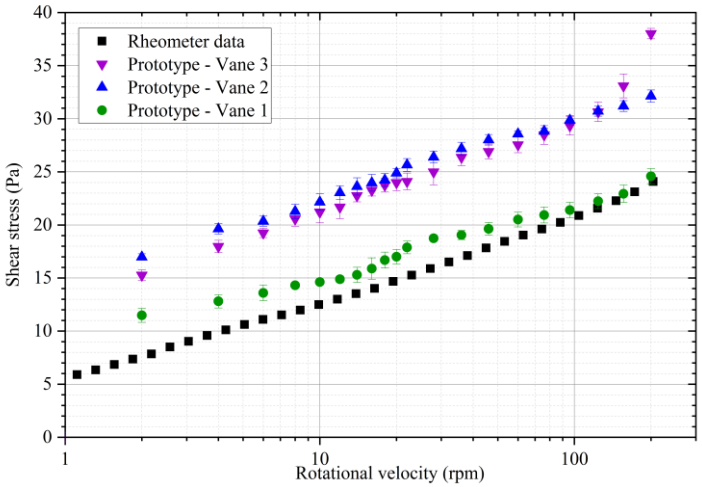

Figure 4-25 Shear stress measured with the commercial benchtop rheometer compared to the results obtained using the prototype with Vanes 1, 2 and 3 before using the compensation procedure [115].

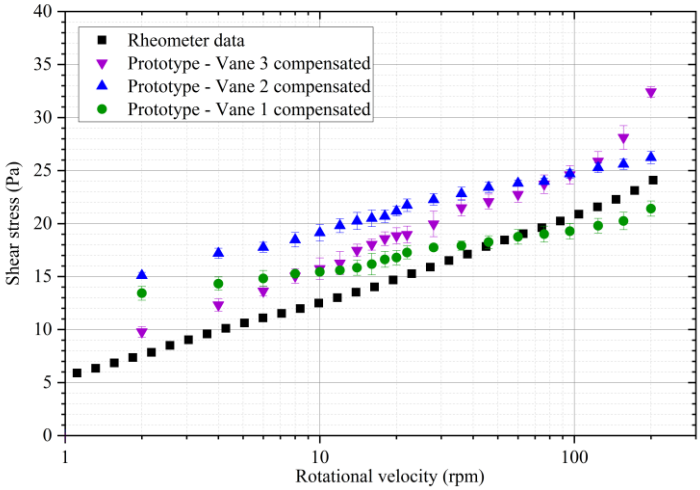

Figure 4-26 Shear stress measured with the commercial benchtop rheometer compared to the results obtained using the prototype with Vanes 1, 2 and 3 after using the compensation procedure [115].

It can be observed that the prototype over-reports using all three geometries, with Vane 1 being affected the least. Vane 2 and Vane 3 results are in agreement, however offset by the same margin before applying the compensation procedure. Before using the compensation procedure, Vane 1 offers the most accurate output of the three geometries.

The compensation procedure does not seem appropriate to use with Vane 1, as it changes the slope of the curve and consequently provides worse output across most of the measurement range. On the other hand, the procedure seems appropriate for Vane 2 and Vane 3 as it decreases the deviation from expected values without changing the slope of the curves significantly. This is more apparent with Vane 3, making the compensated Vane 3 data on par in terms of quality with non-compensated Vane 1 data. Although the Vane 2 results are improved by the compensation procedure, the poor calibration data still makes it the least capable geometry with the prototype.

There is a notable and sudden change in the slope of measured values with Vane 3 both before and after compensation starting at approximately 150 rpm (as opposed to 80 rpm being the assumed start of secondary effects with TiO_2). The compensation procedure appears to have little effect on this which indicates a potential onset of

secondary flows. Secondary effects are expected to be delayed in shear rate ramp experiments when compared to lower viscosity samples, which would explain the difference in the rotational velocities when observing secondary effects.

The potential indicators of the onset of secondary flow effects have been calculated and displayed in Figure 4-27. The only geometry exhibiting potential secondary effects is Vane 3 starting at approximately 150 rpm, which corresponds to Ta = 3.5 and Re = 6. These values are similar to those seen when measuring TiO_2, but equally very low. Vane 1 and Vane 2 do not reach these values in either number, which correlates with the lack of observable effects.

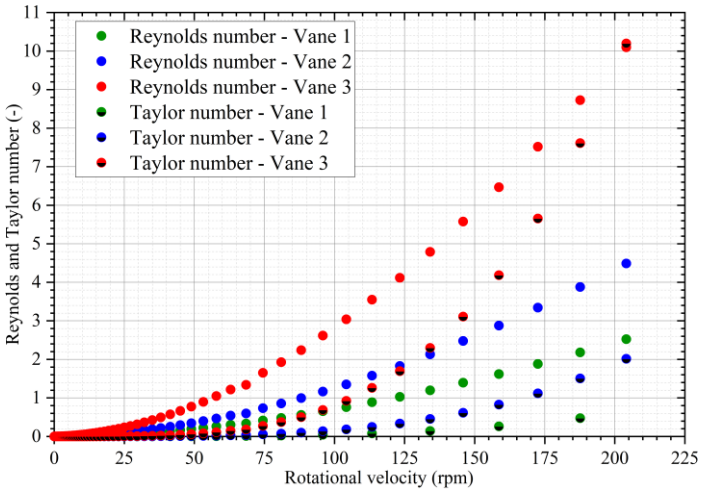

Figure 4-27 Results of the calculation of potential secondary effects occurring in the test material measurements when using Vanes 1-3 on the prototype with ZM [115].

4.4 Conclusions

The prototype described in this chapter can fit through a 75 mm opening and can provide usable, repeatable shear data about suspensions when calibrated against and compared to a benchtop instrument. It also supports the case for use of rapid prototype and use of COTS components to quickly develop functional prototypes. Due to the quick rise in high quality 3D printing components, some materials might also prove robust enough for *in situ* use in hazardous environments.

The calibration procedure using silicone oil to establish the comparison between the prototype and the rheometer proved to be appropriate. Furthermore, this suggests that this comparison can be established using any well-known, repeatably measurable substance that could provide a more pragmatic approach to the data acquisition in some environments.

The measurement range is easily adjustable and does not fundamentally change the calibration procedure. Lowering the measuring range to lower rotational velocities would require an alternative drive system and more precise engineered components to improve the sensitivity of the system. Extending the measurement range to higher rotational velocities does not require complex changes to the system but raises more questions about secondary flow effects that must be considered when analysing the data.

The most important point the development and testing of the prototype has raised is the balancing on three main considerations when choosing the geometry to use *in situ*. Ideally, one would use a geometry adhering to standards commonly employed in the design of benchtop instruments. This in turn however increases the necessity of using precise engineered and therefore expensive components that will most likely have to be custom made, further increasing the lead times to manufacture the prototypes. These standard geometries also require much higher material height to be used appropriately which may not be available in real world *in situ* deployment scenarios. The only option with the standard geometries then is to uniformly scale them down in order to require less material. This in turn however increases the necessary precision of other components even more and raises further questions about the size of the particles relative to the gap between the geometry and the outer wall.

All of these points suggest that it is possible to use standard geometries to measure samples *in situ* using a prototype based on the proposed design, however only at increased cost and most likely moving away from COTS components. Non-standard vanes on the other hand are applicable with the prototype in the ranges used in this thesis. Care must be taken when interpreting the results, especially when using any compensation procedures.

This work provides the challenges for the second prototype described in the next chapter. First, it is the aim to design an even smaller device, preferably to fit through a 50 mm diameter opening. This would further maximise the deployment potential of the device. Second, it is the aim to improve the yield stress detection capability by employing an alternative measurement method. While yield stress can be extrapolated from the results obtained with the first prototype it would be preferable to obtain more robust data about the movability of the sample even at the expense of higher shear rate behaviour.

While there was scope for further testing of the prototype with other test materials the timeline of the project was impacted by the COVID-19 pandemic and a decision was made to focus on the development of the second prototype as progress was achievable with limited laboratory access.

5 Shear Stress Ramp Prototype

In contrast to the first prototype device that essentially provides a shear rate ramp measurement, the second prototype is designed to provide a shear stress ramp measurement. It has been discussed in previous chapters that shear stress ramp measurements are more useful for determining the movability of suspensions. The second prototype has been designed in order to provide a different perspective on the rheological properties of sludges, lower the footprint of the device while maintaining a robust, simple design.

5.1 Overview of the Device

The primary design goal is a device that can output an increasing amount of torque on the output vane in a repeatable way. The prototype size was lowered and could potentially fit through a 50 mm diameter opening. As discussed in previous sections, mechanical solutions are the most likely options to be successfully deployed in hazardous environments and that lead the design choices in this prototype as well. Rather than provide an absolute output, the aim for the device is to provide comparative dataset - similarly to the previous prototype. That enables a more pragmatic approach to data assessment in potential deployment scenarios.

The working principle of the mechanism is outlined below in Figure 5-1. A drive is connected to a torque transmitter and a torque regulator. Its purpose is to supply energy to the system. The torque transmitter serves as a connector to a measurement geometry, a vane in this case. The torque regulator needs to change the amount of transmitted torque during torque transmission. Lastly, a sensor is necessary to monitor the position of the output vane in order to determine the deflection and angular velocity that are used to determine the rheological properties of the sample.

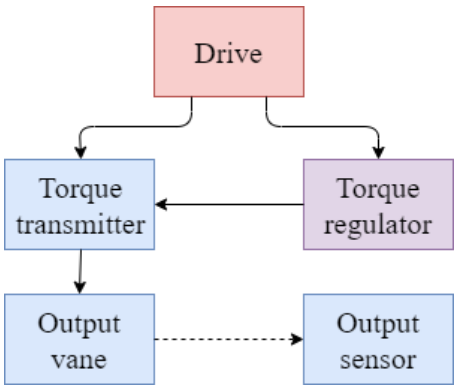

Figure 5-1 The working principle of the second prototype.

The torque transmitter and regulators are based around a friction clutch. A COTS solution usable for this purpose is not available, however it can be adjusted for this purpose. Adjustable friction clutches are a readily available solution that has been chosen to be modified for this design. Specifically, a friction clutch size 25 made by Huco has been used with several adjustments to its construction. A simplified overview of construction of the device is shown in Figure 5-2.

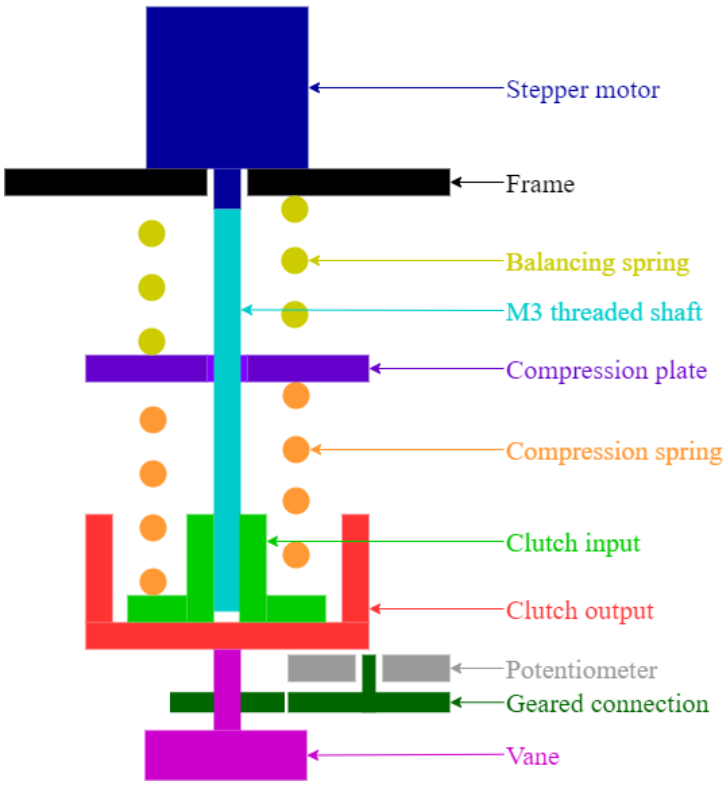

Figure 5-2 Simplified overview of the construction of the second prototype.

A more detailed overview of the prototype is depicted in Figure 5-3, Figure 5-4 and Figure 5-5. The numbering used in the following sections refers to numbering in these figures[4].

The drive is facilitated using a stepper motor (1), the same model that has been used in the first prototype. The stepper motor is fixed to the prototype frame (2) and the output shaft is connected with an Oldham style coupling (3) to an M3 threaded shaft (4) that runs through most of the length of the prototype and is centred at the top using a bearing (5) The other end of the M3 threaded shaft is connected to the input of the clutch. Under all circumstances therefore, the input of the clutch rotates with the same direction and angular velocity as the stepper motor shaft.

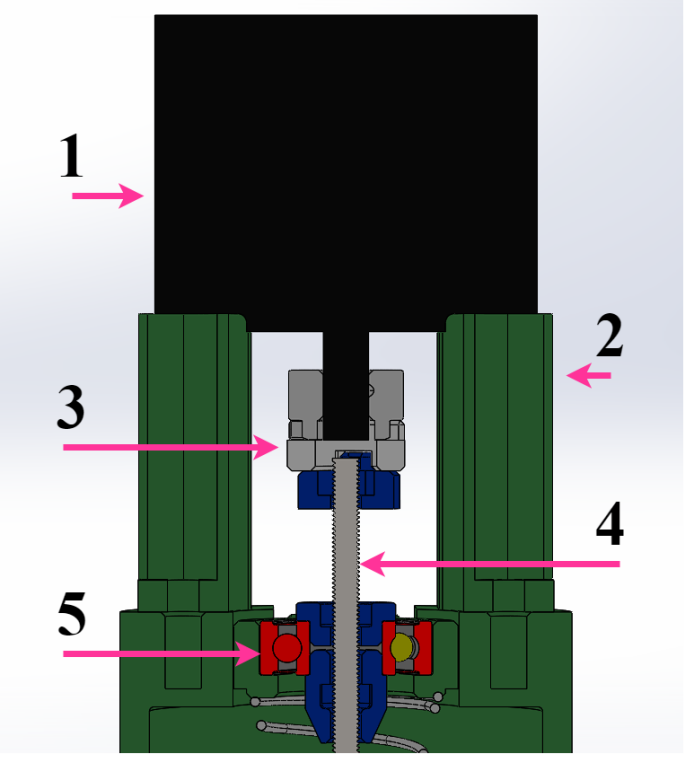

Figure 5-3 Upper portion of the prototype[5].

[4] Larger size pictures can be found in the Appendix at the end of this document.
[5] Green colour illustrates stationary frame components. Blue colour illustrates components rotating with input rotational velocity.

The clutch selected for the mechanism is a disk friction clutch. The torque is adjusted by changing the compression force applied to the sliding surfaces. The clutch is designed to be set and then used in a particular configuration which is not appropriate for this design. The adjuster cap has been removed and the number of friction surfaces has been lowered to one, as the torque required to be transmitted is very low. The compression springs that come with the clutch are not used either.

The clutch mechanism is designed to increase the pressure on the friction surfaces as the input of the clutch rotates. This is facilitated by using a spring (6) between the friction plate of the clutch and a compression plate of the mechanism (7). The compression plate assembly contains a plate with an embedded M3 nut threaded on the M3 threaded shaft and a thrust bearing on the opposite side to the spring. Rotation of the shaft therefore moves the compression plate along the axis of the shaft with the direction determined by the direction of rotation of the shaft. This movement compresses the spring which consequently increases the pressure on the friction surfaces (8). The rest of the assembly allows the spring to rotate with the input of the clutch.

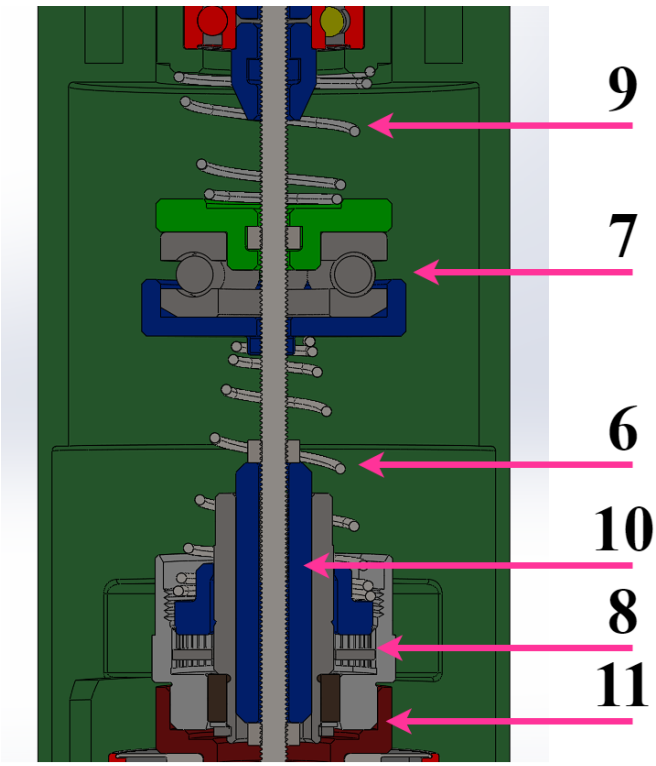

Figure 5-4 Middle portion of the prototype[6].

There is a second spring on the other side of the compression plate – the balancing spring (9). This spring is compressed even under maximum compression of the compression spring and provides a balancing force, lowering the friction on the threads and therefore reducing the necessary driving torque. Second, the friction caused by the force from the spring prevents the compression plate from rotating, which enables controlled compression. The M3 threaded shaft is connected to the input of the clutch using a centring pin (10).

The output of the clutch is connected through a connector (11) to a vane (12). The M3 threaded shaft extends all the way to the connector where it is centred using two embedded bearings (13). Specifically a Vane 2 design used in the first prototype was used in this prototype as this is the vane that requires the lowest material height for measurement while being able to fit through a 50 mm opening. The vane is submerged

[6] Green colour illustrates stationary frame components, blue components rotating with input rotational velocity, red components rotating with output rotational velocity

in the sample and an outer cup (14) is used in the same way as with the first prototype. The vane rotates in the sample based on the torque supplied to it by the clutch.

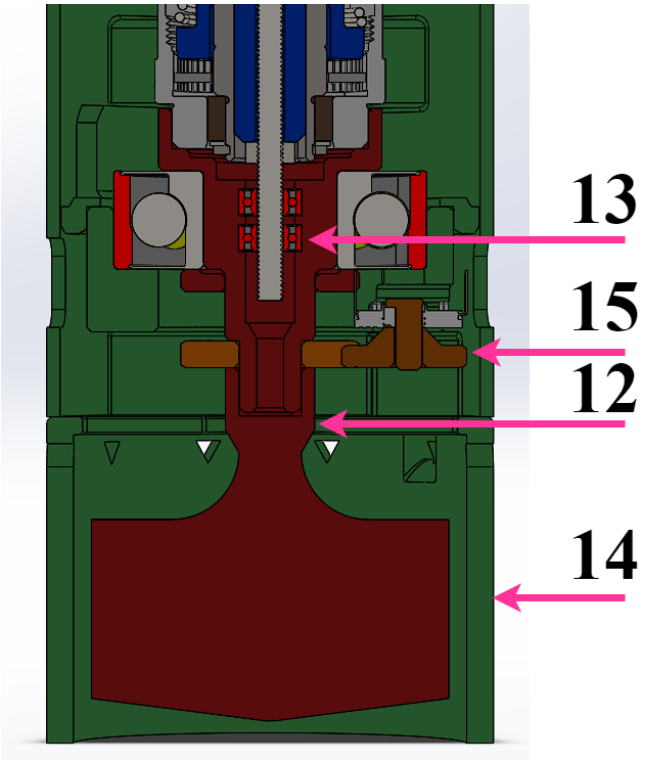

Figure 5-5 Lower portion of the prototype[7].

The angular position of the vane is measured using a potentiometer, specifically a Bourns® 3382H-1-103 potentiometer. Lack of space has been the major limiting factor in choosing a potentiometer and the same applies to the way it has been applied to the mechanism. Directly mounting a shaft through the potentiometer was not found to be a suitable solution. The shaft opening in the potentiometer is too small to accommodate a torque transmitting component. Furthermore, the tolerances of the potentiometer cause alignment issues that are not easily rectified. A geared mechanism (15) offsetting the potentiometer to the side has been chosen to facilitate the measurement, alleviating these constraints. The gear ratio options are threefold. Lowering the angular velocity of the potentiometer relative to the vane velocity is not

[7] Green colour illustrates stationary frame components, blue components rotating with input rotational velocity, red components rotating with output rotational velocity and orange components rotating with a geared output rotational velocity.

beneficial. Maintaining equal angular velocity of the vane and the potentiometer is possible and simplifies the calculations when processing the data. Increasing the angular velocity of the potentiometer increases the resolution of the measurement, at the cost of more complicated calculations when processing the data. The gear ratio selected is 18:12, where the output is the potentiometer. Radiation testing of the potentiometer is described in section 6.8.2.

The construction of the mechanism offers a limited amount of compression before the compression plate comes into contact with the clutch. The compression range is 10 mm, from the compression spring being at no load to the maximum compression on the clutch. With an M3·0.5 mm thread on the threaded rod that corresponds to 20 full revolutions of the stepper motor output from no load on the clutch to maximum load.

5.1.1 Measurement Procedure

Two procedures are programmed into the microcontroller controlling the stepper motor. One is a pre-tensioning procedure and the second is the measurement procedure. They both run the stepper motor at a constant angular velocity in opposite directions. Assumption is made that the mechanism is fully pre-tensioned before running the measurement procedure. The measurement procedure runs the stepper motor at a defined angular velocity for 20 complete revolutions. The microcontroller monitors the number of completed steps and the pre-tensioning procedure runs the mechanism for the same amount of steps in the opposite direction to pre-tension the mechanism.

One of the signal pins on the microcontroller is connected to a National Instruments DAQ card and is used as a trigger for the card to start collecting data. The

potentiometer is connected to the 5 V output pin of the DAQ card and the voltage on the slider is read with a frequency of 1000 Hz.

The potentiometer has a limited angular range where it outputs usable data – in a certain range, due to mechanical limitations it does not output correct voltage. This range is sometimes known as deadzone. The manufacturer datasheet suggests the measurement angle is 330°, implying a 30° deadzone. A small testing device has been 3D printed to try to ascertain the deadzone range more precisely. The testing setup is pictured in Figure 5-6. The outer ring has indicators spaced at 1° intervals and the needle can be attached to the hollow shaft of the potentiometer. The needle has been rotated in the deadzone until the voltage output of the wiper reached 0.01 V with a standard deviation of 1 mV in five repetitions. The angle at this point has been recorded. The needle has then been moved until the highest voltage has been reached. In this case, the voltage reached was 4.871 V with a standard deviation of 1 mV in five repetitions. In these five repetitions, the average angle at output voltage of 0.01 V was 14.4±0.5°, the average angle at the maximum output voltage was measured to be 346° in every repetition. This indicates a deadzone of 28.4°. This data was used to calibrate the potentiometer and during data processing.

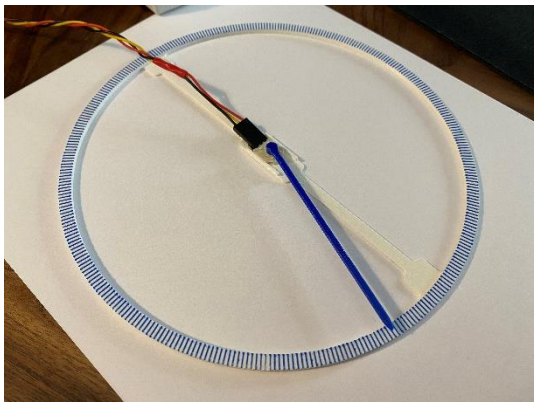

Figure 5-6 Testing of the potentiometer to determine the deadzone of the measurement.

The raw data collected with the DAQ on a rotating vane is a series of ramps from 0 to 331.6° with pauses of noisy data between them when the potentiometer is in the

deadzone, as illustrated in Figure 5-7. In order to determine the rotational velocity and enable comparison between measurement repetitions, the data had to be recalculated to cumulative angle. In order to do this, the pauses between ramps have been replaced with an increment equal to the deadzone size of 28.4°. The final form of the data can be seen in Figure 5-8.

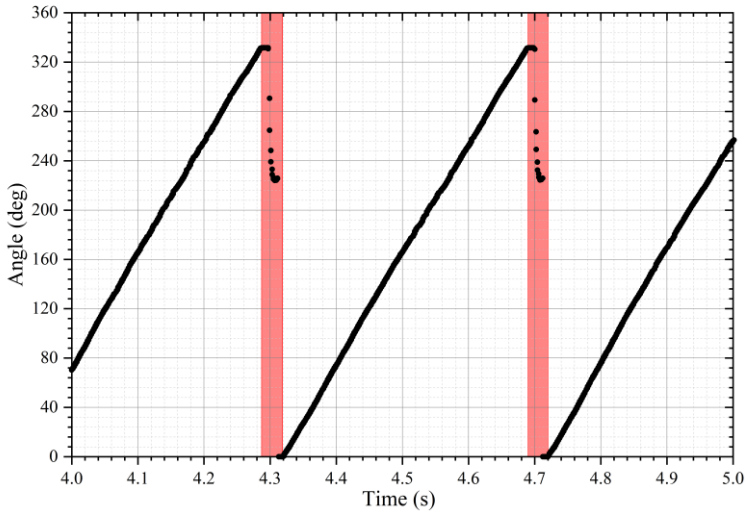

Figure 5-7 Example of raw data obtained with the prototype.

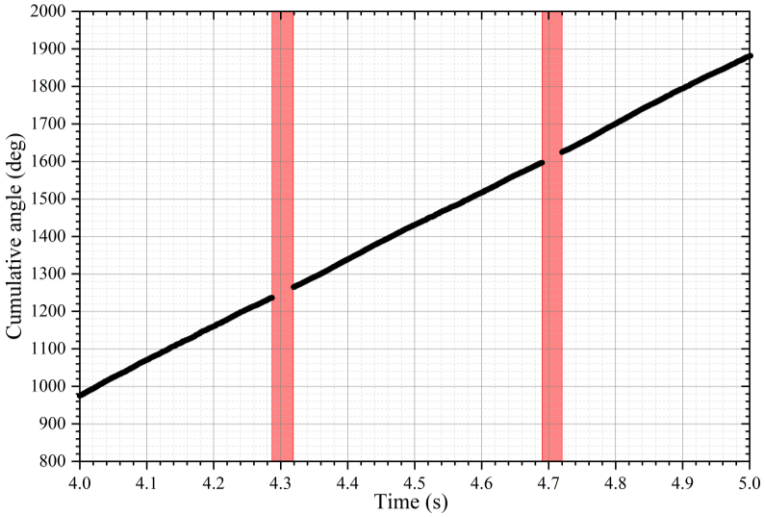

Figure 5-8 Example of processed data after removal of deadzone and conversion to cumulative angle.

5.2 Benchtop Rheometer Modification

The benchtop rheometer used in the previous calibration was no longer available and therefore a different unit has been used. The benchtop rheometer that was used in this

chapter is Lamy RM200 Plus with the Lamy EVA DIN temperature control unit. The design of this rheometer allowed for making and using custom geometries using a 3D printer. A vane, cup and a centring guard have been 3D printed with sizes equal to the geometry used on the second prototype. The guard serves two purposes – a safety aspect, preventing spillage of material at high rotational velocity of the vane and also to centre the rheometer unit with the temperature control unit. All of these components have been manufactured using PLA for most experiments and XSTRAND^{TM} GF30-PP for the ZM experiments. Their design is shown in Figure 5-9.

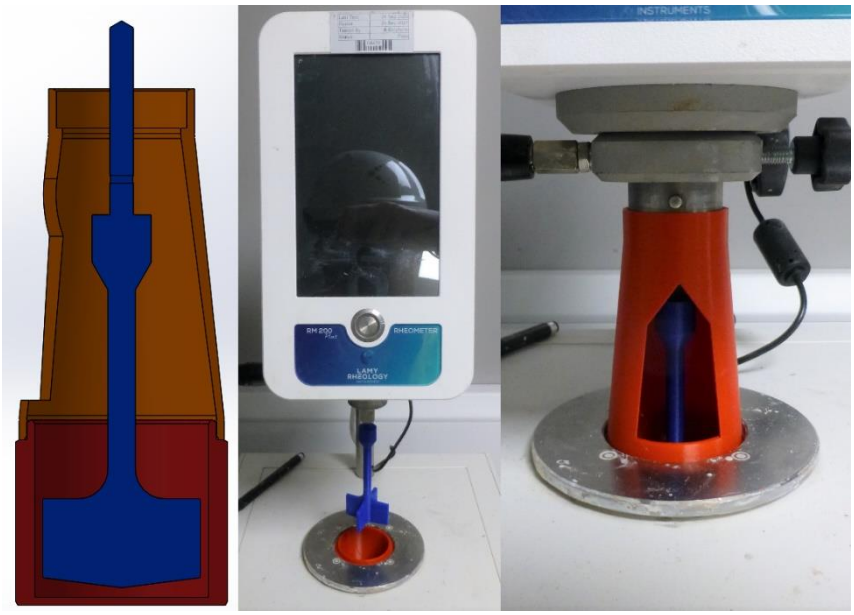

Figure 5-9 Custom geometry assembly made for the Lamy RM200 rheometer. Left: 3D model of the cup (red), vane (blue) and centring guard (orange).

The measurement using this geometry setup has been programmed so that the output data is output in rpm for rotational velocity and in N·mm for the torque. The first experiment performed with the geometry was using de-ionised water. Five repetitions have been performed at a temperature controlled by the temperature control unit at 21 °C. The procedure was set as a shear rate ramp from 0.1 to 150 rpm over a time period of 24 s (this is equal to the slowest measurement time with the prototype as further discussed in the following section).

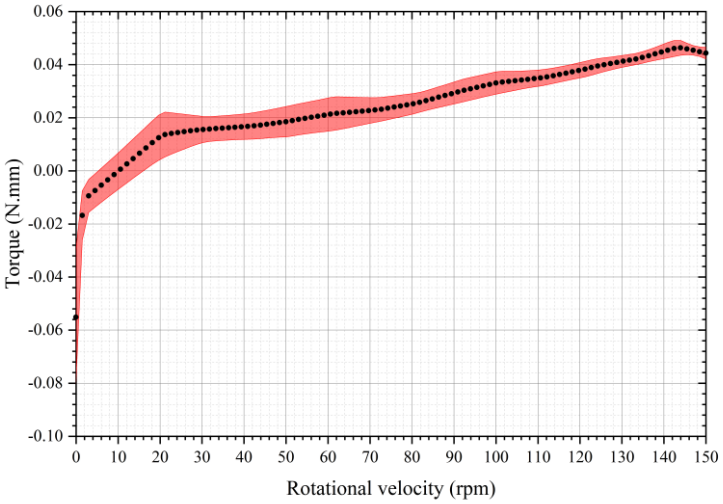

Figure 5-10 Shear behaviour of water measured with the Lamy rheometer using custom geometry.

The rheometer struggled to output consistent data at very low rotational velocities, as evidenced by the negative values at rotational velocities below 10 rpm. The change in slope at 20 rpm suggests the measurement is below the usable torque range of the instrument at torques of less than 0.015 N·mm.

5.3 Data Collected Without a Sample and with Water

The first test was performed without a sample loaded in the test cup of the prototype. Three different input angular velocities have been used - 50, 100 and 150 rpm. These velocities also dictate the measurement time that is 8, 12 and 24 s. Five repetitions of each setting have been run and the averaged data is presented below.

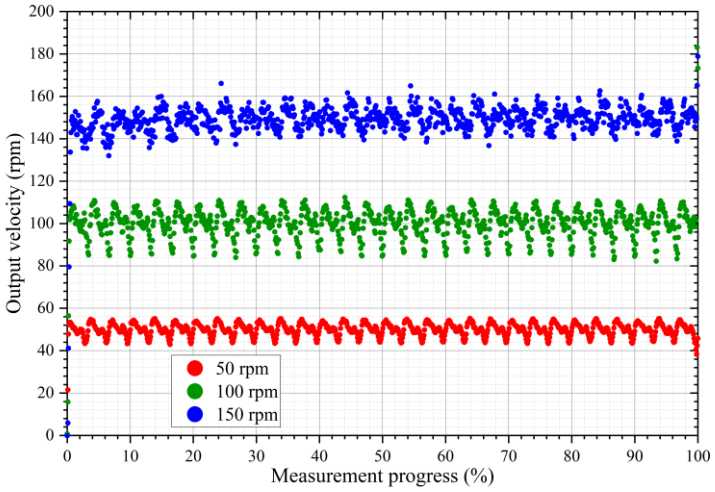

Figure 5-11 Output velocity as a function of measurement progress at three different input rotational velocities without a sample loaded in the prototype.

The measurement time at each setting is different, as discussed in the previous section and in order to compare datasets from different settings, measurement progress has been used as the X-axis. Measurement progress M_p is calculated from the time of the measurement as:

$$M_p = \frac{t}{t_{end}} \cdot 100 \tag{5.3-1}$$

where t is the time and t_{end} is the time when the measurement was finished. This allows direct comparison of output as a function of the spring compression.

The output velocity reaches the programmed input velocity practically immediately. In all datasets, there is a small delay before movement is detected (approximately 100 ms). This can be attributed to the processing delay of the microcontroller - the action to send a trigger signal to start data acquisition is performed before the action starting the movement of the stepper motor. There is also not an observable gradual increase in output velocity that would suggest acceleration of mass due to inertia. The output velocity change is almost immediate, suggesting negligible effect of the inertia of the output rotational components of the mechanism.

The second test was performed using water as the sample that was loaded into the test cup of the prototype. The water was allowed to reach ambient temperature for all measurements. Three different input angular velocities have been used - 50, 100 and 150 rpm.

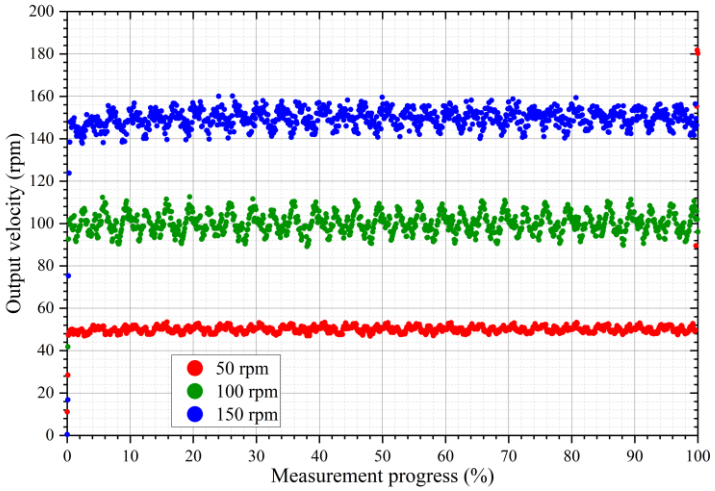

Figure 5-12 Output velocity as a function of measurement progress at three different input rotational velocities with water loaded as the sample.

The comparison of data can be done using the averaged speed and the standard deviation across the entire measurement range. This data is shown in Table 5-1.

Table 5-1 Comparison of the mean output rotational velocity of the prototype at different input velocities.

	Mean output velocity ± standard deviation (rpm)		
Input velocity	**50 rpm**	**100 rpm**	**150 rpm**
No sample	50.0 ± 3.5	100.0 ± 8.6	148.9 ± 9.3
Water	50 ± 1.9	100.1 ± 6.0	149.2 ± 7.9

The oscillation observed in the data can be attributed to the imperfections and misalignments within the mechanism, especially in the gearing to the potentiometer. The potentiometer itself is of imperfect build quality, as seen in the axial and radial play of the output shaft. Without a sample loaded in the mechanism the vibrations also

likely increase the observed noise, as seen in the lower standard deviation. This is likely due to the sample damping the vibrations.

5.4 Simulation of the Mechanism

5.4.1 Simulation Overview

A simulation of the mechanism has been created in Matlab Simulink in order to investigate the behaviour of the mechanism when running using a calibration silicone oil. Silicone oils of two different viscosities have been used in the simulation, the same materials used in the calibration of the first prototype. A simplified illustration of the simulation is depicted in Figure 5-13. The drive is simulated using a constant angular velocity source supplying either 50, 100 or 150 rpm to both the input part of the clutch and the clutch pressure adjustment mechanism. The clutch pressure adjustment is simulated using a leadscrew and a translational spring. There is a non-zero pressure exerted on the clutch without the spring being compressed, simulating the gravitational forces from the components compressing the clutch plates. The clutch is defined by the geometry of the friction surfaces, their number and the static and dynamic friction coefficients. The output of the clutch is rotating a variable damper defined by the combined resistances in the mechanism. These include bearing losses in both bearings, torque from the potentiometer, the viscous resistance of the sample when rotating the vane in it. Lastly, inertias of both the rotating parts of the mechanism and the sample are included in the simulation.

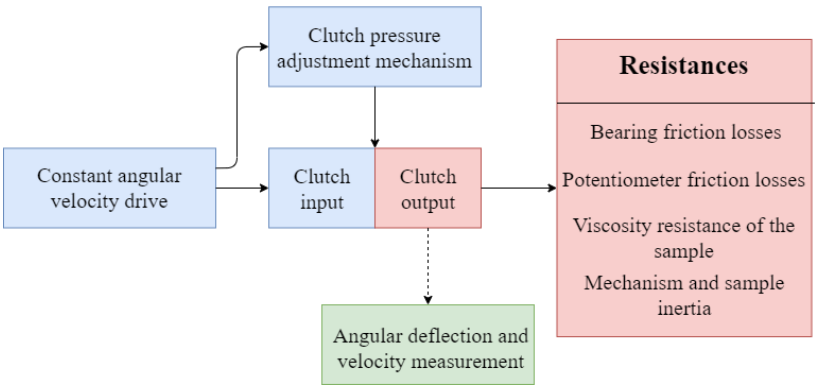

Figure 5-13 Simplified diagram of the simulation of the second prototype.

The bearing friction losses are calculated using the SKF model (all equations 5.4-1 to 5.4-9 are from this model) [120]. This model calculates the frictional moment M in a bearing as a sum of components:

$$M = M_{rr} + M_{sl} + M_{seal} + M_{drag} \quad (5.4\text{-}1)$$

where M_{rr} is the rolling frictional moment (N·mm), M_{sl} is the sliding frictional moment (N·mm), M_{seal} is the frictional moment of seals (N·mm) and M_{drag} is the frictional moment of other losses (N·mm). M_{seal} is not necessary to be calculated as neither bearing has seals. M_{drag} calculates the drag losses caused by the bearing being immersed in oil baths or oil jets. Neither option is used in the mechanism and therefore this frictional moment may be disregarded as well.

M_{rr} can be calculated as a function of the inlet shear heating reduction factor ϕ_{ish} (dimensionless), kinematic replenishment/starvation reduction factor ϕ_{rs} (dimensionless), a variable G_{rr}, the rotational speed of the bearing inner race n (rpm·min^{-1}) and the kinematic viscosity of the lubricant in the bearing ν (mm^2·s^{-1}) . The inlet shear heating reduction factor quantifies the friction losses caused by the balls of the bearing repelling a certain amount of oil into reverse flow. Both bearings rotate at very low speeds and are not flooded with oil, therefore the effect of this phenomenon is negligible. The kinematic replenishment/starvation reduction factor

describes the lack of lubrication due to the lubricant being displaced from the raceway and not being able to return there in time. This reduces the quality of the lubrication film. This is only applicable to high lubrication viscosity or high speed applications and can therefore be neglected for this simulation. The rolling frictional moment can therefore be calculated as:

$$M_{rr} = G_{rr}(\nu n)^{0.6} \tag{5.4-2}$$

where the rolling friction variable G_{rr} can be calculated as:

$$G_{rr} = R_1 {d_m}^{1.97}(F_r + F_g + R_2 F_a)^{0.54} \tag{5.4-3}$$

for the angular contact bearing, where R_1 and R_2 are geometry constants, d_m is the bearing mean diameter (mm), F_r is the radial load (reported in N, it is zero in the case of both bearings), F_a is the axial load (N) and F_g (N) can be calculated as:

$$F_g = R_3 {d_m}^4 n^2 \tag{5.4-4}$$

where R_3 is a geometry constant. The calculation of G_{rr} is different for the thrust bearing and is calculated as follows:

$$G_{rr} = R_1 {d_m}^{1.83} {F_a}^{0.54} \tag{5.4-5}$$

M_{sl} can be calculated as follows:

$$M_{sl} = G_{sl}\mu_{sl} \tag{5.4-6}$$

where G_{sl} is a variable calculated based on several parameters and μ_{sl} is a sliding friction coefficient. μ_{sl} can be calculated as:

$$\mu_{sl} = \phi_{bl}\mu_{bl} + (1 - \phi_{bl})\mu_{EHL} \tag{5.4-7}$$

where ϕ_{bl} is the weighting factor for the sliding friction coefficient, μ_{bl} is a constant depending on movement and μ_{EHL} is the sliding friction coefficient in full-film

conditions. It is noted in the SKF model that if the bearing speed is low, the value of ϕ_{bl} is approaching one. As this is the case, the equation reduces to the sliding friction coefficient μ_{sl} being equal to the constant μ_{bl}. The variable G_{sl} of the angular contact bearing can be calculated as:

$$G_{sl} = S_1 {d_m}^{0.26} [(F_r + F_g)^{\frac{4}{3}} + S_2 {F_a}^{\frac{4}{3}}] \tag{5.4-8}$$

where S_1 and S_2 are geometric constants. F_g is calculated using the same equation as equation (5.4-4), where the constant R_3 is replaced with a constant S_3. G_{sl} of the thrust ball bearing can be calculated as:

$$G_{sl} = S_1 {d_m}^{0.05} {F_a}^{\frac{4}{3}} \tag{5.4-9}$$

The thrust ball bearing rotates with the rotational velocity of the input, and the axial force is slightly lower as it is not compressed by any components due to the gravitational forces. The angular contact bearing rotates with the rotational velocity of the output and the axial force slightly higher, as it is compressed by several components due to the gravitational forces.

While these calculations are designed for constant loads and speeds, the relatively narrow operating envelope of speeds and loads in the mechanism mean this model is still a very robust method of estimating friction losses.

The friction losses from the potentiometer are more difficult to estimate. The manufacturer only provides a maximum torque value but does not clarify under what conditions this torque is reached or sustained. An assumption has been made that the torque increases linearly with rotational velocity and reaches the maximum value provided in the datasheet at 150 rpm.

The inertia of the rotational components bound the output of the clutch has been calculated using the CAD model of the mechanism based on the material characteristics used to manufacture the components. As discussed in chapter 3.5.1 and depicted in Figure 3-8, the sample contained between the blades of the vane is assumed to rotate with the vane and therefore its inertia needs to be added to the inertia of the mechanism. This is also calculated using the CAD model of the mechanism.

Another assumption is made about the model of the clutch itself. The simulation uses a Disk Friction Clutch node that is defined by the friction surface geometry, friction parameters and viscous drag. No viscous drag is used as it is not applicable in this instance. The geometry of the friction surfaces is known and represented in the simulation. The friction coefficients however are not known and an assumption has been made based on the material used. The static friction coefficient has been selected to be 0.5 and the kinetic friction coefficient has been selected to be 0.3. No assumptions can be made about whether these coefficients are constant or dependent on slipping speed. They were selected based on data indicated in [121] on interactions between brass and steel/cast iron.

The viscosity resistance contribution from the sample is calculated based on data obtained with a benchtop rheometer, with a 1 Pa·s calibration oil. The shear stress measured with a DIN standard V25 vane at a shear rate of 100 s^{-1} has been taken as the calibration value. These values are converted to torque and rotational velocity using the calibration constants used in the measurement. Using these, the damping coefficient can be calculated in the form the simulation requires. The damping coefficient for a 10 Pa·s oil is calculated by multiplying the 1 Pa·s oil damping coefficient by 10. Lastly, the difference in geometry has to be addressed in order to

apply the coefficient appropriately. As discussed in previous sections, the vane design has been based on maintaining the same shear rate as a function of rotational velocity as on the DIN standard vane, therefore no rotational velocity correction is necessary. Torque will however differ based on the geometry of the vane, as described in equation (3.5-1). A conversion coefficient has been calculated to account for the torque change and applied to both 1 Pa·s and 10 Pa·s damping coefficients.

5.5 Silicone Oil Measurement and Simulation Results

All runs with the prototype have been repeated five times. The cumulative angle data obtained this way has been averaged over 1000 datapoints. Derivation of the angular data is then used in the following graphs to illustrate the rotational velocity on the output of the mechanism. An example of this dataset is shown in Figure 5-14.

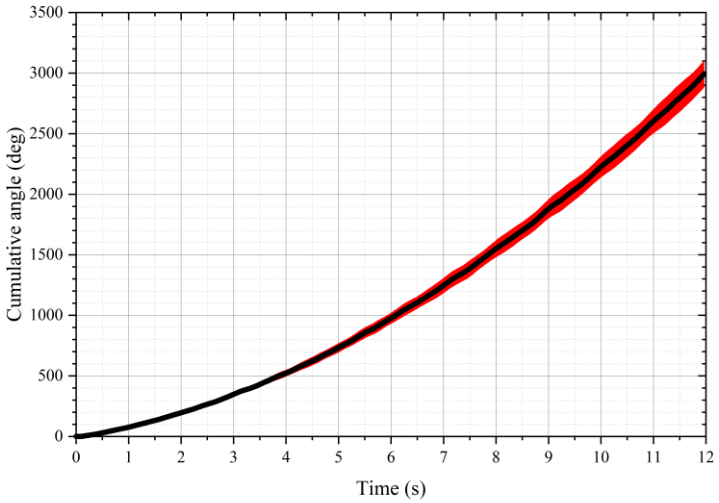

Figure 5-14 Average cumulative angle of the vane over five runs in 10 Pa·s calibration oil at 100 rpm input rotational velocity. Standard deviation of the data in red.

5.5.1 1 Pa·s Calibration Oil

A comparison of the data obtained with a 1 Pa·s calibration oil is displayed in Figure 5-15. The simulation results differ only due to the output velocity equalising with the input velocity. The simulation can roughly determine when this will occur, however the actual measurement progress up to that point is not accurately represented. The

data obtained using the prototype device suggests the torque (including the breakaway torque on the clutch) depends on the input rotational velocity.

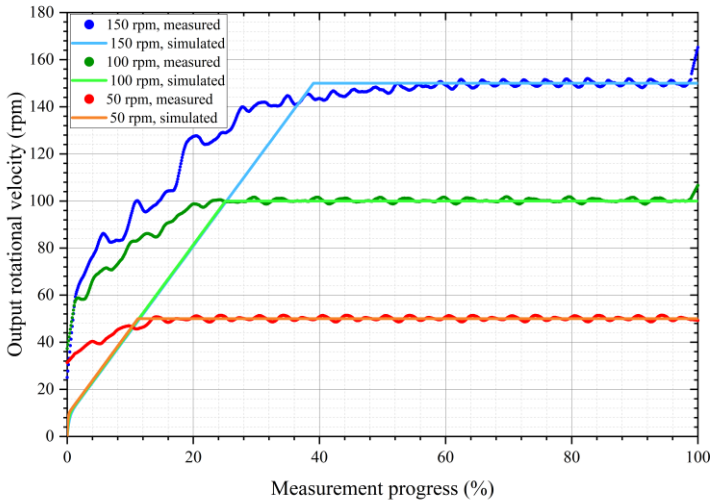

Figure 5-15 Output rotational velocity of the prototype at different input rotational velocities compared with the simulation results using the 1 Pa·s oil.

The difference in starting output rotational velocity (the apparent intercept with the Y axis) can be attributed to the breakaway torque of the clutch being higher than expected due to misalignment in the mechanism. This appears to be exacerbated by the high rotational input velocities. The non-linearity of the output can be attributed to two factors - the thermal effects caused by the uninterrupted slip of the clutch and the variation in slip velocity within the clutch. Both of these phenomena are not easily simulated without complex datasets on the materials used and is beyond the scope of this work.

The same calibration oil was measured using the modified Lamy rheometer. The results are shown in Figure 5-16 and they suggest repeatable, linear response of the material and do not indicate the onset of secondary flows across the measurement range.

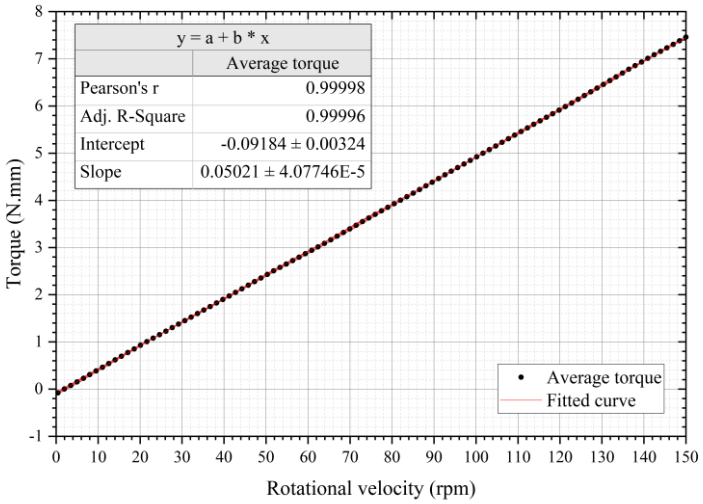

Figure 5-16 Shear behaviour of the 1 Pa·s calibration oil measured using the Lamy rheometer.

5.5.2 10 Pa·s Calibration Oil

A comparison of the data obtained with a 10 Pa·s calibration oil is displayed in Figure 5-17. In neither of the input rotational velocities does the output velocity equalise with the input velocity. Due to this, the simulation results are almost identical in all three cases as the only parameter dependent on the input rotational velocity is the thrust bearing frictional losses which are very low compared to other losses in the system[8]. The output velocities not equalising helps illustrate the torque capacity of the system and would be a valuable calibration tool when developing the prototype for more specific deployment scenarios and expected viscosities.

All three datasets obtained with the prototype are slightly different. The results suggest that the output torque is lower when using lower input rotational velocities. The deviation from the simulation and the difference between the input rotational velocities can again be attributed to the same factors discussed in the previous section.

[8] The maximum output rotational velocity at 150 rpm input rotational velocity is only 0.2% lower than at 50 rpm input rotational velocity.

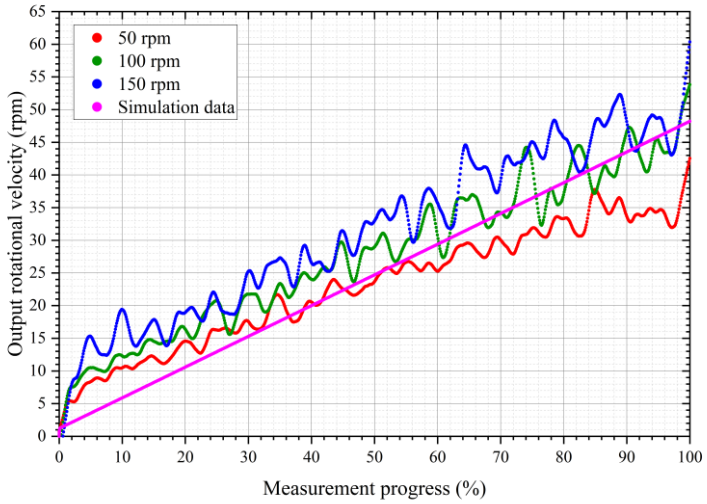

Figure 5-17 Output rotational velocity of the prototype at different input rotational velocities compared with the simulation results using the 10 Pa·s oil.

The same calibration oil was measured using the Lamy rheometer. The results are shown in Figure 5-18 and similarly to the 1 Pa·s oil there is no suggestion of an onset of secondary flows. The output velocity range is limited due to the torque capacity of the Lamy rheometer.

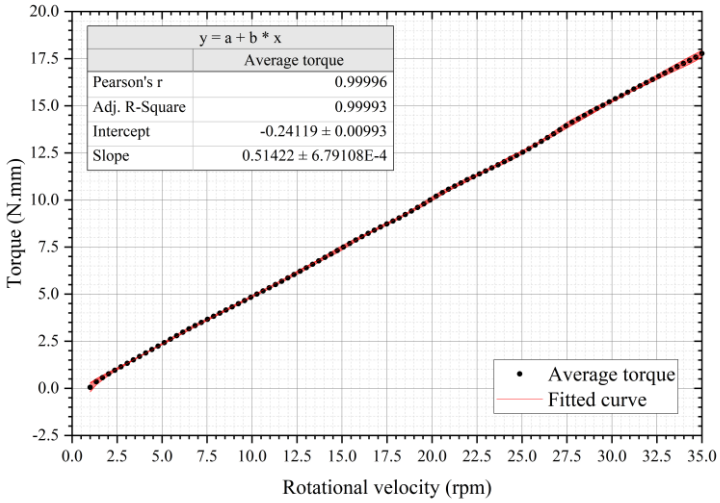

Figure 5-18 Shear behaviour of the 10 Pa·s calibration oil measured using the Lamy rheometer.

Using the fit parameters of both oils obtained with the Lamy rheometer the torque output of the device can be calculated for all measurements and the results obtained with both oils can be directly compared.

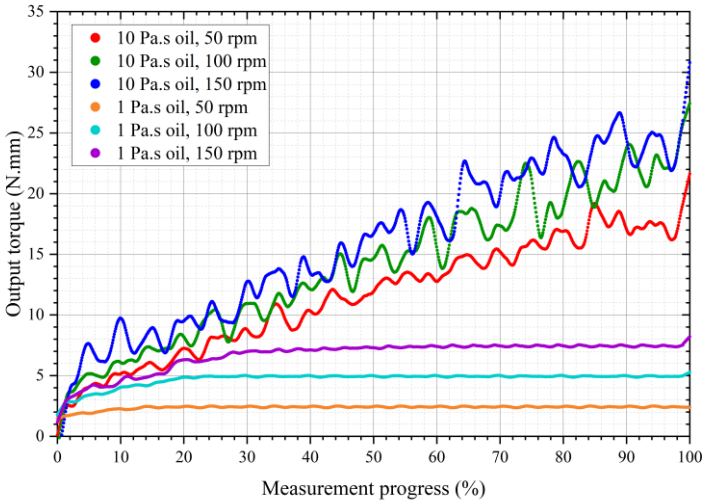

Figure 5-19 Torque output of the prototype with different calibration oils at different input velocities

The difference in the output torques can be explained mainly by the misalignment in the mechanism. Just as the variation of torque, the imperfect construction causes variation in pressure exerted on the clutch plates. Combined with the effects of different slip velocities and times of measurement causing thermal effects within the clutch the output torque will depend on the tested substance and rotational input velocity.

5.6 TiO_2 Suspension Measurements

A titanium dioxide suspension of ϕ=40[9] was prepared with de-ionised water and tested using the Lamy rheometer at 21 °C. Similarly to the results obtained with water, the rheometer struggles with the lowest rotational velocity settings, possibly due to the torque being too low and there is also a slope change at approximately 20 rpm. However, the measurements are repeatable and do not suggest an onset of secondary flows across the measured range. The results also suggest that the viscosity of the titanium dioxide suspension is too low to be detected by the prototype, as the highest torque required to shear the sample is less than 1 N·mm.

[9] This is the highest concentration that was possible to prepare at the time.

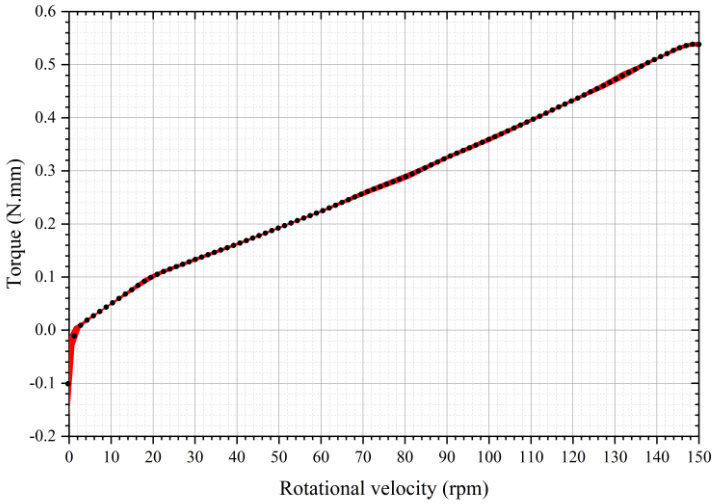

Figure 5-20 Titanium dioxide suspension shear behaviour measured using the Lamy rheometer.

The low torque required to shear TiO_2 is reflected in the data captured by the prototype as shown in Figure 5-21. At all three input rotational velocities there is a pronounced ramp leading to an equalised output and input rotational velocity. It occurs only during the first 10 % of measurement progress at 50 and 100 rpm input velocity. The ramp at 150 rpm input velocity takes longer, approximately equal amount of time as it does with water but the ramp is more pronounced. Based on these measurements, the shear properties of TiO_2 would be placed between water and the 1 Pa·s calibration oil.

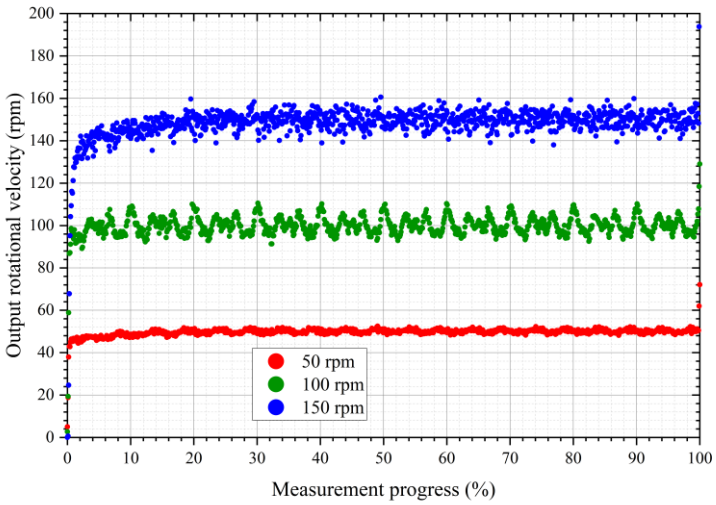

Figure 5-21 Output rotational velocity of the prototype at different input rotational velocities with a TiO_2 sample.

5.7 ZM Suspension Measurements

A ZM suspension sample was measured on the Lamy rheometer at 20 °C. Three separate measurements of five repetitions have been performed, specifically shear rate ramps from 0.1 to 150 rpm over 12, 24 and 48 s. The averaged results of the five runs are shown in Figure 5-22. It is apparent from the results that the ZM exhibits complex, history dependent behaviour. On the shortest ramp of 12 s up to approximately 40 rpm there is a distinctly linear rise in torque required to shear the sample. This is not present in the other measurements and indicates suboptimal performance of the rheometer - most likely the rise in required torque over a very short period of time is beyond the capacity of the rheometer. This issue is also present at the 24 s measurement, albeit less pronounced as it is observable only up to 20 rpm. At the slowest ramp this behaviour is still manifested until 10 rpm, although it is not as obvious as in the other measurements.

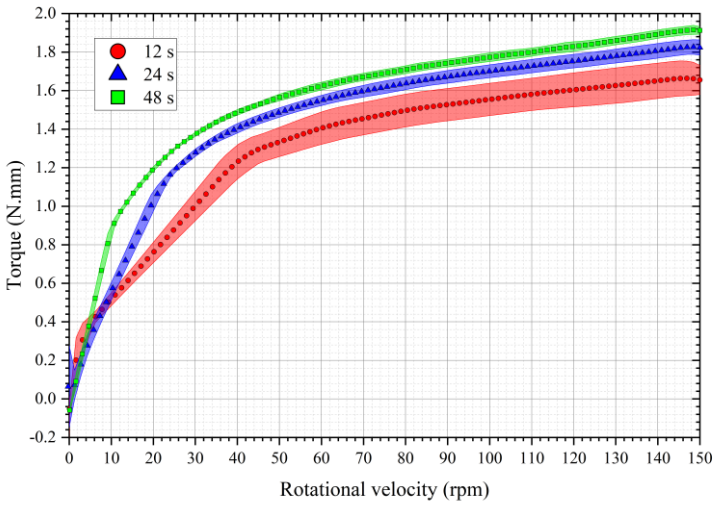

Figure 5-22 Shear rate ramp measurements performed on the Lamy rheometer with a ZM suspension.

When compared to the results obtained previously with the Bohlin rheometer as seen in Figure 4-17 it is apparent that the torque capacity of the rheometer is not sufficient a very low rotational velocities to capture the low shear rate behaviour of the suspension. Overall, the torque should be sufficient enough to be captured by the

prototype. A useful comparison can be obtained by plotting the data together with the data obtained with a 1 Pa·s oil, as seen in Figure 5-23. At low rotational velocities (approximately less than 30 rpm), the ZM suspension exhibits higher viscosity than the 1 Pa·s oil. At higher rotational velocities, it has increasingly lower viscosity than the oil.

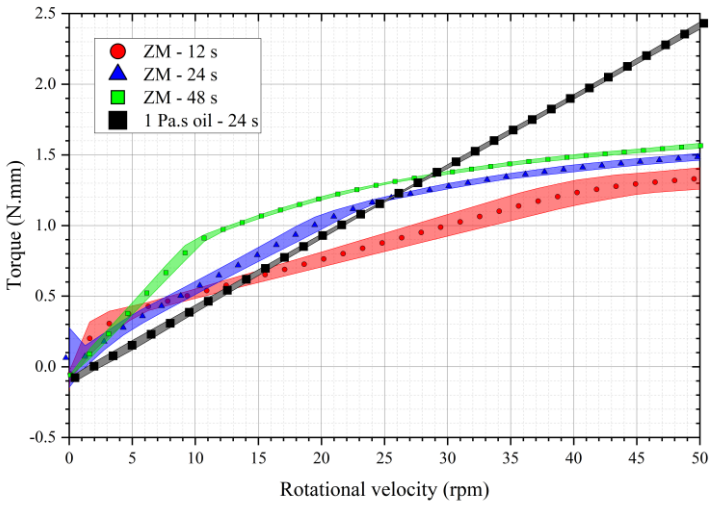

Figure 5-23 Comparison of the ZM and 1 Pa·s oil data obtained with the Lamy rheometer.

The data obtained with the prototype using the ZM sample at temperatures between 21 and 22.2 °C can be seen in Figure 5-24. At all input rotational velocities there is a low output velocity delay before the output ramps up until the velocities are equalised.

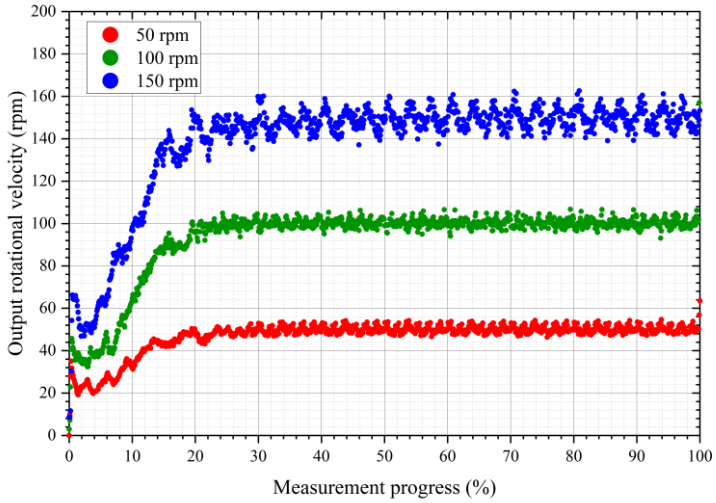

Figure 5-24 Data obtained with the prototype using the ZM sample.

In order to compare the data to the 1 Pa·s oil data both datasets have been plotted in the same graph in Figure 5-25.

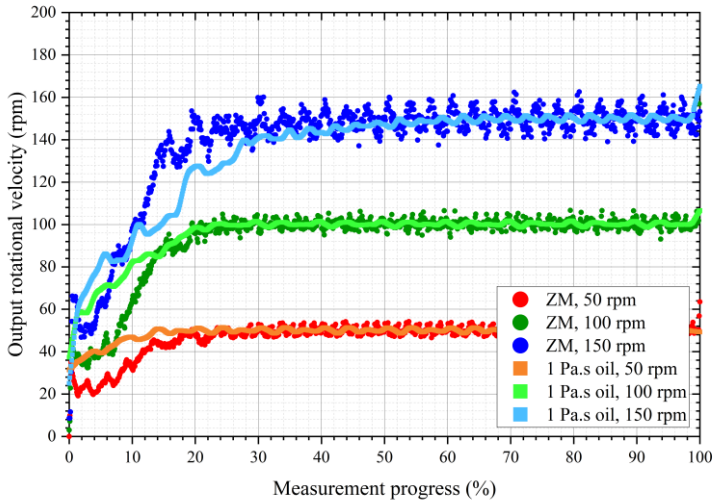

Figure 5-25 Comparison of the ZM and 1 Pa·s oil datasets obtained with the prototype.

Compared to the standard viscosity oil the expected difference can be observed. Initially, the output velocity is lower than the silicone oil. After a short time (approximately 5-8% measurement progress) the viscosity of the sample thins enough for the output velocity gradient to sharply increase. This reproduces the high viscosity to shear thinning transition of the sample as seen in the datasets obtained with the rheometer. It also illustrates the difference in movability in both substances. The silicone standard oils do not exhibit changes in viscosity and that is reflected in their datasets.

This immediate view of an initial lack of movability is highly desired when testing materials with the perspective of future clean out. These indications of yield stress and shear thinning behaviour are key for understanding how materials will react to clean out procedures. The obvious difference between a Newtonian and non-Newtonian behaviour offers valuable insight into the properties of materials and even using a comparative measurement such as this is could be very useful for further decision making in nuclear decommissioning environments.

5.8 Conclusions

The datasets generated by the second prototype provide a less absolute perspective on rheological behaviour than the first prototype, however, it has more potential to be used to generate comparative datasets. In a deployment scenario, it is assumed that the device would be calibrated against a desired substance - whether it is a test material created to simulate the tested substance or a generic reference material and the measurement would be repeated *in situ*. Comparing the two obtained datasets would then provide valuable information for future work in a normalised, repeatable way. There are two possible applications to this:

1. Comparison of data gathered in different deployment scenarios against each other but also against a normalised reference material.
2. Short or long term monitoring by repeating the measurement with quick validation by observing whether the dataset deviates from a reference measurement.

The illustration of the first approach can be seen in the comparison between the 1 Pa·s oil and the ZM suspension. Simply by comparison, both potential yield stress behaviour and shear thickening behaviour can be observed immediately. Furthermore, as the torque output is roughly linear as observed with the 10 Pa·s oil, the comparisons are scalable and could potentially be used to quickly quantify the difference in movability of the materials.

The second approach to the use of the prototype implies a more automated way to interpret the datasets. Whether for validation of rheological properties by embedding the mechanism into containers or repeated deployment of cheap, one off devices in regular intervals, a simple measurement procedure would compare the obtained data

against a pre-defined valid range of data and immediately indicate change in properties on a pass/fail basis, or indicate exactly what has changed. This could be indicating a potential yield stress appearance - as observed by delayed output velocity response or change in slope/linearity of the data, indicating change in viscosity or appearance of shear thinning or thickening behaviour. Furthermore, the effect where the input and output velocities can potentially not equalise could be used for validation too. The prototype could be specifically tailored so that the velocities equalise at a specific point and deviations from this would indicate a change in properties.

The device would require some small modifications but can be made to fit through 50 mm diameter opening, does not contain expensive or sensitive components and can be quickly manufactured. The torque capacity can be scaled by changing the friction surface size and geometry within the clutch, allowing the use in lower or higher viscosity environments.

The main development obstacle lies within eliminating the misalignments within the mechanism. These are a culmination of 3D printing, COTS components with varying tolerances and imperfections due to assembly. More generally, there are two main paths to optimise the design. One would be to design a custom clutch assembly would further reduce the size of the mechanism and optimise the friction surfaces for the desired deployment area. The second is lowering the overall length of the device which contributes to the effect of misalignment significantly. Both can be achieved with sufficient development time using rapid prototyping and COTS components and simple modifications to the simulation would aid this development.

6 Radiation Damage to Electronics and Prototyping Materials

The three main types of radiation discussed in the context of the nuclear decommissioning industry are alpha, beta and gamma radiation. Alpha and beta radiation are reasonably easily shielded, while gamma radiation penetrates many materials much easier and is therefore the most prominent type to consider when discussing radiation damage to materials in the context of nuclear decommissioning [13]. Interaction of radiation with matter and its effect on electronic components is integral to developing working solutions for nuclear decommissioning.

This chapter summarises the effect of radiation on matter and specifically electronic devices and rapid prototyping materials and describes the experiments performed to ascertain the radiation tolerance of several components used in the viscometer prototypes.

6.1 Interaction of Radiation with Matter

There exist two types of interactions between radiation and irradiated matter, physical defects and ionising effects. Physical defects are caused by direct collisions of radiation with matter. Particles are usually responsible for this effect, however in rare cases high energy photons can cause these defects too. The consequences of these interactions include Schottky and Frenkel defects and can cause changes to the physical properties of matter such as density. Photons only rarely cause displacement effects. Instead, they interact with matter in three ways [122]:

1. Photoelectric effect – most common for low energy photons (less than 100 keV). A photon collides with an electron, passing all of its energy to it and, if sufficient, this energy ejects the electron and the photon is annihilated.

2. Compton scattering – most common for medium energy photons (100 keV to 10 MeV). The photon collides with an electron with sufficient energy to eject it, however, as only a portion of its energy is absorbed by the electron the photon travels further on a different trajectory.
3. Pair production – most common for high energy photons (more than 10 MeV). The photon passes close to a nucleus, it is annihilated, producing and electron – positron pair with equal energies.

6.2 Radiation Damage to Structural Prototyping Materials

Rapid prototyping has become synonymous with 3D printing. 3D printing itself has seen a lot of growth in the applications it is used in, from bespoke structures used in the medical industry [123] to novel ways of manufacturing components in space applications [124].

The benefit of quickly manufacturing functional prototypes has made 3D printing increasingly appealing for the nuclear industry, not only for the decommissioning needs. As such, it has become important to understand the behaviour of 3D printed components during irradiation. There have been investigations into the behaviour of commonly used materials when in bulk form or processed in other manufacturing methods however direct investigations of 3D printed structures are fairly new.

The three main materials that will be considered are PLA, ABS and nylon. While there is a wide variety of 3D printing materials, these are the most widely available and used, mainly for the reasons discussed in previous chapters.

PLA appears to degrade the most. According to literature, samples of PLA become visibly distorted and discoloured, mass loss is observed and the mechanical properties, observed by measuring YM and UTS, degrade the fastest out of the compared

materials. It has been reported this happens due to chain scission in the polymer and oxidative processes due to the presence of air [125], [126]. Some sources report using ionising radiation as a way to enhance the mechanical properties of PLA. This however requires a controlled environment, especially appropriate temperature has to be maintained to balance the chain scission processes that degrade PLA with the chain crosslinking, that is reported to increase the mechanical properties of the polymer [127].

It has been mentioned that the generic description of material “nylon” does not indicate precise composition of the material and that broadly speaking, most 3D printing filaments are based on nylon PA6/66. This is reflected in the literature dealing with the radiation effects on nylon components, specific nylon polymers have been tested under varying conditions, but the literature on 3D printed components is scarce. The available data suggests that PA6/66 based 3D printing nylon is very resilient against ionising radiation. In fact, it has been observed that both UTS and YM have increased for the material over a total absorbed dose in the order of several MGy, apparently due to prominent chain crosslinking and low susceptibility to chain scission. It should also be noted that the samples became sticky at very high total absorbed doses, which could prove problematic for certain applications requiring the material be used in moving components [125].

Lastly, ABS degrades in a more complex way than PLA. Over a total dose of several MGy a consistent decrease (albeit much slower than with PLA) of UTS has been observed. YM on the other hand rises with the total dose received. The surface hardness of the samples consistently increased as well. These results indicate a more complex behaviour, in contrast with PLA and Nylon and prevents easily drawn conclusions [125], [128].

There are however more considerations to be discussed on this topic, not only in the context of nuclear decommissioning. The influence of other parameters discussed but not necessarily explored in the literature above is one of them. Due to the nature of fused deposition modelling (FDM) various modifications can be made to the way a component is printed. These changes include layer heights, infill of the internal structure, line width of the printed material. All of these parameters influence the structure on a microscopic scale, changing the porosity of the material, surface roughness and other qualities. The literature suggests that porosity and surface area of polymers exposed to oxygen influences the reactions the material undergoes during irradiation, as confirmed by the discolouration of the samples [126], [128]–[130]. It is therefore expected that not only the material, but also the settings used in printing will have an influence on the way components degrade in radioactive environments.

6.3 Radiation Damage to Conductors and Insulation

The main consideration often taken with regards to wires and cables is the activation of the metallic substances used as conductors. However, as this work is concerned mainly with gamma radiation this is not an issue. As mentioned in previous sections, displacement effects are not likely to be the issue with gamma radiation. Ionisation is more likely to happen and can potentially cause electrical currents. Nevertheless, unless very sensitive circuitry is used, this is unlikely to be an issue and these effects on conductors such as wires and cables are often considered negligible [131].

Insulation of wires and cables is however a different matter. Some substrates are known to be unsuitable for use in active environments – namely polyvinyl chloride (PVC), which is known to emit HCl while it’s being irradiated. The interaction of this acid with the insulation itself makes it brittle and eventually causes it to fall apart. Furthermore, it can react with other components and substrates around it, causing

damage. Polytetrafluorethylene (PTFE) exhibits a similar behaviour, emitting fluorocarbon gasses under irradiation that can have the same effect as the acid emitted by PVC [129], [132], [133]. This means that the selection of wiring for radioactive environments should avoid using insulation containing PVC or PTFE but for most applications, no specific considerations have to be made for the core of the wiring itself.

6.4 Radiation Damage to Passive Electronic Components

6.4.1 Resistors

Resistors are one of the three fundamental passive components used in electronic circuits, with inductors and capacitors being the other two. They obstruct current flow which generates heat that the component then dissipates. Their main characteristic considered when designing circuits and selecting them is resistance – a function of the material used for their design and the geometry of the component itself. They can be manufactured from various materials, predominantly metals, usually to conform with standardised resistance values. While they are made in a variety of geometries and packages for applications, fundamentally they are simply precision-made conductors [134].

Due to the extremely simple nature of resistors, not a lot of experimental work has been performed to test them in radioactive environments and they are considered robust and radiation resistant components [135], [136].

Potentiometers, or variable resistors are a more complex topic to discuss in the context of irradiation, as they use moving parts and a variety of materials for other parts of the components, such as casings, frames and fixings. Contact surface quality is important in the moving and stationary resistive elements, as for example a formation of

oxidised layer between the two elements may cause a change in the resistance of the potentiometer. The materials surrounding these elements are as important, as discussed in the previous section on insulation material. Due to the lack of literature, it has been proposed to perform an irradiation experiment on the potentiometers used in the designed prototypes to ascertain their suitability for *in situ* deployment.

6.4.2 Inductors

Inductors are mainly constructed as a metal coil either without a core (using air) or a ferromagnetic core. The main characteristic of inductors is self-inductance, a function of the geometry of the component and the type of core it uses. The coil used is usually no different from a conductor used elsewhere in the circuitry and therefore is not susceptible radiation damage. The ferromagnetic core used in some inductors has to be considered as well, however, literature suggests negligible effect of gamma radiation on ferromagnetic materials unless exposed to immense total doses. This leaves the secondary materials used for the packaging as the main material to consider [134], [137], [138].

6.4.3 Capacitors

Capacitors are a set of two conductors separated from each other by a dielectric material. The main characteristic of capacitors is capacitance, a function of the geometry of the conductors and the material used between them. Similarly to inductors, the conductors are not susceptible to gamma radiation. The dielectric used between them however can be. It has been reported that inorganic dielectrics like ceramic, mica and glass offer the highest radiation resistance. As expected from the issues discussed in the previous sections, organic materials, especially certain polymers are not suitable for use in radioactive environments and high expected total doses. Use of electrolytic capacitors is also not recommended. Metal-Oxide-

Semiconductor (MOS) capacitors have been reported to undergo change in the capacitance curve while being irradiated, which may be problematic for some applications [133], [134], [139], [140].

6.5 Radiation Damage to Semiconductors

Semiconductors are the foundation of all modern electronics. Ionising radiation affects all semiconductors in a variety of ways, however the effect they have on the function of the devices differs. It should be noted that several conditions affect the radiation tolerance of devices – elevated temperature will usually make semiconductors more sensitive to radiation, but at low dose rates, annealing at elevated temperatures might balance this out. Whether a device is biased or not is also an important factor.

First, one must consider the total dose the component needs to survive. Total ionising dose will affect both physical and functional characteristics of the component and will generally cause progressive change to its properties. Setting aside material degradation, total dose has two effects on semiconductors: production of hole traps and interface generation at the Si/SiO2 interface [141].

Whether by charged particles or photons, electron-hole pairs are created and in biased devices, electrons are usually swept away by the applied electric field. However, holes are less mobile and tend to migrate and produce traps in the oxide. While some recombine and some might anneal under certain circumstances, they act as positive biasing of the gate in MOS transistors affecting threshold voltage and increasing leakage current. While not immune, PMOS transistors are inherently more radiation tolerant than NMOS transistors [142].

Second, dose-rate can also prove to be of significant importance. Both low and high dose rates have varying impact on total acceptable dose a device can survive. Very

low doses (in the order of $mGy \cdot s^{-1}$) can cause severe damage to semiconductors, which is significant mainly for space applications. This is sometimes referred to as enhanced low dose rate sensitivity (ELDRS). Very high dose rates can induce high currents in the device and cause latchup or burnout (further explained below) [143].

Lastly, single event effects (SEE) are consequences of individual collisions of particles with the device, causing a variety of defects. They can be divided into two categories – soft SEEs are not destructive and can be easily fixed and hard SEEs are destructive, causing permanent damage to the device. They can be classified as follows [141]:

a. Non-destructive SEEs
    i. Single event upset (SEU)
    ii. Single event transient (SET)
b. Destructive SEEs
    i. Single event latchup (SEL)
    ii. Single event burnout (SEB)
    iii. Single event gate rupture (SEGR)
    iv. Single event snapback (SES)

SEU is caused by ionization that causes a change of state in a device. An example is a bit flip – a change between the binary values of a bit in memory devices. This can be caused by charge deposition, when a charged particle travels through the device, creating electron-hole pairs along its trajectory or charge collection, when charge carriers are collected in certain parts of semiconductor devices. Depending on the device architecture and materials, the specifics of mechanisms of SEUs vary, but as they are soft errors, a simple device reset eliminates them. Multiple-bit upsets (MBU) occur, when a single particle causes multiple errors. Single event functional interrupts

(SEFI) occur, when the particle collision causes the device to temporarily lose functionality. Even though these defects do not cause permanent damage, they can render devices useless in active environments [141], [144].

SETs are similar to SEUs as they are caused by ionization. However, they are caused by temporary voltage or current pulse created by the ionization. That might in turn create direct issues – for example in voltage comparators, or the pulse can travel through a digital system, causing an SEU or disruption of the output signal. The production and propagation of SETs is dependent on a number of factors but decreasing sizes of integrated circuit (IC) devices and increasing clock speeds help SETs travel through digital systems and cause disruptions. They do not cause permanent physical damage, but cause information disruption [145], [146].

SELs are unique to complementary metal-oxide semiconductors (CMOS). Essentially, charge deposited by radiation may create a current spike that triggers parasitic transistors in the CMOS structure. If several conditions are met (see [147] for details), a short-circuit is created and if not rectified by a power cycle, high current flow may cause excessive heat build-up and cause physical damage to the device. Some conditions, like increased operating temperature and decreased device size, make products more susceptible to latchup. There are devices inherently resistant to latchup and a variety of radiation hardening methods exist, that can effectively protect the device from SELs [148], [149].

SEBs occur in bipolar junction transistors (BJTs) and metal-oxide semiconductor field-effect transistors (MOSFETs), with thyristors and diodes being susceptible as well. As in other single events, current created usually by an ion travelling through the device structure is the cause of these events. This induced current can turn on a

parasitic NPN transistor in the device structure that can cause high voltage and current flow, consequently thermally damaging and destroying the device [150], [151].

SEGRs occur in MOSFETs. It is a destructive event, caused by a creation of a conductive path through the gate structure to the drain. For a SEGR to occur, the ion creating the electron-hole pairs in the device needs to pass through the gate oxide, through the neck and into the drain (although newer papers suggest a secondary possible mechanism and potential trajectory for SEGR to occur). This can create a transient voltage that can exceed the breakdown voltage of the gate insulator. Shorter events may not cause device failure, but most events will cause thermal damage to the vicinity of the gate [152]–[154].

SESs are similar to SELs, except they occur in n-channel transistors. As with SELs, a well-placed ion strike activates a parasitic transistor in the device leading to high current condition, that can cause permanent damage to the device unless quickly rectified [141], [155].

6.6 Radiation Damage to Microcontrollers

Radiation damage to materials and simple components is well understood in literature, as the previous sections indicate. The effect of radiation on some low-level components, such as voltage regulators has been investigated in the literature. However, even these investigations focus predominantly on the effects of radiation for space applications. Testing of microcontrollers themselves is limited in the literature. Some literature focuses on the SEE characterisation of microprocessors due to mixed radiation fields, giving only little detail about TID effects of only gamma radiation [156], [157]. Other sources focus purely on heavy ion and neutron irradiation and while they describe and quantify TID effects, due to the very different modes of

interaction between different types of radiation with electronics, it is hard to correlate the results with purely gamma irradiation experiments [158], [159].

Based on the information available, it is not possible to draw conclusions about the performance of COTS microcontrollers in the context of nuclear decommissioning. The difference in the dose rates, radiation types and testing condition are the main reasons. It was therefore proposed to test a COTS microcontroller board using gamma radiation for functionality during irradiation. COTS microcontroller boards use various components, such as voltage regulators, memory modules and current limiting switches as well as the microcontroller chip itself. The critical component ensuring the function of the microcontroller is the voltage regulator, therefore the first experiment was focused solely on the degradation of the on-board voltage regulator. The further experiments attempt to quantify the gamma radiation effects on the three main aspects of functionality of the microcontroller itself – digital output, analog output and analog input performance.

6.7 Radiation Testing Considerations

While a variety of databases - namely NASA[10], IAEA[11] and ESA[12] for example – provide a breadth of technical reports on radiation testing of electronics, great care needs to be taken when using these sources as basis for radiation tolerance assessment of a whole product for several reasons. The main considerations one has to make when selecting electronic components for radioactive environments is the existence of data, change of manufacturing process and data comparison between lots and the applicability of the data itself.

[10] https://ntrs.nasa.gov/search.jsp
[11] https://inis.iaea.org/search/default.aspx
[12] https://escies.org/

Due to large technological leaps in electronic devices development, there may be no results whatsoever for a given device. While some simple discrete components have not changed much, semiconductor technology makes great advances every year and COTS products are rarely radiation hardened or tested, as demand for radiation tolerant devices is not very high.

While product numbers may stay the same, as the overall product specification has not changed, the production process or the foundry might change, rendering previous radiation testing useless, as one can rarely predict the influence of the production process on radiation tolerance. Similarly, products can differ to some extent between individual wafer lots. Even though the process and foundry are the same, some variance between products will always exist and that is minimized by using devices from the same wafer lot.

Analysis of SEEs in electronic devices due to the presence of heavy ion and proton radiation in space and neutron radiation in nuclear applications can be useful in some applications. These tests however often don’t include total ionising dose data, relevant in gamma radiation environments. Other issues might include radiation sources of different types and energies, than those present in the expected environment of the device, few tested devices and other issues.

The main concern with gamma radiation testing is the dose rate – as discussed above, ELDRS is of great concern for space applications, but not necessarily for nuclear applications. Accelerated testing, annealing of the device between individual irradiations and whether a device is biased during testing are just some of the considerations that need to be taken into account when evaluating radiation testing data. Following specific testing procedures and standards – like MIL-STD-883/1019.9

– is important for the data to be considered comparable to other sources and for cross comparison between individual tests and components. Data on radiation doses in real deployment scenarios is not available and therefore the guidance provided by this standard is the only real reference point one can use for selecting dose rates when performing irradiation experiments. However, it is important to mention that fundamentally, constant dose rate will never be reproduced in deployment scenarios. Following this standard then serves mostly for further comparison with more literature and testing for deployment capability might require bespoke procedures.

Total dose selection for experiments is similarly complicated. As dose rate in a lot of deployment scenarios will be uncertain, so will be total dose. There are two approaches how to tackle this challenge. The first one is to irradiate a component to a dose so high it could not conceivably be surpassed in most deployment scenarios. Following the dose rate recommendations however means this might produce experiments that take an extremely long time. The second approach, only possible with some components, is to continuously test them during irradiation and continue the irradiation to the point of failure. This however creates complex experimental setups and is not always possible for some components.

6.8 Experimental Work

6.8.1 Continuous Turn Potentiometer of the Shear Rate Ramp Prototype

A continuous potentiometer (Bourns® 6630S0D-C28-A103) has been connected with a 3D printed shaft connector to a stepper motor (RS PRO 535-0372). The motor was programmed to rotate at 3 rpm by a microcontroller and a stepper motor driver in a direction that increases the voltage output of the potentiometer as it rotates.

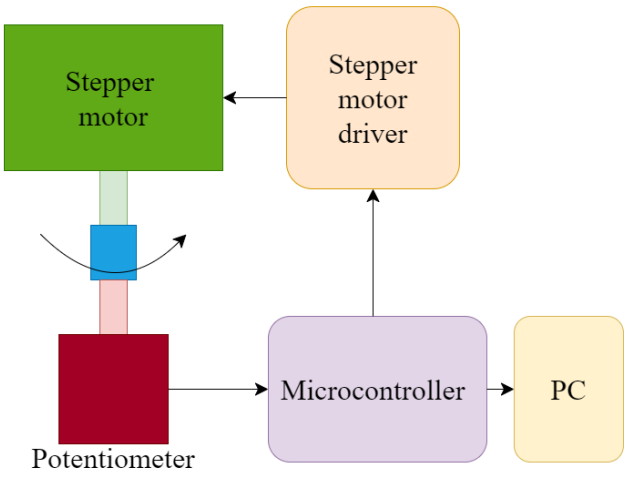

Figure 6-1 Diagram of the testing layout for the first potentiometer

The values of the potentiometer are read with a Teensy 3.6 microcontroller and transferred and saved using the Arduino IDE environment to a PC. The data is read with 16-bit precision on-board ADC, meaning the output of the potentiometer is a number between 0-65 535. These correspond to the voltage range of 0-3.3 V, as the supply voltage from the microcontroller is 3.3 V. Furthermore 0 is 0° and 65 535 is roughly 340° (the potentiometer has an effective electrical angle of 340° as stated by the manufacturer) [160]. Because of the uncertainty of the output near the zero/maximum values and in the remaining 20° of potentiometer travel, data has only been recorded and saved between the values of 2 500 and 62 500. Five potentiometers have been tested at varying dose rates. All data is average of five runs recorded before and five runs after irradiation. Potentiometers have been irradiated for 24 hours using a ^{60}Co source at the Dalton Cumbrian Facility (Foss Therapy Services Model 812 Cobalt 60, self-shielded). The dose rates and corresponding total doses can be found in the table below.

Table 6-1 Comparison of dose rates and total doses the samples have been exposed to

	Dose rate (Gy.min^{-1})	Total dose (kGy)
SAMPLE 1	47.27	68
SAMPLE 2	47.11	68
SAMPLE 3	83.04	120
SAMPLE 4	82.81	119
SAMPLE 5	200.99	289

An example of the results is illustrated in Figure 6-2. The data is plotted as a function of time as the angle of rotation is proportional to the time of the measurement due to the constant rotation velocity of the motor. It is apparent that comparing raw data obtained before and after irradiation suggests no significant difference in the output of the potentiometer. As such, a different method is used to illustrate the effect of irradiation on the potentiometers.

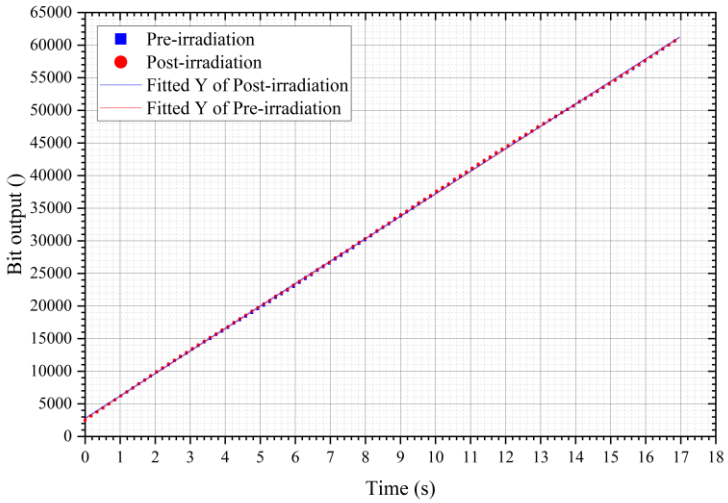

Figure 6-2 Example output values of rotating potentiometer sample number 1 as a function of time.

The data has been fitted with linear functions for both pre irradiation and post irradiation measurements. In all cases, as seen in the R^2 column in Table 6-2, the linearity of the potentiometer output remains high after irradiation. The intercept and slopes of the fits change slightly in all observed cases.

Table 6-2 Linear fit data for potentiometer measurements

		Pre-irradiation			*Post-irradiation*		
Sample	**TID (kGy)**	**Intercept**	**Slope**	**R^2**	**Intercept**	**Slope**	**R^2**
1	68	2693.6	0.00344	0.99991	2828.0	0.00345	0.99991
2	68	2499.5	0.00347	0.99984	2417.8	0.00349	0.99984
3	120	2586.6	0.00345	0.99991	2544.3	0.00345	0.99991
4	119	2610.5	0.00347	0.99980	2661.9	0.00348	0.99979
5	289	2629.6	0.00349	0.99983	2682.7	0.00346	0.99984

To visualise the effect of irradiation on the potentiometer output, the deviation from the linear fits (converted into mV from bit values) has been plotted as a function of time for all of the samples. For the post-irradiation results, deviation from both pre-irradiation fit (initial fit) and post-irradiation fit (adjusted fit) have been plotted. The adjusted fit data is a good indicator of the overall performance of the potentiometer after irradiation, independent on the performance before irradiation. The initial fit data is a good indicator of the change in performance during irradiation in applications where the output of the potentiometer needs to remain repeatable. Two examples are plotted below in Figure 6-3 and Figure 6-4, the rest can be found in the appendix.

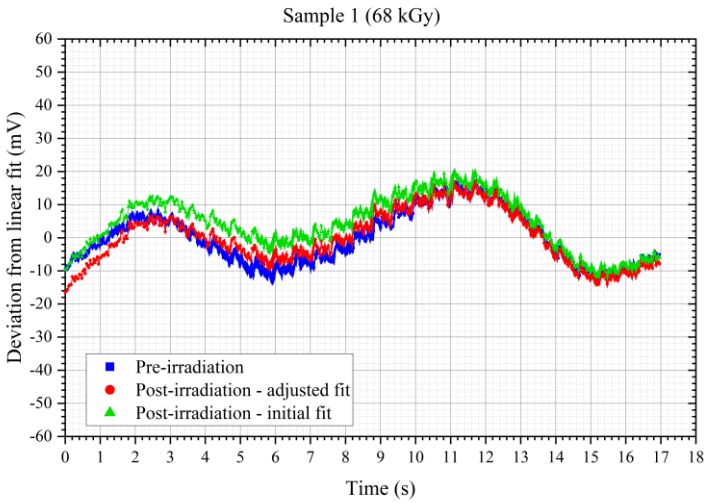

Figure 6-3 Data from sample 1.

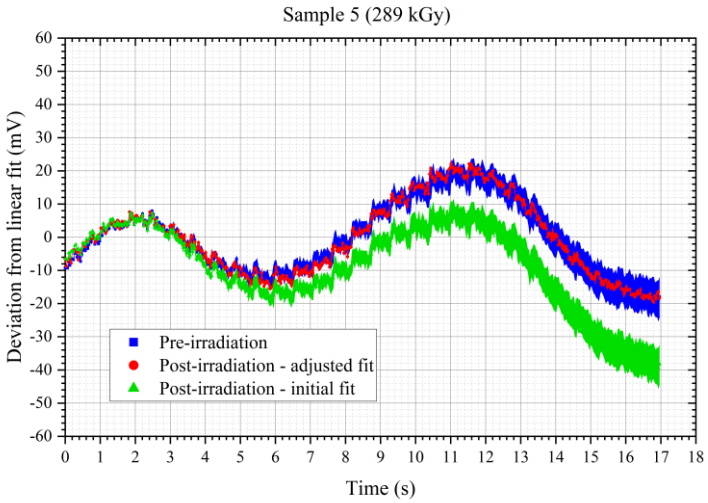

Figure 6-4 Data from sample 5.

The Y scale of Figure 6-3 reflects the independent linearity of the potentiometers as described in the datasheet. On a 3.3 V supply, the reported independent linearity of ±2% amounts to a deviation of ±66 mV [160]. None of the samples have exhibited non-linearity outside of the manufacturer's specification, even after irradiation. Samples 1 and 2 exhibit the least amount of change after irradiation. In both samples, only a certain region of the measurement range appears to be affected. Both the adjusted fit and initial fit report only small changes. Sample 3, while within manufacturers specification for linearity, output very noisy signal compared to the other samples. However, after irradiation this noise appears to have decreased, with both adjusted and initial fit. Samples 4 and 5 have virtually unchanged adjusted fit outputs after irradiation, however their initial fits have been slightly offset. With sample 4, this offset is observable across the entire measurement range, with sample 5 there is a range that is seemingly unchanged by irradiation.

This effect of irradiation only on some of the measurement regions suggests an uneven degradation of materials in the potentiometer, most likely in the resistive element itself. The effect of radiation can be observed on the surface of the metallic

components. The surface darkens and becomes more matte, this is also demonstrated on the threaded part of the potentiometer that has not been shielded by the locking nut.

Figure 6-5 Comparison of the appearance of samples of potentiometers. From left to right: Control sample, non-irradiated; sample number 3, irradiated to 120 kGy; sample number 5, irradiated to 289 kGy.

6.8.2 Continuous Potentiometer of the Shear Stress Ramp Prototype

The continuous turn potentiometer used in the second prototype was also tested at the Dalton Cumbrian Facility. The potentiometers were divided into three groups of three samples. Initial testing using the prototype was performed to establish the data quality obtained with the potentiometers. With no sample loaded, five repetitions of running the prototype were performed with each potentiometer. The input rotational velocity was 100 rpm. In order to provide a representative dataset for comparison after irradiation the average output velocity and the standard deviation of the velocity has been calculated. The average calculation excluded the first and last 100 ms of the dataset, as there is an inconsistent start time that affects the start of the measurement and a calculation error caused by the deadzone can influence the end of the measurement. Because no sample was loaded in the prototype and the only change made to the prototype is the use of a different potentiometer any changes to the calculated parameters can be attributed to the irradiation.

The groups were irradiated to different TIDs by specific placement and time spent in the irradiator chamber. The dose rates were selected in the range recommended by the MIL-STD-883K standard [161]. The first day of irradiation subjected the samples to the following doses and TIDs:

Table 6-3 First irradiation experiment summary of dose rates and TIDs.

Potentiometer number	Dose rate (Gy·s^{-1})	TID (Gy)
1	0.59	993
2	0.61	1020
3	0.61	1020
4	0.51	10 059
5	0.51	10 102
6	0.51	10 102
7	2.63	49 141
8	2.69	50 108
9	2.69	50 108

After this irradiation the samples have been used in the same test as before irradiation in order to collect data necessary to calculate average output velocity and the standard deviation of the output velocity. The body of the potentiometers was discoloured by the radiation changing the colour to dark grey as seen in Figure 6-6, the rotor of the potentiometer does not appear to be affected. No physical damage or movement restriction has been observed.

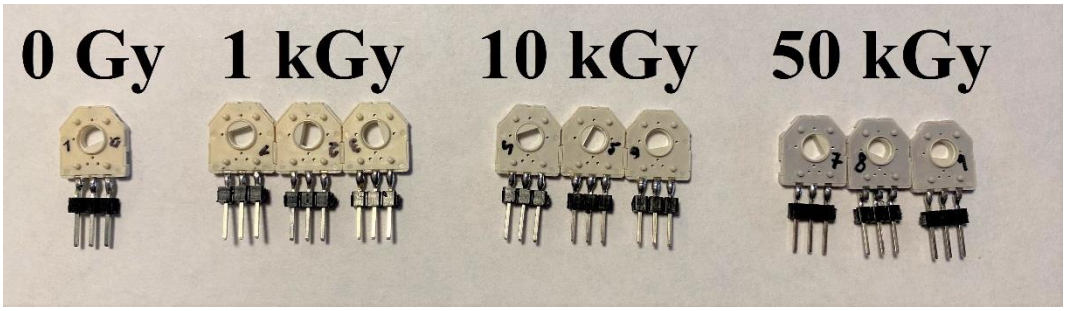

Figure 6-6 Potentiometers after first irradiation with TID illustrated above each group.

The second day of irradiation subjected the samples to the following doses and TIDs:

Table 6-4 Second irradiation experiment summary of dose rates and TIDs.

Potentiometer number	Dose rate (Gy·s^{-1})	TID (Gy)
1	2.24	50 097
2	2.32	51 813
3	2.32	51 813
4	2.63	74 616
5	2.68	75 931
6	2.68	75 931
7	2.45	98 820
8	2.50	100 775
9	2.50	100 775

After this irradiation the samples were again tested with the prototype and the average output velocity and the standard deviation of the output velocity were established. A comparison of these averages and standard deviations is depicted in Table 6-5. The discolouration of the potentiometers became normalised across all irradiated samples and is illustrated in Figure 6-7.

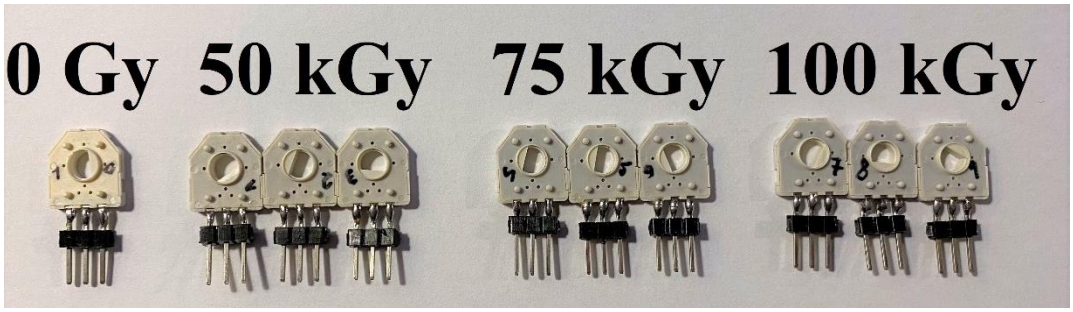

Figure 6-7 Potentiometers after second irradiation with TID illustrated above each group.

The data suggests no degradation of the functionality of the potentiometers was observed in any of the tested samples. The reported average velocity is maintained irrespective of TID and the standard deviation of the average has actually decreased with irradiation in several samples.

Table 6-5 Summary of irradiation testing results of potentiometers used in the shear stress ramp prototype.

	TID (kGy)	**Average rotational velocity (rpm)**	**TID (kGy)**	**Average rotational velocity (rpm)**	**TID (kGy)**	**Average rotational velocity (rpm)**
Sample 1	**0**	100.2 ± 4.0	**993**	100.0 ± 3.1	**50097**	100.0 ± 2.5
Sample 2	**0**	100.2 ± 5.1	**1020**	100.1 ± 4.1	**51813**	100.1 ± 3.7
Sample 3	**0**	100.1 ± 5.3	**1020**	100.2 ± 4.0	**51813**	100.2 ± 4.1
Sample 4	**0**	100.1 ± 4.8	**10059**	100.1 ± 3.2	**74616**	100.1 ± 3.6
Sample 5	**0**	100.3 ± 6.0	**10102**	100.1 ± 3.8	**75931**	100.1 ± 2.8
Sample 6	**0**	100.3 ± 3.8	**10102**	100.2 ± 4.4	**75931**	99.9 ± 2.5
Sample 7	**0**	100.2 ± 3.5	**49141**	100.3 ± 2.9	**98820**	100.0 ± 2.9
Sample 8	**0**	100.2 ± 3.1	**50108**	99.9 ± 2.5	**100775**	100.1 ± 3.5
Sample 9	**0**	100.2 ± 4.3	**50108**	100.1 ± 4.3	**100775**	100.2 ± 4.2

6.8.3 Teensy 3.6 Microcontroller

This work was done in collaboration with Antonio Di Buono from the University of Manchester as part of the CINDe consortium. The author contributed to all aspects of this work. Significant contribution was made to the design of the experimental procedure, data collection, data processing and the creation of the Arduino code of the microcontroller.

6.8.3.1 Devices Used and the Experimental Layout

The COTS microcontroller platform that has been used in the previous chapters for control and data acquisition has been selected as the platform to test. The platform is called Teensy® 3.6 and it is manufactured by PJRC. It is based around a MK66FX1M0VMD18 ARM® Cortex®-M4F microprocessor running at 3.3 V and in all the applications mentioned in this thesis it has been running at the default clock speed of 180 MHz. It offers a wide variety of useful functions and outputs, such as a wealth of communication protocols it supports including the hardware required for it, touch sensing capability and all pins being interruptible. In the work presented in this thesis the high quality 13-bit resolution ADC, 12-bit resolution DAC, on-board micro-USB port and the ability to program it using the Arduino language were the critical functionalities.

For the purpose of physically supporting the board and provide a base for connectors, four types of printed circuit boards have been designed and manufactured. Three of the types have been made for the irradiated boards and will be further referred to as primary boards. The last type has been created for circuitry to supply voltage to the primary boards and measure the supplied current in the last set of experiments, these will be referred to as secondary boards. The voltage is regulated by a Texas Instruments LM2937 voltage regulator, the current measurement components selected were Linear Technology LT®6105 current sense amplifier and a Texas Instruments OPA140 operational amplifier.

The data has been collected using National Instruments LabVIEW 2019, the first two experiments utilised a NI USB-6009 data acquisition (DAQ) USB card, the third experiment used a NI USB-6210 DAQ USB card. Two different power supplies have

been used in the experiments, Elektro-Automatik EA-PS 2342-10B and RS PRO IPS 303DD.

The Dalton Cumbrian Facility irradiator described previously has been used in all of the experiments. Before every experiment, the dose rate has been measured at the designated place where the boards have been placed using a RadCal® 10X6-0.18 high dose rate chamber. The dose rates indicated below are the average dose rates measured over 60 seconds and have been chosen in accordance with MIL-STD-883K [161].

The experimental equipment has been placed in two main locations, the irradiator chamber and the control room of the irradiator. The majority of equipment was placed in the control room so that it would not be exposed to the radiation. Figure 6-8 summarises the equipment used and its placement in all three experiments. The first experiment connectors are red, second experiment connectors are green and the last experiment connectors are blue. The shielding (20 mm tungsten, 52 mm lead), secondary board and reference microcontroller have only been used in the third experiment and they are highlighted in blue.

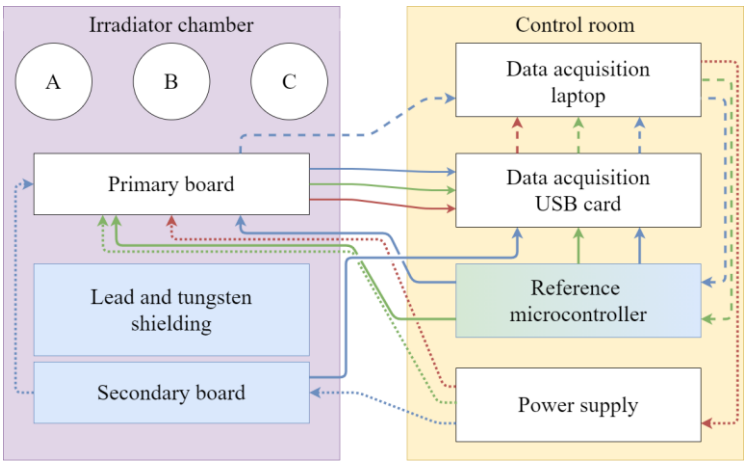

Figure 6-8 Illustration of the physical layout of all the experiments performed in a top-down view. The circles marked A, B and C represent the ^{60}Co rods of the irradiator, red colour represent first, green colour second and red colour third experiment connectors and equipment. Dotted lines represent power supply wiring, dashed lines USB cable and solid lines signal wires. [162]

6.8.3.2 Voltage Regulator Test

The first set of experiments was focused on how the voltage regulator of the platform behaves under irradiation. It has been decided to measure the output voltage of the voltage regulator on the 3.3 V output pin of the board. Six samples of the board have been used. Four of them, labelled A1, A2, A3 and A4 have been exposed to a dose rate of 1.952 $Gy.s^{-1}$. Two more samples, labelled A5 and A6 have been exposed to a dose rate of 0.997 $Gy.s^{-1}$. All of these samples will generally be referred to as A samples. All of the microcontrollers have been programmed with a simple code, periodically switching the state of the onboard LED. The power supply, placed outside of the irradiator, has been programmed to switch the voltage it outputs to the microcontroller board every five seconds. The values it switched between were 3.85, 4.00, 4.40, 4.75, 5.15 and 5.70 V. This procedure was meant to determine whether the deterioration of the voltage regulator is linked to the input voltage. A second consideration that needed to be investigated was the effect of temperature on the voltage regulator. The irradiator chamber experiences elevated temperatures as a consequence of the heat generating qualities of the active material used for irradiation. In order to rule the temperature effects out, the same procedure has been performed with samples A1-4 in a temperature controlled oven at approximately 45 °C for more than five hours before the irradiation experiments.

6.8.3.3 Functionality Tests

In order to determine whether the functionality of the microcontroller board degrades under irradiation and whether its performance could be improved with a simple modification, two sets of tests have been performed.

The second experiment, with four samples labelled B2, B3, B4 and B5 has used the microcontroller boards as they were supplied. The boards have been irradiated with a dose rate of 1.108 $Gy.s^{-1}$ and will generally be referred to as B samples.

The third experiment, with three samples labelled C2, C3 and C4 has used the boards with a slight modification – the on-board voltage regulator has been detached. The voltage to the board has been supplied by a secondary board, also located in the irradiator chamber, but shielded using lead and tungsten shielding, as illustrated in Figure 6-8. The microcontroller boards have been irradiated with a dose rate of 0.870 $Gy.s^{-1}$ and the secondary boards with a dose rate of 2.290 $mGy.s^{-1}$. In addition to the functionality measurements, the current output and the output voltage of the voltage regulator on the secondary board have been measured as well.

The functionality test itself comprises of three main sections, testing the key aspects of the microcontroller functionality. They are presented in the sequence in which they run on the microcontroller. These experiments have been performed until the microcontroller lost all functionality.

Digital Functionality Test

The first part of the sequence tests the digital output of the microcontroller under irradiation. The stability of the digital output functionality can be determined by ascertaining the timing and the output voltage of the microcontroller. The boards have been programmed to output a specific sequence of digital signals. From a digital perspective, these can be considered “LOW” and “HIGH”. From an analog measurement perspective, these would correspond to 0 V and 3.3 V. The output sequence is illustrated in Figure 6-9, it consists of five 25 ms long switches and two

500 ms long switches between the two states. Digital signals are useful for controlling robotic devices and mechanisms.

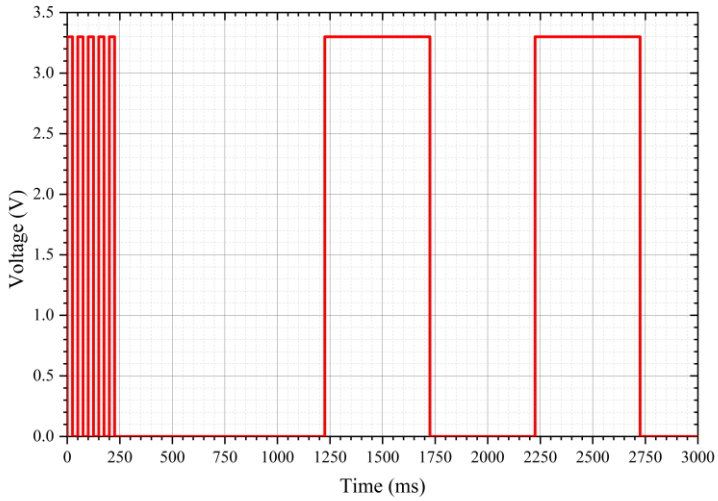

Figure 6-9 Digital test sequence as it is output by the microcontroller before irradiation. [162]

Analog Output Functionality Tests

The second part of the sequence tests the analog output of the microcontroller under irradiation. It consists of two procedures. The first is an analog hold procedure. In this procedure, the microcontroller is programmed to output approximately 2.1 V on one of the analog output connectors for one second and then 0 V for one second. This is then repeated on the other analog output connector. The second is an analog ramp procedure. In this procedure, the microcontroller is programmed to output voltage in discrete voltage steps from 0 V to 3.3 V with 12-bit precision. One step increase per cycle of the code is made, totalling in 4096 steps to reach the maximum. Once the output reaches the maximum value, the procedure is repeated in an inverse way, from 3.3 V to 0 V. This test is designed to diagnose the analog output functionality of the microcontroller, useful for the regulation and control of various systems, such as motor drivers.

Analog Input and Serial Data Transfer Functionality Test

Testing the analog reading capability is not as straightforward as the other tests. There is no obvious way to test it without relying on other components. If the data was read and stored in memory, an assumption is made the memory will not be affected. If the data was directly communicated via any communication connection and protocol, an assumption is made that the communication hardware is not corrupted during the irradiation test. The procedure proposed here attempts to minimise the effect of other components. The microcontroller in the irradiator is connected to a second microcontroller outside of the irradiator. The outside microcontroller outputs an analog voltage sequence of various voltages, each step lasting 100 ms in an infinite loop, as illustrated in Figure 6-10. The inside microcontroller reads these values and then outputs them on one of the analog pins to the DAQ card. It also sends the value it has read over the USB connector to the DAQ laptop. This procedure is then repeated so that the microcontroller outputs the read values through the second analog output connector. The reference signal by the outside microcontroller is recorded as well, allowing a direct comparison between what the irradiated microcontroller reads and attempts to repeat. The analog output test should reveal irregularities in the output system, meaning any difference observed between the effects of irradiation in the previous test and this one. This data could be a good indicator of the microcontrollers ability to read sensors during irradiation.

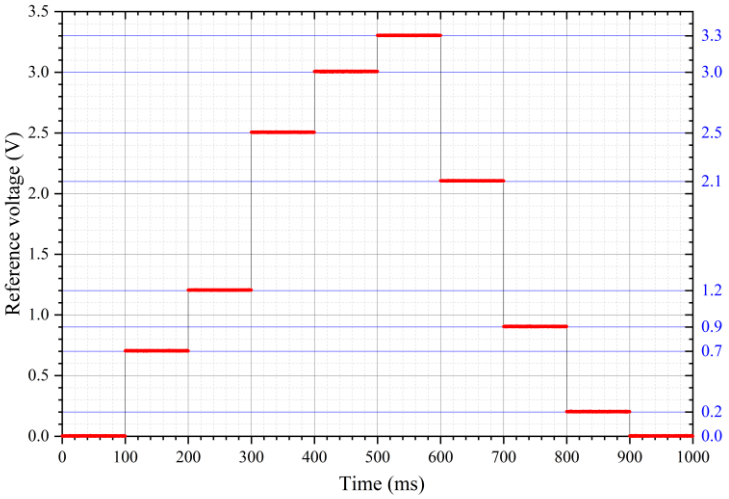

Figure 6-10 Reference signal used in the analog read test. [162]

All of the functionality tests are executed in sequence, taking approximately 10 seconds in total. The DAQ code reading this data has been programmed to read all the data in a 22 second windows, making sure that at least one entire sequence is captured. The code also continuously reads and saves the data sent by the microcontroller through the USB port.

6.8.3.4 Results and Discussion

Voltage Regulator Test

During the preliminary test with the microcontrollers in the oven no difference in output voltage has been observed. This is as expected, as the microcontroller doesn't use a lot of power with a simple code like the one used in this test and 45 °C is not a significantly elevated temperature.

In the first test with the microcontroller boards without modifications all irradiated samples exhibit similar behaviours. The voltage supplied by the voltage regulator consistently decreased as it was irradiated. An example can be seen in Figure 6-11 that shows all of the A samples supplied with a voltage of 4.75 V. The data is almost identical for other voltages as well, indicating the board degrades the same way regardless of supply voltage used.

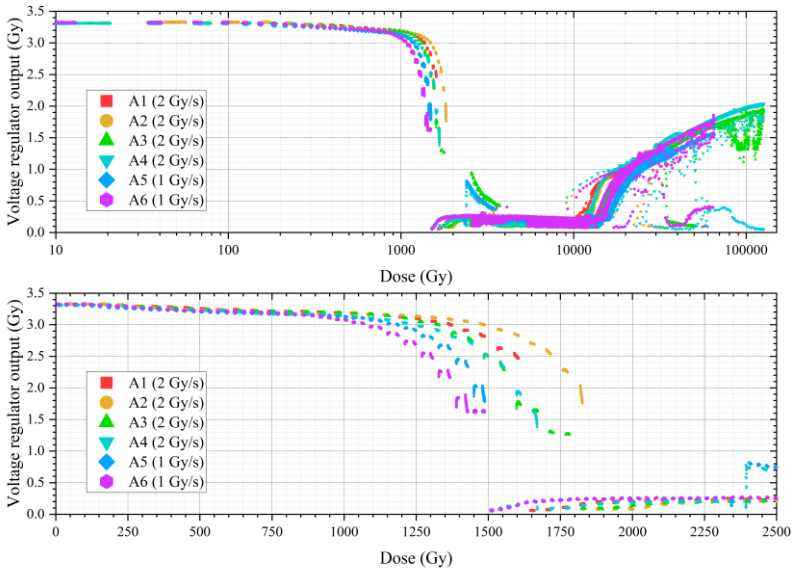

Figure 6-11 Voltage output of the on-board voltage regulator of the microcontroller boards, supplied with 4.75 V under irradiation. [162]

In the C experiments, both voltage and current have been measured, providing more insight into the way the boards degrade from a power supply perspective. An example of these results can be seen in Figure 6-12. It is apparent that the detached and shielded voltage regulator provides more stable voltage output during irradiation. The voltage of the on-board regulator starts decreasing after approximately 100 Gy, as opposed to approximately 400 Gy on the detached voltage regulator. The current output suggests the microcontroller board starts drawing increasingly more current as it is being irradiated. When the current demand from the microcontroller reaches the limit of what the voltage regulator can supply, the voltage drops, possibly due to overload and thermal protection in the regulator.

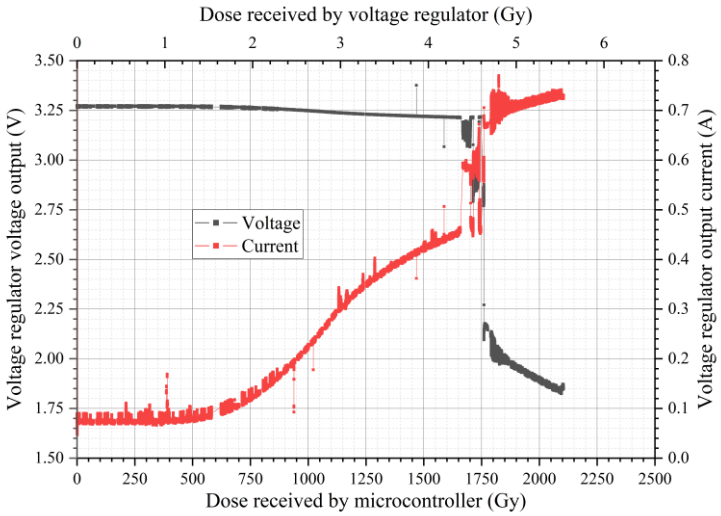

Figure 6-12 Output voltage and current measured on the secondary board of sample C4 as a function of total dose received by the microcontroller. [162]

Digital Output Test

In order to compare individual sequences during irradiation, the data that has been collected has been synchronised to the first rising edge of the procedure. This allows the comparison of the relative timing of the output signal as well as the signal itself. One example of this comparison can be seen in Figure 6-13[13]. The different doses received by the microcontroller at the start of the measurement are illustrated by different colours. The deterioration of the signal is further illustrated by the range of colours used. The example in Figure 6-13 shows, that the voltage decreases as the microcontroller is irradiated. The relative timing of the signal does not change throughout the measurement. In this example however, is the only observed anomaly in the digital output test. At the dose of 1231 Gy, as witnessed in the graph, the microcontroller stopped outputting the programmed signal. However, in further readings in higher doses, it still output the correct sequence before losing all functionality. This loss of functionality and a consequent return to normal operation is the only observed instance in all of the samples. Both B and C samples experience a

[13] In these types of graphs that depict data obtained at discrete total doses reported in the legend, the data in the legend describes the total dose received by the microcontroller at the start of the curve depicted.

similar deterioration pattern, where the timing remains correct but the voltage output decreases as a function of total dose received by the microcontroller.

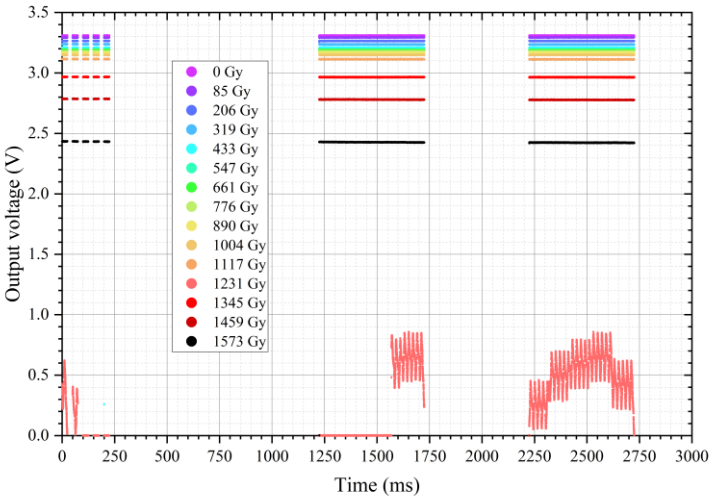

Figure 6-13 Example of the digital data output during irradiation of sample B2. [162]

To compare all of the samples the mean voltage that the microcontroller outputs as 'HIGH' signal has been plotted as a function a total dose received by the microcontroller in Figure 6-14. The B samples report higher initial voltage as the on-board voltage regulator supplies slightly higher voltage than the detached regulator. The results show the B samples degrading faster and almost immediately, while the C samples hold a more steady and consistent voltage. They also suggest a more sudden failure of the C samples as opposed to a progressive deterioration of the B samples. It should be noted that sample C2 lost all functionality (including the tests described below) and did not regain it at approximately 675 Gy, much earlier than all other samples. From an application perspective, it is useful to determine when the output voltage drops too low to be recognised on the receiving end correctly. Using the microcontroller as an example, based on the datasheet [34], voltage of at least 75% of supply voltage will be recognised as 'HIGH' from a digital signal perspective. On a 3.3 V microcontroller board this means that at least 2.5 V will be recognised as digital signal 'HIGH'. This can however vary depending on the system used on the received

end of the data. Based on this, the B samples output sufficient voltage when requested up to approximately 1500 Gy, sample C3 up to 1678 Gy and C4 up to 2023 Gy.

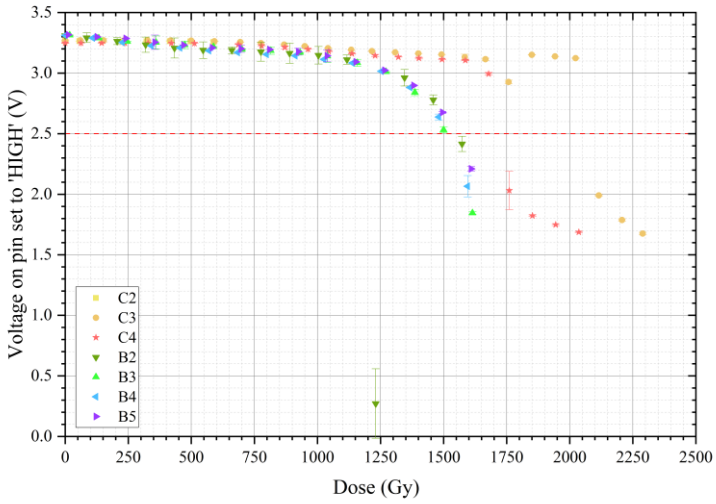

Figure 6-14 Comparison of the digital output performance of all samples during irradiation. Red dashed line indicates 75% of the supply voltage of 3.3 V. [162]

Analog Output Hold Test

In order to compare individual sequences during irradiation, the data that has been collected has been synchronised to the first recorded voltage increase of the procedure. This allows direct comparison of the voltage output and the timing of the signal as well. One example is shown in Figure 6-15. The distinction of total doses received and illustration of deterioration is identical to the depiction in the previous section. The target voltage is also illustrated in the graph with a solid blue line. The relative timing of this procedure remains correct across all of the samples and the voltage output is stable for the vast majority of the observed data. In the depicted example the first decrease in the voltage can be observed after a total dose of 131 Gy. Only the last curve in the graph after approximately 1612 Gy shows observable loss of steadiness of the signal.

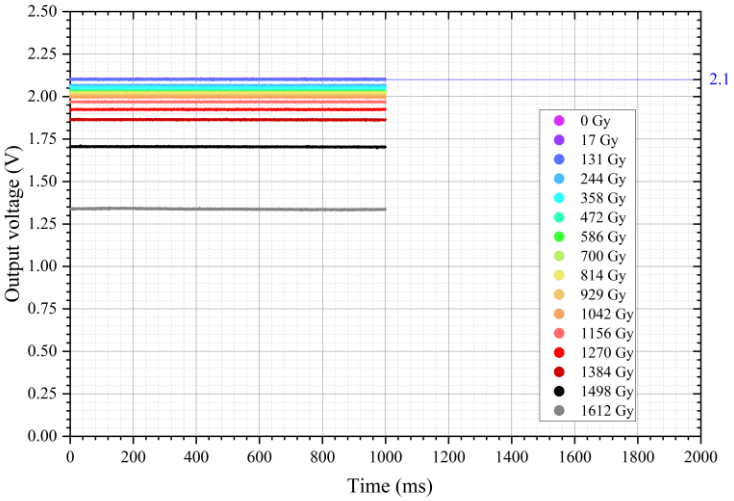

Figure 6-15 Example of the analog hold data output of one of the output pins during irradiation of sample B2.[162]

The average voltage output by the microcontroller when it is instructed to do so has been calculated for all of the samples in order to compare them and this data has been plotted in Figure 6-16 for all samples and both output pins on each sample. The C samples output a lower initial value similarly to the digital data due to the lower voltage supply. The C samples also do not deteriorate until a total dose of approximately 500 Gy, unlike the B samples that start deteriorating very quickly after the start of irradiation. However, in higher total doses, the C samples lose consistency between the two pins on the same board meaning there is little to no difference between the B and C samples in terms of stability.

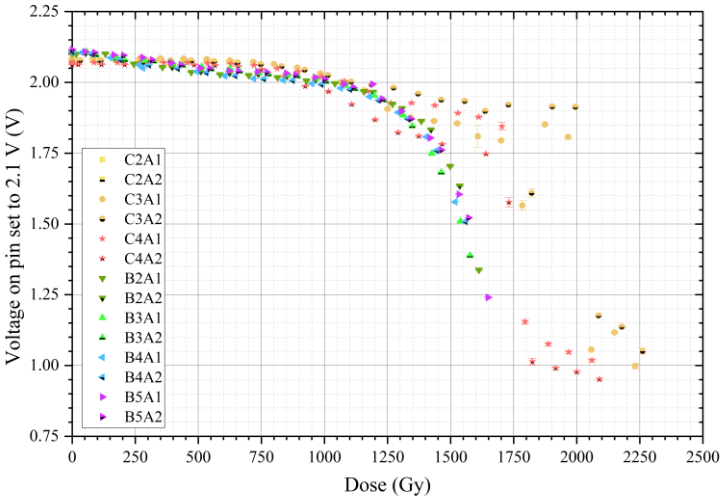

Figure 6-16 Comparison of the analog hold output performance of all samples during irradiation. [162]

Analog Output Ramp Test

In order to compare individual sequences during irradiation, the data that has been collected has been synchronised to the first step above 0 V on the output pin of the microcontroller. This allows for direct comparison of the timing of the individual steps and the steps themselves. One example is shown in Figure 6-17. The distinction of total doses received and illustration of deterioration is identical to the depiction in the previous section. The timing appears to not be affected by the irradiation, as the time from 0 V to peak and time from peak to 0 V are almost identical. The voltage changes proportionally in all of the points the microcontroller outputs. This indicates a connection to the supply voltage, similarly to the previous test.

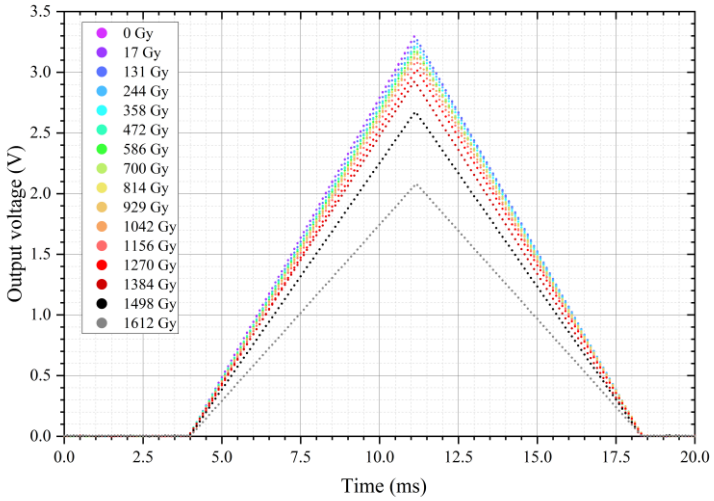

Figure 6-17 Example of the analog hold data output of one of the output pins during irradiation of sample B2. [162]

A comparison between all the samples can be made using the maximum voltage achieved during this procedure on all of the samples and is shown in Figure 6-18. Similarly to the hold test, the C samples report little to no change up to approximately 500 Gy, as opposed to B samples that output decreasing voltage after very low doses. As the dose increases however, unlike in the hold test the C samples do not exhibit a large inconsistency between the pins and degrade observably slower than the B samples. The B samples report better consistency between pins and degrade in a more repeatable pattern.

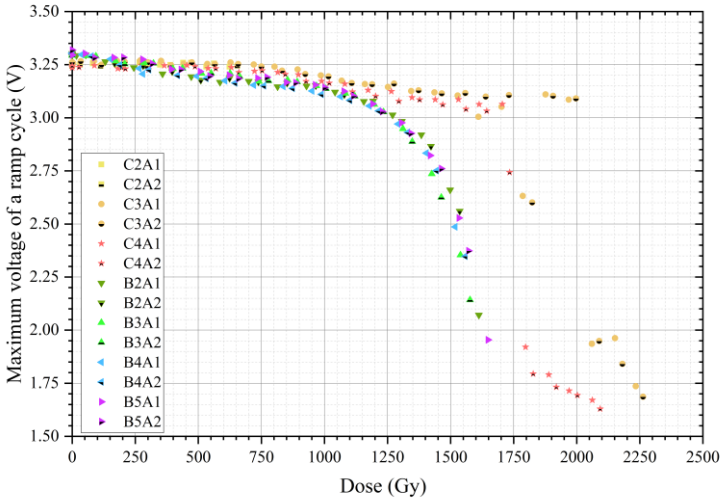

Figure 6-18 Comparison of the analog ramp output performance of all samples during irradiation. [162]

Analog Read and Serial Data Transfer Test

One example of data collected in this procedure is plotted in Figure 6-19. It shows four different measurements taken with the sample C3 – the first is the reference signal that is being output by the external microcontroller. The second is the performance of the microcontroller before the irradiation started. Furthermore, there are two more sets of data at varying total doses. Comparing the reference signal against the 0 Gy data suggests the C samples output voltage slightly higher than it reads (including a slight offset at 0 V), with the exception of the maximum voltage step. This behaviour has not been observed on the B samples. The data also suggests there is sometimes a small delay in changing the value the microcontroller repeats, as seen in the change from 3.3 V to 2.1 V and 0.2 V to 0.0 V on the 0 Gy line. After 354 Gy the offset from reference becomes slightly higher on most points, the 3.0 V step is offset by more than 0.15 V and the microcontroller retains correct timing. After 538 Gy the microcontroller retains correct timing for some steps, however the values it outputs do not correlate with the reference signal (except for the maximum voltage value).

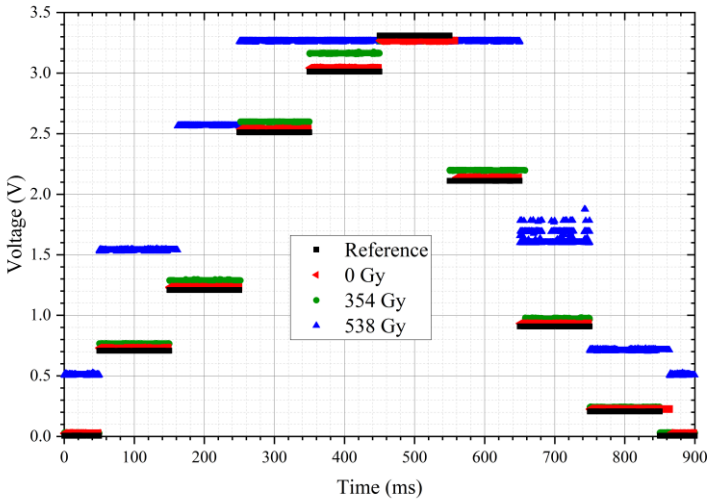

Figure 6-19 Example of data collected during analog read test on one of the output pins of sample C3. [162]

A comparison can be made between all of the samples and both their output pins by calculating the mean absolute deviation from the voltage it is trying to replicate. This data is plotted as a function of total dose received by the microcontroller in Figure 6-20. It is an indicator of the deviation from the reference signal across the entire repeating sequence. It is apparent that the 0 Gy value is higher for the C samples than for the B samples – this is caused partly by a slightly lower voltage being supplied by the detached voltage regulator. Both in B and C samples there is a sudden increase in the deviation from reference. This step change happens at approximately 400 Gy in the C samples and approximately 600 Gy in the B samples. As seen in the previous sections, this is the earliest step change in the function of the microcontroller.

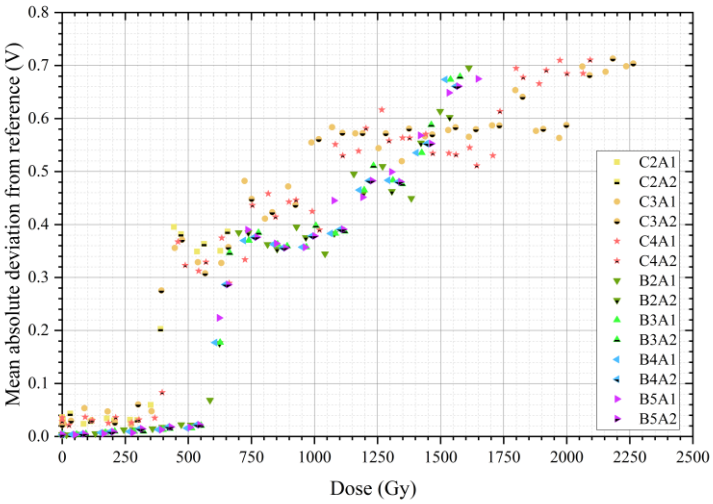

Figure 6-20 Summary of all of the analog read test data. [162]

The serial port connection via USB stopped working at approximately 665 Gy in the sample C2, 724 Gy in the sample C3 and 860 Gy in the sample C4. This failure does not seem to have impacted other functions that the microcontroller was performing as seen in the sections above. A more detailed illustration of the change of deviation from reference voltage at various doses can be found in the appendix.

6.8.3.5 Microcontroller Mode of Failure

It has been mentioned in previous sections that the experiments have been performed until a total loss of function has been observed. In all cases, all of the outputs have been monitored and when they have all stopped outputting signals they were programmed to output the experiment has been allowed to finish one more cycle and then it has been stopped. In most cases, the output pins of the microcontroller have been outputting low voltage noise after failing. A notable exception to this however is the pin used for the digital output tests. An example of the voltage on the pin is shown in Figure 6-21. The graph depicts the voltage on the digital pin on sample C3 shortly after failure. It is apparent that the voltage on the digital pin is not noise and looks similar to a sine wave. However, the step changes are not equal throughout the signal. Proportionally, the steps of voltage the microcontroller outputs are very similar to the reference voltage being output by the external microcontroller. The reference voltage appears to be affected by this – the maximum voltage step of 3.3 V is indistinguishable from the previous step, 2.9 V as the external microcontroller seemingly does not change voltage from 2.9 to 3.3 V.

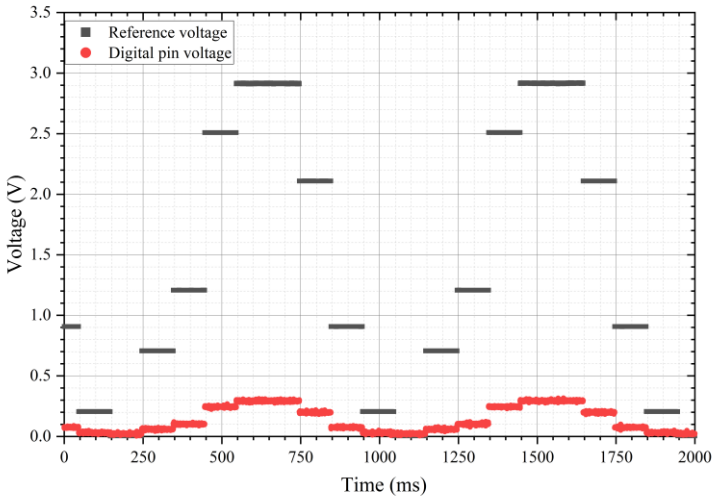

Figure 6-21 Digital pin output of the sample C3 after failing to output the programmed data after a total dose of approximately 2307 Gy. [162]

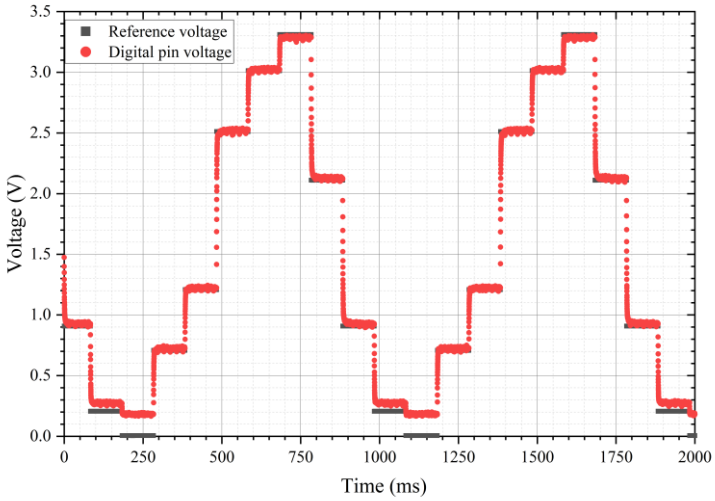

Figure 6-22 Digital pin output of the sample C2 after failing to output the programmed data after a total dose of approximately 1421 Gy. [162]

Figure 6-22 further reinforces the assumption that the reference voltage being fed to the irradiated microcontroller is responsible for this pattern on the output pin. In this example, on the sample C2 the maximum voltage on the digital pin kept rising after failure. It can be seen that after approximately 1421 Gy, the voltage on the digital pin matches the reference voltage almost perfectly. There is considerable leading edge when the voltage changes and the voltage on the pin does not drop to 0 V even when the reference voltage does, however other steps are almost identical. These pins are not programmed to output analog voltage nor should they be capable of doing so.

6.9 Conclusions

The radiation testing of the COTS potentiometers suggests high resilience to gamma radiation in both types up to very high TIDs. While material selection remains critical not only for the potentiometers but other components in their vicinity, the results suggest no special considerations are necessary for their use in hazardous environments. The resistive elements used to deliver the functionality of the potentiometers do not seem to be affected by the radiation, the only observable effect was on the physical appearance of some of the components of the potentiometers.

The radiation testing of COTS microcontrollers revealed higher resilience than initially anticipated. The microcontrollers can remain applicable for applications that only require digital output functions up to 1 kGy and data acquisition is still usable up to approximately 350 Gy with relatively low impact. While no data is available for comparison, the lack of radiation hardness of the components used in the microcontroller boards means that these can be considered very high total doses. The impact is further lowered and the overall survivability of the microcontroller is extended using a relatively simple modification in detaching or shielding the voltage regulator.

The behaviour of the microcontrollers is also a novel dataset as literature does not focus on observing their behaviour this way during irradiation. The data and observed changes in voltage during irradiation could serve as the foundation of new methodologies for irradiation testing of electronics for use in nuclear decommissioning environments.

Total expected doses will vary significantly with deployment scenarios, however, the repeatable, predictable manner with which the microcontrollers failed could potentially be used as a source of information itself. Devices using sacrificial design - expected to fail but still performing their planned functions until failure could be monitored and the response of the microcontroller through time would be indicative of the TID the microcontroller is subjected to. Considering the price and availability of these microcontrollers, exploration, characterisation or even automated monitoring activities would potentially benefit from their use.

Further testing would be necessary to ensure other factor do not have more severe impact on the performance of the microcontroller – for example, whether memory

functions remain unaffected throughout irradiation would require separate testing and different dose rates (particularly much lower dose rates that would be observed in monitoring scenarios). Overall, the microcontroller appears to be suitable for one-off or potentially sacrificial rapidly prototyped devices for use in hazardous environments.

7 Conclusions and Future Work Suggestions

7.1 Conclusions

The first aim of this work was to propose an alternative approach to the rheological assessment of hazardous substances. Through the development of two different viscometer prototypes it has been demonstrated that it is possible to deliver rheological assessment of sludge remotely, using minimal amount of electronic components and with a compact device capable of fitting through very small openings. Two different approaches are discussed, each presenting a different view on rheological assessment of sludge that could provide valuable information about legacy waste in nuclear decommissioning scenarios.

The development of the first prototype has shown that the proposed design is suitable for an *in situ* analysis tool for hazardous environment. It can be calibrated against any machine for direct data comparison and it is appropriate to use non-standard geometries do deliver the measurements. The use of COTS components and rapid prototyping proved to be invaluable and many of the components used and manufactured are robust enough for nuclear decommissioning environments. The resilience of modern 3D printing filaments such as ABS and reinforced polypropylene and the quick manufacturing it provides has the potential to save money in many applications in the nuclear industry. COTS potentiometer used in the design proved to be sufficiently robust for active environments as well.

Deployment of these technologies is dependent on the deployment location however several methods already exist and would be available for use. First, manual deployment where operator presence is available is the most straightforward option. This could be applied for smaller containers such as barrels. Second, underwater

devices have already been deployed and they could be used to deploy the viscometer designs proposed in this thesis. This is particularly suited for deployment in pools and other larger structures with settled beds of materials. For more complex or automated deployment options the devices are compact and low in weight to not pose significant challenges for use on robotic platforms, however specifics would be closely linked to concrete deployment scenarios. The device can also potentially be scaled in size to accommodate other deployment access sizes.

The second aim of this work was to determine the suitability of novel rapid prototyping techniques and COTS components for use in nuclear decommissioning environments. Through radiation testing of several COTS electronic components, it has been shown that these components exhibit good resilience to gamma radiation – a crucial quality necessary for components to be deployed in nuclear decommissioning environments. Furthermore, new approaches for testing these components have been utilised in every test in order to determine real life effect on the devices in deployment scenarios.

The irradiation testing of potentiometers used in both prototypes suggests that the components are very resilient to gamma radiation and suitable for active environments. This shows promise for the quick development of prototypes using COTS components that aren't necessarily rated as radiation tolerant. While some change has been observed across the measured range of TID, it was always within manufacturers specification and has negligible impact on the performance of the devices designed using the potentiometers. This is in line with expectations, as potentiometers are fundamentally very simple devices. Further investigations should focus on application specific devices as previous testing should be considered more as

a suggestion for similar component selection rather than proof that similar devices will perform the same.

The irradiation testing of microcontrollers has shown that COTS microcontroller boards have the potential to be applied in harsh environments, including gamma radiation fields. While they degrade and the main functionality impacted appears to be data acquisition, the output functionality remained acceptable for hundreds of Gy of gamma radiation from a ^{60}Co source. A relatively simple modification in detaching the voltage regulator has improved the functionality and suggests that adapting COTS electronic components for use in active environments is worth exploring.

7.2 Suggestions for Future Work

There are some areas that could be further explored to improve the quality of the data the prototypes output and expand the academic knowledge on some of the challenges encountered. The use of non-standard geometries has proved to be suitable in the measurement range used in the experiments described above, but it might prove beneficial for some applications to explore a wider range of rotational velocities. This could enable the use of the prototype not only for cleanout and decommissioning purposes but also for inspection and process monitoring. These applications would also benefit from a cheap, disposable and robust tool to use on hazardous substances. The further optimisation of non-standard geometries and their validation using both theoretical simulations and high-precision benchtop instruments would certainly be a novel contribution to the application of rotational vane rheometry, not only in remote environments.

Development for specific deployment locations should focus on two main aspects. First, it is important to ensure that the calibration and test materials are appropriate.

These choices further inform the selection of components such as springs and could result in using different test materials more representative substances expected to be measured *in situ*. Second, the design must take into account the specifics of the environments. This includes tailoring construction materials appropriate for the expected hazards, decontamination and disposal considerations. An example of an initial deployment scenario would be manual deployment in easily accessible, smaller containers. This would be a good initial test before scaling the experiments for more complex deployment scenarios, integrating them into existing deployment technologies in ponds and other vessels.

Exploring these non-standard geometries in suspensions in wider measurement conditions would also require increased focus on the onset of secondary flow effects. As it stands, secondary flow effects in suspensions sheared using vanes is an unexplored topic in the literature and greatly limits the use of vanes to relatively low rotational velocities in most materials, irrespective if they adhere to a specific standard or not. Quantifying these effects in suspensions would help establish the working envelope more precisely for a wider variety of geometries and potentially extend it using a more robust non-linearity compensation procedure.

The development of the second prototype has shown that it is possible to design a very compact viscometer design capable of providing a shear stress ramp type measurements using rapid prototyping. In the context of exploring the movability of sludge in nuclear decommissioning environments the torque range it outputs in its current form would be applicable, however for lower viscosity samples further work would be necessary to optimise the design to output lower torque. The potential use for the prototype lies mainly in validation and comparative rheology to obtain quick datasets with a low cost, easily manufactured device. Further work to optimise the

design and prepare it for deployment would be the appropriate next step for the development of the prototype, possibly utilising other rapid prototyping methods such as 3D metal printing.

The next step in investigating the radiation tolerance of the microcontroller board should focus on testing the memory systems, as they are the main component not tested in this thesis and while no impact has been observed, no conclusions can be drawn about the resilience of the memory modules. Furthermore a model deployment situation, such as a monitoring scenario using sensors, should be investigated using irradiator facilities. This would help illustrate the deployment potential of the platform and help establish very specific operational boundaries for deployment.

There is no clearly defined irradiation testing methodology that could be readily applied to components that are to be used in nuclear decommissioning environments. Establishing a new methodology that takes into account that the devices are expected to be used during irradiation and attempts to quantify the resilience of devices by establishing an acceptable level of deterioration would underpin the development of sacrificial, low cost devices using COTS components. This has the potential to lower costs and development times in developing new technologies.

The use of rapid prototyping is very likely to continue growing in all industries and the nuclear industry would certainly benefit from further studies into the suitability of 3D printing materials for use in hazardous environments. 3D printing has delivered robust, high quality components for the prototypes and their mechanical properties and available research suggest they could prove highly beneficial for use in nuclear decommissioning environments. Some of the commonly used materials have been tested and the results are available in the literature, but a systematic effort to optimise

not only the material, but the print settings for use in active environments is possibly the main topic that has not been investigated so far. The impact of layer height, infill amount and pattern of the infill are the main properties that should be investigated in combination with gamma radiation using standard elongation and impact techniques normally used to ascertain the mechanical properties of materials. Furthermore, multi-material printing using one printer is possible as well and the implications for use in hazardous environments are worth exploring. The potential of using an expensive, difficult to use material to create a protective outer layer in combination with a more common material for the internal structure could provide further opportunities for the development of various devices. All of this work could potentially further reinforce the case for the use of rapid prototyping in order to lower manufacturing times and costs for a wide range of applications in hazardous environments.

References

[1] Department for Business Energy & Industrial Strategy, “Digest of UK Energy Statistics (DUKES): electricity,” 2020. https://www.gov.uk/government/statistics/electricity-chapter-5-digest-of-united-kingdom-energy-statistics-dukes (accessed Apr. 14, 2021).

[2] I. Crossland and National Nuclear Laboratory, *Nuclear fuel cycle science and engineering*. Woodhead Publishing Series in Energy, 2012.

[3] Department for Business Energy and Industrial Strategy, “Policy paper - Nuclear Sector Deal,” 2018. https://www.gov.uk/government/publications/nuclear-sector-deal/nuclear-sector-deal (accessed Sep. 09, 2020).

[4] Nuclear Decommissioning Authority and Sellafield Ltd, “History made as final fuel leaves iconic nuclear plant,” 2019. https://www.gov.uk/government/news/history-made-as-final-fuel-leaves-iconic-nuclear-plant (accessed Sep. 09, 2020).

[5] National Audit Office, “Nuclear power in the UK,” 2016. https://www.nao.org.uk/wp-content/uploads/2016/07/Nuclear-power-in-the-UK.pdf (accessed Mar. 11, 2021).

[6] Sellafield Ltd, “Sellafield Plan,” 2011. https://www.cumbria.gov.uk/eLibrary/Content/Internet/538/755/1929/17716/17720/17722/41333114920.pdf (accessed Feb. 10, 2021).

[7] Sellafield Ltd, “Green light to restart Magnox Reprocessing,” 2020. https://www.gov.uk/government/news/green-light-to-restart-magnox-reprocessing (accessed Mar. 11, 2021).

[8] GOV.UK, “End of reprocessing at Thorp signals new era for Sellafield,” 2018. https://www.gov.uk/government/news/end-of-reprocessing-at-thorp-signals-new-era-for-sellafield (accessed Mar. 19, 2019).

[9] Sellafield Ltd, “Sellafield Ltd Corporate plan 2016/17,” 2017.

https://www.gov.uk/government/uploads/system/uploads/attachment_data/file/627566/SEL11098_corporate-plan_web.pdf (accessed Mar. 19, 2019).

[10] H. Paterson, “How much radioactive waste is there in the world?,” 2019. https://nda.blog.gov.uk/2019/08/02/how-much-radioactive-waste-is-there-in-the-world/ (accessed Sep. 09, 2020).

[11] J. Woodfield, “How much radioactive waste is there in the UK?,” 2020. https://nda.blog.gov.uk/2020/01/10/how-much-radioactive-waste-is-there-in-the-uk/ (accessed Sep. 09, 2020).

[12] Department for Business Energy & Industrial Strategy, “2019 UK RADIOACTIVE WASTE INVENTORY,” 2019. https://ukinventory.nda.gov.uk/wp-content/uploads/2020/01/2019-Waste-Report-Final.pdf (accessed Mar. 11, 2021).

[13] C. R. Bayliss, *Nuclear decommissioning, waste management, and environmental site remediation*. Elsevier Butterworth-Heinemann, 2003.

[14] GOV.UK, “About us - Nuclear Decommissioning Authority.” https://www.gov.uk/government/organisations/nuclear-decommissioning-authority/about (accessed Sep. 09, 2020).

[15] Westinghouse Electric Company LLC, “Westinghouse Springfields > Products,” 2020. https://www.westinghousenuclear.com/springfields/products (accessed Sep. 14, 2020).

[16] Nuclear Decommissioning Authority - GOV.UK, “Nuclear Provision: the cost of cleaning up Britain’s historic nuclear sites - GOV.UK,” 2019. https://www.gov.uk/government/publications/nuclear-provision-explaining-the-cost-of-cleaning-up-britains-nuclear-legacy/nuclear-provision-explaining-the-cost-of-cleaning-up-britains-nuclear-legacy (accessed Sep. 08, 2020).

[17] Sellafield Ltd, “Sellafield Ltd Context Plan,” 2016. https://www.gov.uk/government/uploads/system/uploads/attachment_data/file/649731/Context_Plan_Issue_2_May_2017.pdf (accessed Mar. 11, 2021).

[18] Washington State Department of Ecology, “Tank waste management - Washington State Department of Ecology,” 2020.

https://ecology.wa.gov/Waste-Toxics/Nuclear-waste/Hanford-cleanup/Tank-waste-management (accessed Sep. 15, 2020).

[19] Savannah River Nuclear Solutions LLC, “Facts from the Savannah River Site.” https://www.srs.gov/general/news/factsheets/srs_overview.pdf (accessed Mar. 11, 2021).

[20] P. G. Martin, O. D. Payton, J. S. Fardoulis, D. A. Richards, Y. Yamashiki, and T. B. Scott, “Low altitude unmanned aerial vehicle for characterising remediation effectiveness following the FDNPP accident,” *J Env. Radioact*, vol. 151, pp. 58–63, 2016, doi: 10.1016/j.jenvrad.2015.09.007.

[21] P. G. Martin *et al.*, “3D unmanned aerial vehicle radiation mapping for assessing contaminant distribution and mobility,” *Int. J. Appl. earth Obs. Geoinf.*, vol. 52, pp. 12–19, 2016, doi: 10.1016/j.jag.2016.05.007.

[22] A. Griffiths, A. Dikarev, P. R. Green, B. Lennox, X. Poteau, and S. Watson, “AVEXIS - Aqua vehicle explorer for in-situ sensing,” *IEEE Robot. Autom. Lett.*, vol. 1, no. 1, pp. 282–287, 2016, doi: 10.1109/LRA.2016.2519947.

[23] M. Nancekievill *et al.*, “Detection of simulated fukushima daichii fuel debris using a remotely operated vehicle at the naraha test facility,” *Sensors (Switzerland)*, vol. 19, no. 20, 2019, doi: 10.3390/s19204602.

[24] K. Groves, A. West, K. Gornicki, S. Watson, J. Carrasco, and B. Lennox, “MallARD: An Autonomous Aquatic Surface Vehicle for Inspection and Monitoring of Wet Nuclear Storage Facilities,” *Robot.*, vol. 8, no. 2, p. 47, 2019, doi: 10.3390/robotics8020047.

[25] H. Peel, “MIRRAX DATA SHEET,” 2020. https://uomrobotics.com/onewebmedia/MIRRAX-Data-sheet-2019.pdf (accessed Mar. 11, 2021).

[26] C. Ducros *et al.*, “RICA: A Tracked Robot for Sampling and Radiological Characterization in the Nuclear Field,” *J. F. Robot.*, vol. 34, no. 3, pp. 583–599, 2017, doi: 10.1002/rob.21650.

[27] W. Lee, M. Hirai, and S. Hirose, “Gunryu III: reconfigurable magnetic wall-climbing robot for decommissioning of nuclear reactor,” *Adv. Robot.*, vol. 27,

no. 14, pp. 1099–1111, 2013, doi: 10.1080/01691864.2013.812174.

[28] C.-H. Choi, S.-H. Jung, and S.-H. Kim, “Feeder Pipe Inspection Robot Using an Inch-Worm Mechanism with Pneumatic Actuators,” in *2004 IEEE International Conference on Robotics and Biomimetics*, 2004, pp. 889–894, doi: 10.1109/ROBIO.2004.1521902.

[29] B. Bird *et al.*, “A Robot to Monitor Nuclear Facilities: Using Autonomous Radiation-Monitoring Assistance to Reduce Risk and Cost,” *IEEE Robot. Autom. Mag.*, vol. 26, no. 1, pp. 35–43, 2019, doi: 10.1109/mra.2018.2879755.

[30] D. T. Connor *et al.*, “Application of airborne photogrammetry for the visualisation and assessment of contamination migration arising from a Fukushima waste storage facility,” *Environ. Pollut.*, vol. 234, pp. 610–619, 2018, doi: 10.1016/j.envpol.2017.10.098.

[31] Y. Sato *et al.*, “Remote radiation imaging system using a compact gamma-ray imager mounted on a multicopter drone,” *J. Nucl. Sci. Technol.*, vol. 55, no. 1, pp. 90–96, 2018, doi: 10.1080/00223131.2017.1383211.

[32] M. Nancekievill *et al.*, “Development of a Radiological Characterization Submersible ROV for Use at Fukushima Daiichi,” *IEEE Trans. Nucl. Sci.*, vol. 65, no. 9, pp. 2565–2572, 2018, doi: 10.1109/TNS.2018.2858563.

[33] Sellafield Ltd, “The 2017/18 Technology Development and Delivery Summary,” 2018. https://www.gov.uk/government/publications/the-201718-technology-development-and-delivery-summary (accessed Mar. 11, 2021).

[34] J. Bux, J. Peakall, S. Biggs, and T. N. Hunter, “In situ characterisation of a concentrated colloidal titanium dioxide settling suspension and associated bed development: Application of an acoustic backscatter system,” *Powder Technol.*, vol. 284, no. C, pp. 530–540, 2015, doi: 10.1016/j.powtec.2015.07.028.

[35] B. D. Keele, R. S. Addleman, G. R. Blewett, C. S. Mcclellan, and G. L. Troyer, “Non-destructive in situ measurement of radiological distributions in Hanford Site waste tanks,” *IEEE Trans. Nucl. Sci.*, vol. 43, no. 3, pp. 1821–1826, 1996, doi: 10.1109/23.507229.

[36] M. Z. Martin, S. Allman, D. J. Brice, R. C. Martin, and N. O. Andre,

"Exploring laser-induced breakdown spectroscopy for nuclear materials analysis and in-situ applications," *Spectrochim. Acta Part B At. Spectrosc.*, vol. 74 75, p. 177, 2012.

[37] S. Delepine-Lesoille *et al.*, "France's State of the Art Distributed Optical Fibre Sensors Qualified for the Monitoring of the French Underground Repository for High Level and Intermediate Level Long Lived Radioactive Wastes," *Sensors (Basel)*, vol. 17, no. 6, p. 1377, 2017, doi: 10.3390/s17061377.

[38] J. A. Botha *et al.*, "Quartz crystal microbalance as a device to measure the yield stress of colloidal suspensions," *Colloids Surfaces A Physicochem. Eng. Asp.*, vol. 546, pp. 179–185, 2018, doi: 10.1016/j.colsurfa.2018.03.005.

[39] N. J. Alderman and N. I. Heywood, "The Importance of Rheological Assessment in the Mobilisation, Mixing and Transport of Nuclear Waste Sludges," in *37th Annual Radioactive Waste Management Symposium 2011 (WM 2011)*, 2011.

[40] NEA Task Group on Decontamination, "Decontamination Techniques Used in Decommissioning Activities," 1999. http://www.oecd-nea.org/rwm/reports/1999/decontec.pdf (accessed Mar. 11, 2021).

[41] D. Gurau and R. Deju, "The use of chemical gel for decontamination during decommissioning of nuclear facilities," *Radiat. Phys. Chem. Oxf. Engl. 1993.*, vol. 106, pp. 371–375, 2015, doi: 10.1016/j.radphyschem.2014.08.022.

[42] A. A. Pujol-Pozo, F. Monroy-Guzmán, and E. Bustos, "Advanced oxidation process for the decontamination of stainless steels containing uranium," *J. Mater. Sci. Mater. Electron.*, vol. 29, no. 18, pp. 15754–15760, 2018, doi: 10.1007/s10854-018-9229-3.

[43] G. Greifzu, T. Kahl, M. Herrmann, W. Lippmann, and A. Hurtado, "Laser-based decontamination of metal surfaces," *Opt. laser Technol.*, vol. 117, pp. 293–298, 2019, doi: 10.1016/j.optlastec.2019.04.037.

[44] T. N. Hunter, L. Darlison, J. Peakall, and S. Biggs, "Using a multi-frequency acoustic backscatter system as an in situ high concentration dispersion monitor," *Chem. Eng. Sci.*, vol. 80, pp. 409–418, 2012, doi: https://doi.org/10.1016/j.ces.2012.06.038.

[45] Technical Working Group of the Nuclear Industry Safety and D. Forum, “Best Available Techniques (BAT) for the Management of the Generation and Disposal of Radioactive Wastes.” 2010.

[46] C. W. Macosko, *Rheology : principles, measurements, and applications*. VCH, 1994.

[47] F. M. White, *Fluid mechanics, 7th ed.* McGraw-Hill, 2011.

[48] H. A. Barnes, “Thixotropy—a review,” *J. Nonnewton. Fluid Mech.*, vol. 70, no. 1, pp. 1–33, 1997, doi: 10.1016/S0377-0257(97)00004-9.

[49] X. Cheng, J. H. McCoy, J. N. Israelachvili, and I. Cohen, “Imaging the microscopic structure of shear thinning and thickening colloidal suspensions.,” *Science (80-.).*, vol. 333, no. 6047, p. 1276, 2011, doi: 10.1126/science.1207032.

[50] L. B. Chen, B. J. Ackerson, and C. F. Zukoski, “Rheological consequences of microstructural transitions in colloidal crystals,” *J. Rheol. (N. Y. N. Y).*, vol. 38, no. 2, pp. 193–216, 1994, doi: 10.1122/1.550498.

[51] D. Kalman and N. Wagner, “Microstructure of shear-thickening concentrated suspensions determined by flow-USANS,” *Rheol. Acta*, vol. 48, no. 8, pp. 897–908, 2009, doi: 10.1007/s00397-009-0351-2.

[52] H. Kanai and T. Amari, “Negative thixotropy in ferric-oxide suspensions,” *An Int. J. Rheol.*, vol. 34, no. 3, pp. 303–310, 1995, doi: 10.1007/BF00396021.

[53] H. A. Barnes, J. F. Hutton, and K. Walters, *An Introduction to Rheology*. Elsevier Science, 1989.

[54] D. S. Keller and D. V Keller, “An investigation of the shear thickening and antithixotropic behavior of concentrated coal–water dispersions,” *J. Rheol. (N. Y. N. Y).*, vol. 34, no. 8, pp. 1267–1291, 1990, doi: 10.1122/1.550086.

[55] T. Osswald and N. Rudolph, “Polymer Rheology - Fundamentals and Applications.” Hanser Publishers, [Online]. Available: https://app.knovel.com/hotlink/toc/id:kpPRFA0005/polymer-rheology-fundamentals/polymer-rheology-fundamentals.

[56] A. Einstein, “Eine neue Bestimmung der Moleküldimensionen,” *Ann. Phys.*, vol. 324, no. 2, pp. 289–306, Jan. 1906, doi: 10.1002/andp.19063240204.

[57] A. Einstein, “Berichtigung zu meiner Arbeit: „Eine neue Bestimmung der Moleküldimensionen”,” *Ann. Phys.*, vol. 339, no. 3, pp. 591–592, Jan. 1911, doi: 10.1002/andp.19113390313.

[58] B. P. Ho and L. G. Leal, “Inertial migration of rigid spheres in two-dimensional unidirectional flows,” *J. Fluid Mech.*, vol. 65, no. 2, pp. 365–400, 1974, doi: DOI: 10.1017/S0022112074001431.

[59] G. K. Batchelor, “The effect of Brownian motion on the bulk stress in a suspension of spherical particles,” *J. Fluid Mech.*, vol. 83, no. 1, pp. 97–117, 1977, doi: DOI: 10.1017/S0022112077001062.

[60] I. M. Krieger and T. J. Dougherty, “A Mechanism for Non-Newtonian Flow in Suspensions of Rigid Spheres,” *Trans. Soc. Rheol.*, vol. 3, no. 1, pp. 137–152, Mar. 1959, doi: 10.1122/1.548848.

[61] M. M. Cross, “Rheology of non-Newtonian fluids: A new flow equation for pseudoplastic systems,” *J. Colloid Sci.*, vol. 20, no. 5, pp. 417–437, 1965, doi: 10.1016/0095-8522(65)90022-X.

[62] P. J. Carreau, “Rheological Equations from Molecular Network Theories,” *Trans. Soc. Rheol.*, vol. 16, no. 1, pp. 99–127, Mar. 1972, doi: 10.1122/1.549276.

[63] E. C. Bingham and U. States., “An investigation of the laws of plastic flow.” U.S. Dept. of Commerce, Bureau of Standards : U.S. Govt. Print. Off., Washington, D.C., pp. 309–353, 1917, [Online]. Available: file://catalog.hathitrust.org/Record/009487703.

[64] W. H. Herschel and R. Bulkley, “Konsistenzmessungen von Gummi-Benzollösungen,” *Kolloid-Zeitschrift*, vol. 39, no. 4, pp. 291–300, 1926, doi: 10.1007/BF01432034.

[65] M. Mooney and R. H. Ewart, “The Conicylindrical Viscometer,” *Physics (College. Park. Md).*, vol. 5, no. 11, pp. 350–354, 1934, doi: 10.1063/1.1745219.

[66] P. Dontula, C. W. Macosko, and L. E. Scriven, “Origins of concentric cylinders viscometry,” *J. Rheol. (N. Y. N. Y).*, vol. 49, no. 4, pp. 807–818, 2005, doi: 10.1122/1.1940640.

[67] Q. Nguyen and D. V Boger, “Measuring the Flow Properties of Yield Stress Fluids,” *Annu. Rev. Fluid Mech.*, vol. 24, pp. 47–88, 1992.

[68] H. A. Barnes and Q. D. Nguyen, “Rotating vane rheometry — a review,” *Journal of Non-Newtonian Fluid Mechanics*, vol. 98, no. 1. pp. 1–14, 2001, doi: 10.1016/S0377-0257(01)00095-7.

[69] C. E. Owens, A. J. Hart, and G. H. Mckinley, “Improved rheometry of yield stress fluids using bespoke fractal 3D printed vanes,” *J. Rheol. (N. Y. N. Y).*, vol. 64, no. 3, pp. 643–662, 2020, doi: 10.1122/1.5132340.

[70] G. I. Taylor, “Stability of a Viscous Liquid Contained between Two Rotating Cylinders,” *Philos. Trans. R. Soc. London. Ser. A, Contain. Pap. a Math. or Phys. Character*, vol. 223, no. 605, pp. 289–343, 1923, doi: 10.1098/rsta.1923.0008.

[71] A. Rozgus, “A material issue: How to select a rheometer or viscometer,” *Res. Dev.*, vol. 44, no. 3, pp. 31–33, 2002.

[72] H. A. Barnes, H. Schimanski, and D. Bell, “30 Years of Progress in Viscometers and Rheometers,” *Appl. Rheol.*, vol. 9, no. 2, pp. 69–76, 1999, doi: https://doi.org/10.1515/arh-2009-0006.

[73] R. Buchdahl and G. Curado, “Viscosimeter,” US patent 2553844, 1951.

[74] AMETEK.Inc, “Dial Reading Viscometer,” 2019. https://www.brookfieldengineering.com/products/viscometers/laboratory-viscometers/dial-reading-viscometer (accessed Jun. 16, 2020).

[75] D. W. Brookfield, “Apparatus for measuring viscosity and other fluid properties,” US patent 2679750, 1954.

[76] R. J. Murphy, Jr., “Apparatus and method for measuring viscosity,” US patent 4571988, 1986.

[77] D. A. Brookfield, “Viscometer with a continuously variable electronic

readout," US patent 4448061, 1984.

[78] D. A. Brookfield, "Portable viscometer," US patent 5503003, 1996.

[79] D. A. Brookfield and R. P. Bishop, "Viscometer usable in situ in large reactor vessels," US patent 5531102, 1996.

[80] Hydramotion Ltd, "Viscolite Portable Viscometer | Hand-held Viscometer," 2020. https://hydramotion.com/en/products/viscolite (accessed Jun. 18, 2020).

[81] PCE Instruments™, "Portable Viscometer / Viscosity Meter PCE-RVI 3 VP20 | PCE Instruments," 2020. https://www.pce-instruments.com/english/measuring-instruments/test-meters/viscometer-viscosity-meter-pce-instruments-portable-viscometer-viscosity-meter-pce-rvi-3-vp20-det_313405.htm (accessed Jun. 18, 2020).

[82] D. A. Brookfield, "Rheometer system," US patent 5167143, 1992.

[83] G. Raffer, "Process for determining the rheological properties of materials," US patent 9255872B2, 2016.

[84] J. Läuger and M. Krenn, "Rheometer and rheometric method for testing samples," US patent 8453496B2, 2013.

[85] R. W. Hall, "Rotational rheometer," US patent 6698275B2, 2004.

[86] Brookfield AMETEK, "More Solutions to Sticky Problems." 2017, [Online]. Available: https://www.brookfieldengineering.com/-/media/ametekbrookfield/tech sheets/more solutions 2017.pdf?la=en.

[87] B. J. Briscoe, M. Glaese, P. F. Luckham, and S. Ren, "The falling of spheres through Bingham fluids," *Colloids and Surfaces*, vol. 65, no. 1, pp. 69–75, 1992, doi: 10.1016/0166-6622(92)80176-3.

[88] P. Reardon, A. Graham, S. Feng, V. Chawla, R. Admuthe, and L. Mondy, "Non-Newtonian end effects in falling ball viscometry of concentrated suspensions," *Rheol. Acta*, vol. 46, no. 3, pp. 413–424, 2007, doi: 10.1007/s00397-006-0138-7.

[89] V. Ros-Polski, F. L. Schmidt, A. A. Vitali, A. Marsaioli, and V. G. S. Raghavan, "Rheological Analysis of Sucrose Solution at High Temperatures

Using a Microwave-Heated Pressurized Capillary Rheometer," *J. Food Sci.*, vol. 79, no. 4, pp. E540–E545, 2014, doi: 10.1111/1750-3841.12398.

[90] S. Pollak, S. Hüttemann, S. E. Quiñones-Cisneros, and E. Weidner, "Development and calibration of a high pressure high shear rate capillary rheometer," *J. Pet. Sci. Eng.*, vol. 157, pp. 581–587, 2017, doi: 10.1016/j.petrol.2017.07.056.

[91] A. T. Morita, M. S. Toma, and M.-A. De Paoli, "Low cost capillary rheometer, transfer molding and die-drawing module," *Polym. Test.*, vol. 25, no. 2, pp. 197–202, 2006, doi: 10.1016/j.polymertesting.2005.10.008.

[92] I. Dufour *et al.*, "The Microcantilever: A Versatile Tool for Measuring the Rheological Properties of Complex Fluids," *J. Sensors*, vol. 2012, no. 2012, 2012, doi: 10.1155/2012/719898.

[93] H. Barnes and K. Walters, "The yield stress myth?," *An Int. J. Rheol.*, vol. 24, no. 4, pp. 323–326, 1985, doi: 10.1007/BF01333960.

[94] D. M. Husband, N. Aksel, and W. Gleissle, "The existence of static yield stresses in suspensions containing noncolloidal particles," *J. Rheol. (N. Y. N. Y).*, vol. 37, no. 2, pp. 215–235, Mar. 1993, doi: 10.1122/1.550442.

[95] J. P. Hartnett and R. Y. Z. Hu, "Technical note: The yield stress—An engineering reality," *J. Rheol. (N. Y. N. Y).*, vol. 33, no. 4, pp. 671–679, 1989, doi: 10.1122/1.550006.

[96] H. Barnes, "The 'yield stress myth?' paper - 21 years on," *Appl. Rheol.*, vol. 17, no. 4, 2007.

[97] W. H. Fischer, W. H. Bauer, and S. E. Wiberley, "Yield Stresses and Flow Properties of Carboxypolymethylene-Water Systems," *Trans. Soc. Rheol.*, vol. 5, no. 1, pp. 221–235, 1961, doi: 10.1122/1.548896.

[98] R. Reshma, M. Daas, R. Srivastava, and B. Tansel, "Resuspension of non-Newtonian slurries by submerged jet-nozzles," *Exp. Therm. fluid Sci.*, vol. 31, no. 7, pp. 771–778, 2007, doi: 10.1016/j.expthermflusci.2006.05.013.

[99] J. J. Hastings, D. Rhodes, A. S. Fellerman, D. Mckendrick, and C. Dixon, "New approaches for sludge management in the nuclear industry," *Powder*

Technol., vol. 174, no. 1, pp. 18–24, 2007, doi: 10.1016/j.powtec.2006.10.015.

[100] S. R. Biggs *et al.*, "Engineering Properties, Hydraulic Behaviour and Theoretical Modelling of Nuclear Waste Flows," in *37th Annual Radioactive Waste Management Symposium 2011 (WM 2011)*, 2011.

[101] N. Paul, "Characterisation of highly active nuclear waste simulants," University of Leeds, 2014.

[102] R. A. Peterson *et al.*, "Review of the Scientific Understanding of Radioactive Waste at the U.S. DOE Hanford Site," *Environ. Sci. Technol*, vol. 52, no. 2, pp. 381–396, 2018, doi: 10.1021/acs.est.7b04077.

[103] B. Dunnett, T. Ward, R. Roberts, and J. Cheesewright, "Physical Properties of Highly Active Liquor Containing Molybdate Solids," *Procedia Chem.*, vol. 21, pp. 24–31, 2016, doi: 10.1016/j.proche.2016.10.004.

[104] P. A. Smith, D. R. Rector, and A. Shekarriz, "Microstructural and Rheological Characterization of Colloidal Aggregates of Nuclear Waste Slurries," *Miner. Process. Extr. Metall. Rev.*, vol. 20, no. 1, pp. 311–324, 2000, doi: 10.1080/08827509908962480.

[105] J. Chun, T. Oh, M. Luna, and M. Schweiger, "Effect of particle size distribution on slurry rheology: Nuclear waste simulant slurries," *Colloids Surf. A. Physicochem. Eng. Asp.*, vol. 384, no. 1–3, pp. 304–310, 2011, doi: 10.1016/j.colsurfa.2011.04.003.

[106] E. M. Tracey, P. A. Smith, and E. V Morrey, "Rheology of concentrated, heterogeneous slurries containing > 1M electrolyte — a case study in nuclear waste suspensions," *J. Nucl. Mater.*, vol. 230, no. 1, pp. 19–35, 1996, doi: 10.1016/0022-3115(96)00025-6.

[107] S. Biggs, M. Fairweather, T. Hunter, Q. Omokanye, and J. Peakall, "Engineering Properties of Nuclear Waste Slurries," no. 44076. pp. 353–360, 2009, [Online]. Available: http://dx.doi.org/10.1115/ICEM2009-16378.

[108] C. Chang and P. A. Smith, "Flow-induced structure in a system of nuclear waste simulant slurries," *Rheol. acta*, vol. 35, no. 4, pp. 382–389, 1996, doi: 10.1007/BF00403539.

[109] L. F. Pease, R. C. Daniel, and C. A. Burns, “Slurry rheology of Hanford sludge,” *Chem. Eng. Sci.*, vol. 199, pp. 628–634, 2019, doi: 10.1016/j.ces.2018.12.044.

[110] Ultimaker, “Ultimaker PLA TDS - Ultimaker Support,” 2020. https://support.ultimaker.com/hc/en-us/articles/360011962720-Ultimaker-PLA-TDS (accessed Jun. 08, 2020).

[111] Ultimaker, “Ultimaker ABS TDS - Ultimaker Support,” 2020. https://support.ultimaker.com/hc/en-us/articles/360012759139-Ultimaker-ABS-TDS (accessed Jun. 08, 2020).

[112] Ultimaker, “Ultimaker CPE TDS - Ultimaker Support,” 2020. https://support.ultimaker.com/hc/en-us/articles/360012061099-Ultimaker-CPE-TDS (accessed Jun. 08, 2020).

[113] Owens Corning, “XSTRAND® GF30-PP - Owens Corning Composites,” 2020. https://www.owenscorning.com/composites/product/xstrand-gf30-pp (accessed Jun. 08, 2020).

[114] BSI, *BS EN ISO 3219:1995 BS 2782-7: Method 730B: 1994 Plastics — Polymers/resins in the liquid state or as emulsions or dispersions — Determination of viscosity using a rotational viscometer with defined shear rate*. British Standards Institution, 1994.

[115] T. Fried, D. Cheneler, S. D. Monk, C. J. Taylor, and J. M. Dodds, “Compact Viscometer Prototype for Remote In Situ Analysis of Sludge,” *Sensors* , vol. 19, no. 15. 2019, doi: 10.3390/s19153299.

[116] Arduino Team, “Arduino.h.” 2019, [Online]. Available: https://github.com/arduino/ArduinoCore-avr/blob/master/cores/arduino/Arduino.h.

[117] L. Badea, “StepperDriver.h.” 2017, [Online]. Available: https://github.com/laurb9/StepperDriver/blob/master/src/DRV8834.h.

[118] S. Audry, T. O. Fredericks, and R. Tillaart, “Chrono.h.” 2017, [Online]. Available: https://github.com/SofaPirate/Chrono/blob/master/Chrono.h.

[119] N. Paul, R. B. Hammond, T. N. Hunter, M. Edmondson, L. Maxwell, and S.

Biggs, “Synthesis of nuclear waste simulants by reaction precipitation: Formation of caesium phosphomolybdate, zirconium molybdate and morphology modification with citratomolybdate complex,” *Polyhedron*, vol. 89, no. C, pp. 129–141, 2015, doi: 10.1016/j.poly.2014.12.030.

[120] SKF, “The SKF model for calculating the frictional moment.” p. 15, [Online]. Available: https://www.skf.com/binaries/pub12/Images/0901d1968065e9e7-The-SKF-model-for-calculating-the-frictional-moment_tcm_12-299767.pdf.

[121] Engineering ToolBox, “Friction and Friction Coefficients,” 2004. https://www.engineeringtoolbox.com/friction-coefficients-d_778.html (accessed Sep. 21, 2021).

[122] E. H. Ibe, *Terrestrial radiation effects in ULSI devices and electronic systems*. Singapore, 2014.

[123] Q. Wang *et al.*, “Application of a 3D-Printed Navigation Mold in Puncture Drainage for Brainstem Hemorrhage,” *J. Surg. Res.*, vol. 245, pp. 99–106, 2020, doi: https://doi.org/10.1016/j.jss.2019.07.026.

[124] T. Prater, N. Werkheiser, F. Ledbetter, D. Timucin, K. Wheeler, and M. Snyder, “3D Printing in Zero G Technology Demonstration Mission: complete experimental results and summary of related material modeling efforts,” *Int. J. Adv. Manuf. Technol.*, vol. 101, no. 1, pp. 391–417, 2019, doi: 10.1007/s00170-018-2827-7.

[125] P. Wady *et al.*, “Effect of ionising radiation on the mechanical and structural properties of 3D printed plastics,” *Addit. Manuf.*, vol. 31, 2020, doi: 10.1016/j.addma.2019.100907.

[126] C. West, R. McTaggart, T. Letcher, D. Raynie, and R. Roy, “Effects of Gamma Irradiation Upon the Mechanical and Chemical Properties of 3D-Printed Samples of Polylactic Acid,” *J. Manuf. Sci. Eng.*, vol. 141, no. 4, Feb. 2019, doi: 10.1115/1.4042581.

[127] S. Shaffer, K. Yang, J. Vargas, M. A. Di Prima, and W. Voit, “On reducing anisotropy in 3D printed polymers via ionizing radiation,” *Polymer (Guildf).*, vol. 55, no. 23, pp. 5969–5979, 2014, doi: 10.1016/j.polymer.2014.07.054.

[128] B. Rankouhi, F. Delfanian, R. McTaggart, and T. Letcher, “An Experimental Investigation of the Effects of Gamma Radiation on 3D Printed ABS for In-Space Manufacturing Purposes.” Nov. 11, 2016, doi: 10.1115/IMECE2016-67745.

[129] H. Schönbacher and A. Stolarz-Izycka, *Compilation of radiation damage test data: cable insulating materials. Index des résultats d’essais de radiorésistance: matériaux d’isolation de câbles, pt.1*. Geneva: CERN, 1979.

[130] E. Salem, N. Mostafa, M. M. Hassan, and M. Mohsen, “Effects Induced by Gamma Irradiation on Free-Volumes, Mechanical, and Thermal Properties of Flame- and Non Flame-Retardant Polyvinylchloride,” *J. Appl. Polym. Sci.*, vol. 113, no. 1, pp. 199–206, 2009, doi: 10.1002/app.29582.

[131] European Space Agency, *The Radiation Design Handbook*. Paris: ESA, 1993.

[132] M. Tavlet and H. Schönbacher, *Compilation of radiation damage test data, part 1 2nd edition.: Halogen-free cable-insulating materials*. Geneva: CERN, 1989.

[133] D. J. Hamman and C. L. Hanks, *Radiation effects design handbook. Section 3 - Electrical insulating materials and capacitors*. Washington: NASA, 1971.

[134] I. R. Sinclair, *Passive components for circuit design*. Newnes, 2000.

[135] J. G. Fossum, H. H. Sander, and H. J. Gerwin, “The effects of ionizing radiation on diffused resistors,” *IEEE Trans. Nucl. Sci.*, vol. 21, no. 6, pp. 315–322, 1974, doi: 10.1109/TNS.1974.6498947.

[136] A. G. Holmes-Siedle, *Handbook of radiation effects*, 2nd ed. Oxford University Press, 2002.

[137] J. Alderman, P. K. Job, R. C. Martin, C. M. Simmons, and G. D. Owen, “Measurement of radiation-induced demagnetization of Nd–Fe–B permanent magnets,” *Nucl. Instruments Methods Phys. Res. Sect. A Accel. Spectrometers, Detect. Assoc. Equip.*, vol. 481, no. 1, pp. 9–28, 2002, doi: https://doi.org/10.1016/S0168-9002(01)01329-8.

[138] R. S. Gao, L. Zhen, G. A. Li, C. Y. Xu, and W. Z. Shao, “Effect of γ-ray irradiation on the magnetic properties of NdFeB and Fe–Cr–Co permanent magnets,” *J. Magn. Magn. Mater.*, vol. 302, no. 1, pp. 156–159, 2006, doi:

https://doi.org/10.1016/j.jmmm.2005.09.018.

[139] R. Roy and A. Pandya, “Evaluation of gamma and neutron irradiation effects on the properties of mica film capacitors,” *Bull. Mater. Sci.*, vol. 28, no. 7, pp. 719–724, 2005, doi: 10.1007/BF02708543.

[140] K. Sharashar and S. Kayed, “Experimental study of total ionizing dose radiation effects on MOS capacitor.” pp. 88–91, 2002, doi: 10.1109/EWAED.2002.1177881.

[141] V. K. Khanna, *Extreme-temperature and harsh-environment electronics: Physics, technology and applications*. 2017.

[142] R. N. Nowlin, E. W. Enlow, R. D. Schrimpf, and W. E. Combs, “Trends in the total-dose response of modern bipolar transistors,” *Nucl. Sci. IEEE Trans.*, vol. 39, no. 6, pp. 2026–2035, 1992, doi: 10.1109/23.211400.

[143] A. H. Johnston, C. I. Lee, and B. G. Rax, “Enhanced damage in bipolar devices at low dose rates: effects at very low dose rates,” *Nucl. Sci. IEEE Trans.*, vol. 43, no. 6, pp. 3049–3059, 1996, doi: 10.1109/23.556904.

[144] P. E. Dodd and L. W. Massengill, “Basic mechanisms and modeling of single-event upset in digital microelectronics,” *Nucl. Sci. IEEE Trans.*, vol. 50, no. 3, pp. 583–602, 2003, doi: 10.1109/TNS.2003.813129.

[145] P. E. Dodd, M. R. Shaneyfelt, J. A. Felix, and J. R. Schwank, “Production and propagation of single-event transients in high-speed digital logic ICs,” *Nucl. Sci. IEEE Trans.*, vol. 51, no. 6, pp. 3278–3284, 2004, doi: 10.1109/TNS.2004.839172.

[146] J. M. Benedetto, P. H. Eaton, D. G. Mavis, M. Gadlage, and T. Turflinger, “Digital Single Event Transient Trends With Technology Node Scaling,” *Nucl. Sci. IEEE Trans.*, vol. 53, no. 6, pp. 3462–3465, 2006, doi: 10.1109/TNS.2006.886044.

[147] B. L. Gregory and B. D. Shafer, “Latch-Up in CMOS Integrated Circuits,” *Nucl. Sci. IEEE Trans.*, vol. 20, no. 6, pp. 293–299, 1973, doi: 10.1109/TNS.1973.4327410.

[148] G. Bruguier and J.-M. Palau, “Single particle-induced latchup,” *Nucl. Sci. IEEE*

Trans., vol. 43, no. 2, pp. 522–532, 1996, doi: 10.1109/23.490898.

[149] H. Shindou, S. Kuboyama, T. Hirao, and S. Matsuda, “Local and pseudo SELs observed in digital LSIs and their implication to SEL test method,” *Nucl. Sci. IEEE Trans.*, vol. 52, no. 6, pp. 2638–2641, 2005, doi: 10.1109/TNS.2005.861081.

[150] J. L. Titus, G. H. Johnson, R. D. Schrimpf, and K. F. Galloway, “Single-event burnout of power bipolar junction transistors,” *Nucl. Sci. IEEE Trans.*, vol. 38, no. 6, pp. 1315–1322, 1991, doi: 10.1109/23.124111.

[151] A. M. Albadri, R. D. Schrimpf, K. F. Galloway, and D. G. Walker, “Single event burnout in power diodes: Mechanisms and models,” *Microelectron. Reliab.*, vol. 46, no. 2, pp. 317–325, 2006, doi: 10.1016/j.microrel.2005.06.015.

[152] J. L. Titus, “An Updated Perspective of Single Event Gate Rupture and Single Event Burnout in Power MOSFETs,” *Nucl. Sci. IEEE Trans.*, vol. 60, no. 3, pp. 1912–1928, 2013, doi: 10.1109/TNS.2013.2252194.

[153] J. R. Brews, M. Allenspach, R. D. Schrimpf, K. F. Galloway, J. L. Titus, and C. F. Wheatley, “A conceptual model of a single-event gate-rupture in power MOSFETs,” *Nucl. Sci. IEEE Trans.*, vol. 40, no. 6, pp. 1959–1966, 1993, doi: 10.1109/23.273457.

[154] S. Kuboyama, N. Ikeda, E. Mizuta, H. Abe, T. Hirao, and T. Tamura, “Rediscovery of Single-Event Gate Rupture Mechanism in Power MOSFETs,” *Nucl. Sci. IEEE Trans.*, vol. 59, no. 4, pp. 749–754, 2012, doi: 10.1109/TNS.2012.2201501.

[155] F. W. Sexton, “Destructive single-event effects in semiconductor devices and ICs,” *Nucl. Sci. IEEE Trans.*, vol. 50, no. 3, pp. 603–621, 2003, doi: 10.1109/TNS.2003.813137.

[156] A. Wilson, M. Von Thun, B. Baranski, R. Anderson, and A. Turnbull, “Radiation Effects Characterization of an Arm®-Based 32-bit Microcontroller,” in *2018 IEEE Nuclear and Space Radiation Effects Conference, NSREC 2018*, 2018, pp. 1–7, doi: 10.1109/NSREC.2018.8584302.

[157] J. Xiaoming *et al.*, “Radiation effect in CMOS microprocessor exposed to

intense mixed neutron and gamma radiation field," in *Proceedings of the European Conference on Radiation and its Effects on Components and Systems, RADECS*, 2013, pp. 1–4, doi: 10.1109/RADECS.2013.6937406.

[158] H. Quinn, T. Fairbanks, J. L. Tripp, G. Duran, and B. Lopez, "Single-event effects in low-cost, low-power microprocessors," in *IEEE Radiation Effects Data Workshop*, 2014, vol. 2015-Janua, no. January, pp. 1–9, doi: 10.1109/REDW.2014.7004596.

[159] S. M. Guertin, M. Amrbar, and S. Vartanian, "Radiation test results for common CubeSat microcontrollers and microprocessors," *IEEE Radiation Effects Data Workshop*, vol. 2015-Novem. pp. 1–9, 2015, doi: 10.1109/REDW.2015.7336730.

[160] Bourns®, "6630 - Precision Potentiometer REV. 11/19." 2019, [Online]. Available: https://www.bourns.com/docs/technical-documents/obsolete-parts/6630_obsolete.pdf?sfvrsn=da8047f6_16.

[161] Department of Defense, "MIL-STD-883K w/CHANGE 2," 2017. http://everyspec.com/MIL-STD/MIL-STD-0800-0899/MIL-STD-883K_54326/ (accessed Mar. 11, 2021).

[162] T. Fried *et al.*, "Radiation testing of low cost, commercial off the shelf microcontroller board," *Nucl. Eng. Technol.*, vol. 53, no. 10, pp. 3335–3343, 2021, doi: https://doi.org/10.1016/j.net.2021.05.005.

Appendices

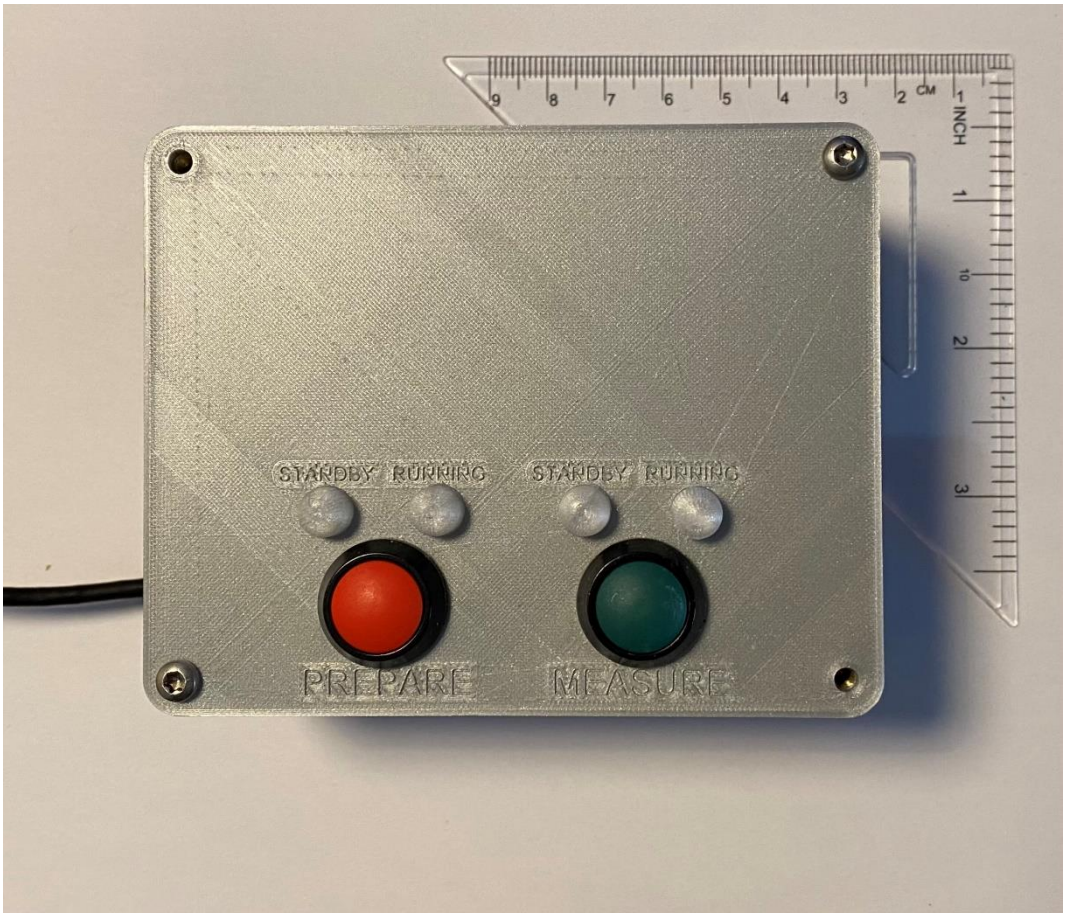

Figure A-1 Control unit of the shear rate ramp prototype.

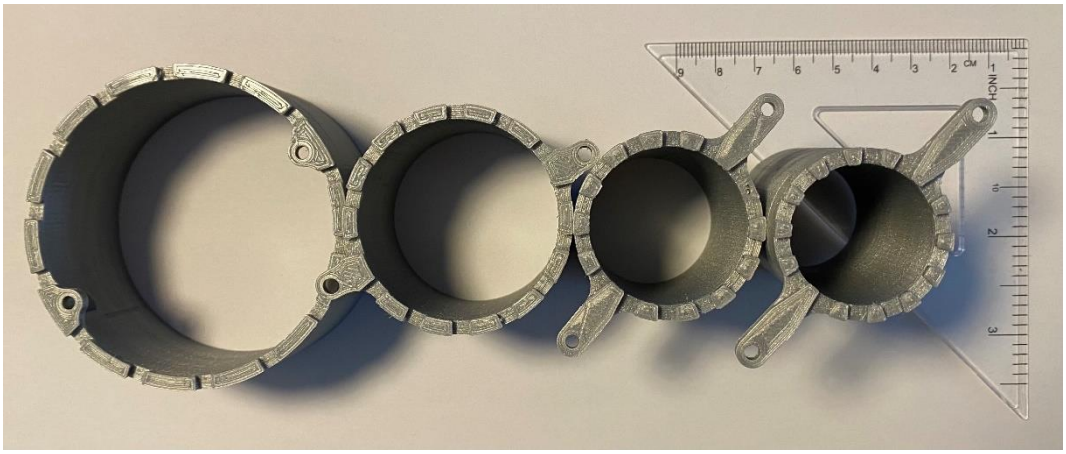

Figure A-2 Cups used with the shear rate ramp prototype; from left to right – 3, 2, 1 and ISO size cups.

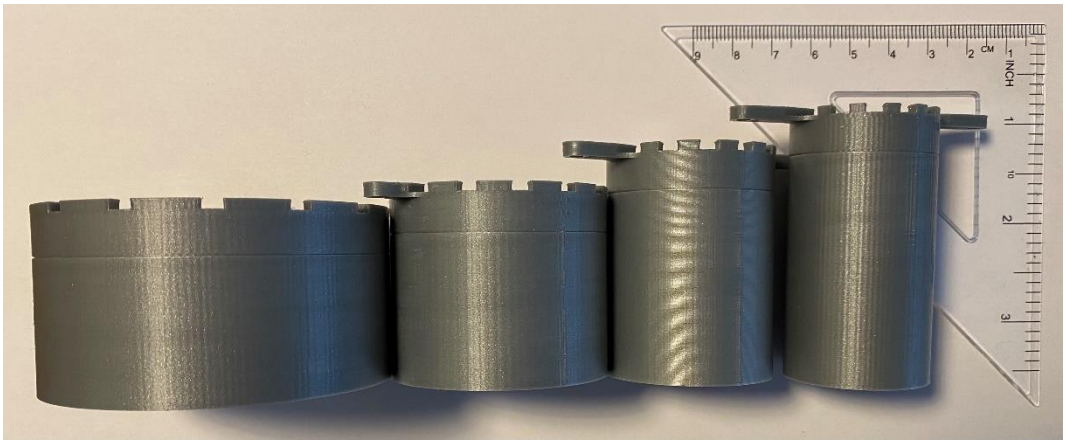

Figure A-3 Cups used with the shear rate ramp prototype; from left to right – 3, 2, 1 and ISO size cups.

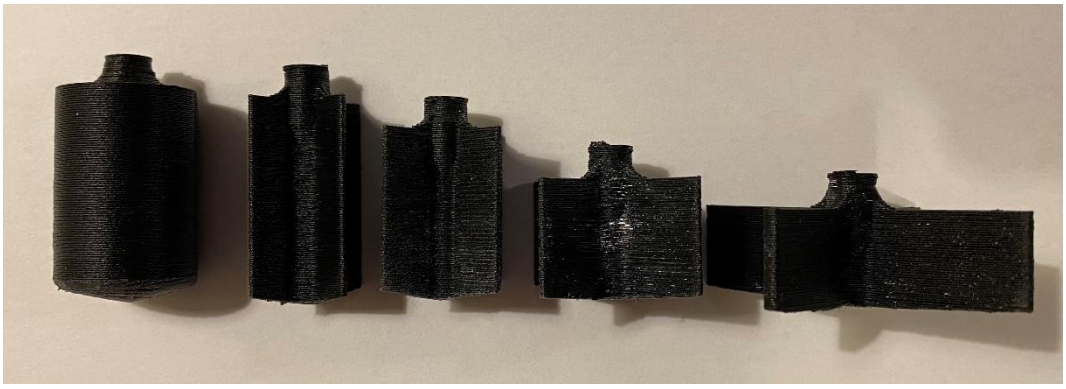

Figure A-4 Geometries used with the shear rate ramp prototype; from left to right – ISO C25 bob, ISO V25 vane, Vane 1, Vane 2, Vane 3.

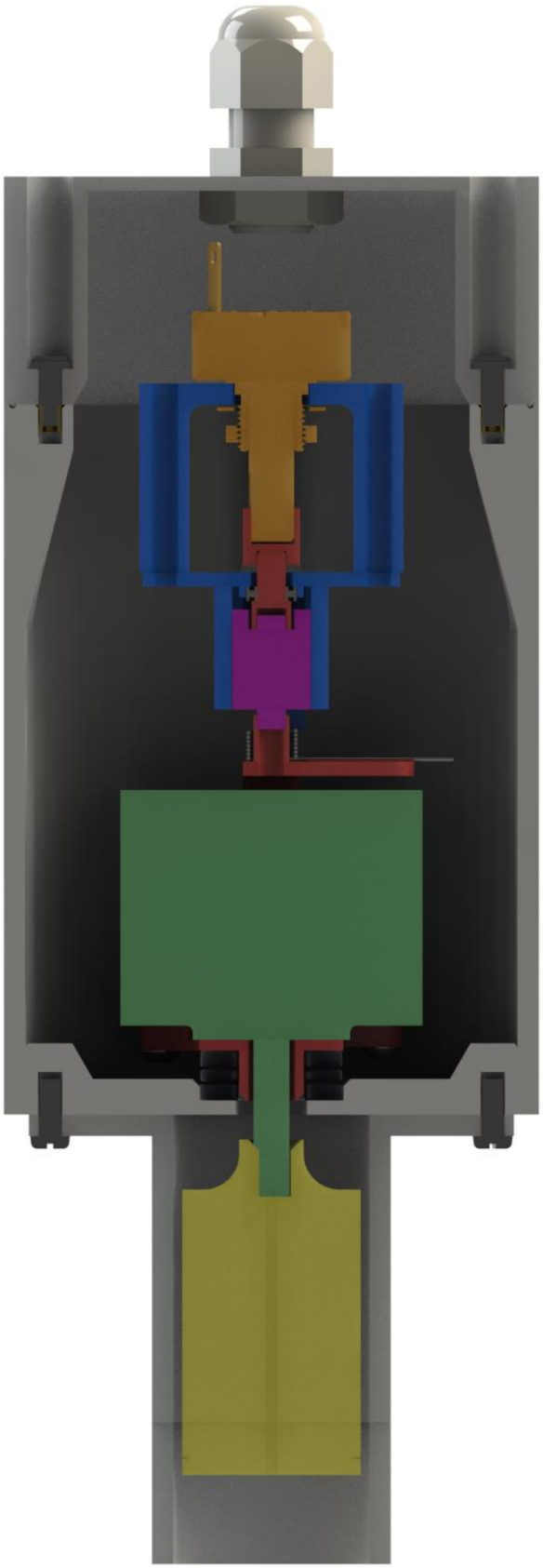

Figure A-5 Model of the shear rate ramp prototype as seen in a cross-section through the centre of the prototype.

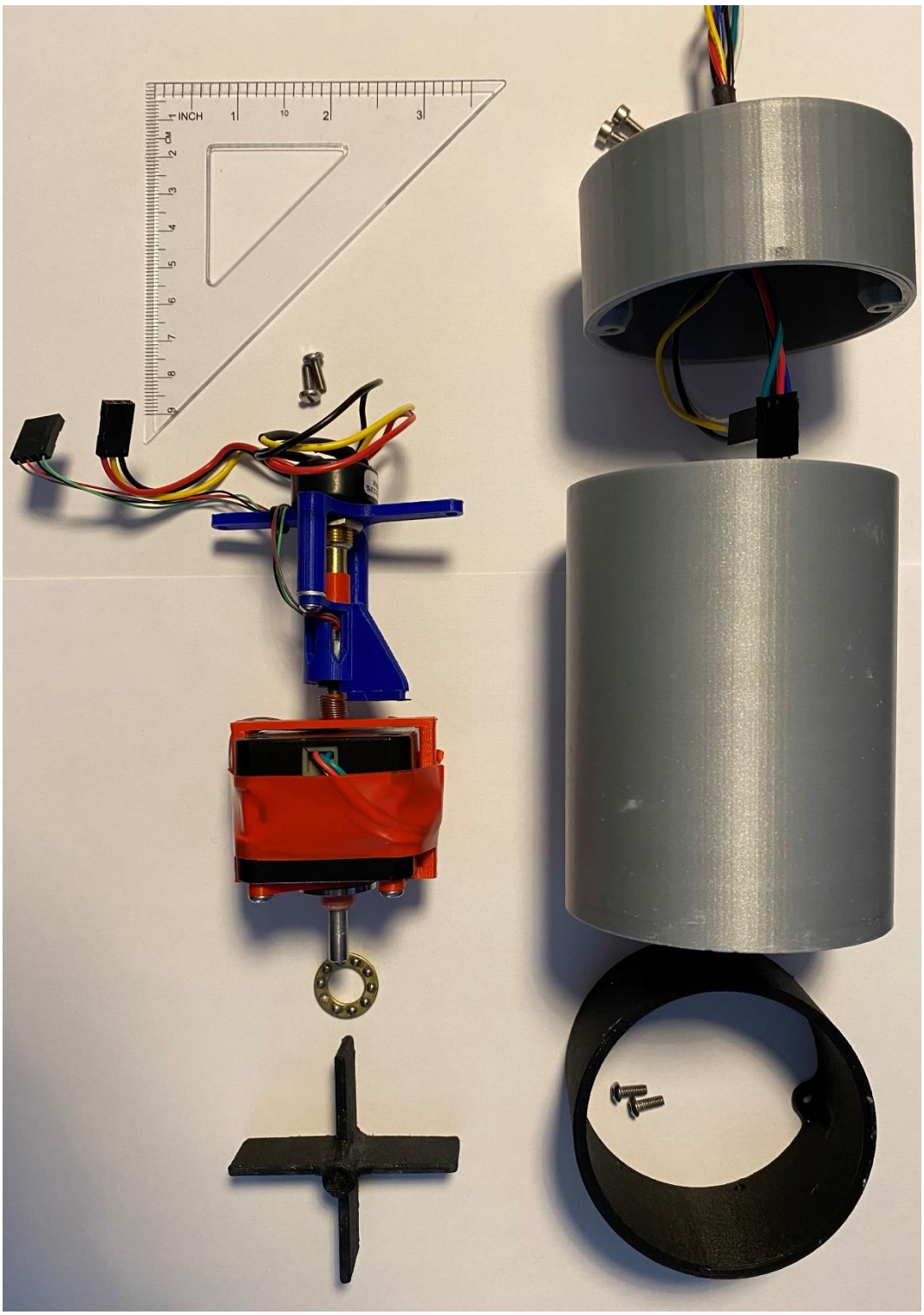

Figure A-6 Partially disassembled shear rate ramp prototype.

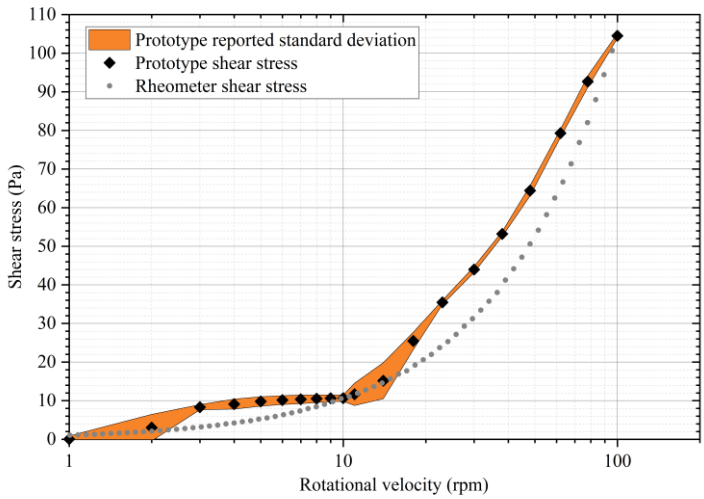

Figure A-7 Final calibration curve of the first prototype using the ISO Bob geometry [115].

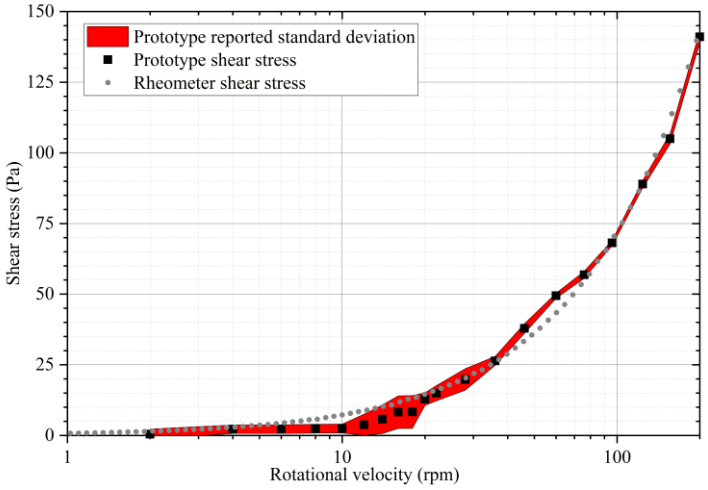

Figure A-8 Final calibration curve of the first prototype using the ISO Vane geometry [115].

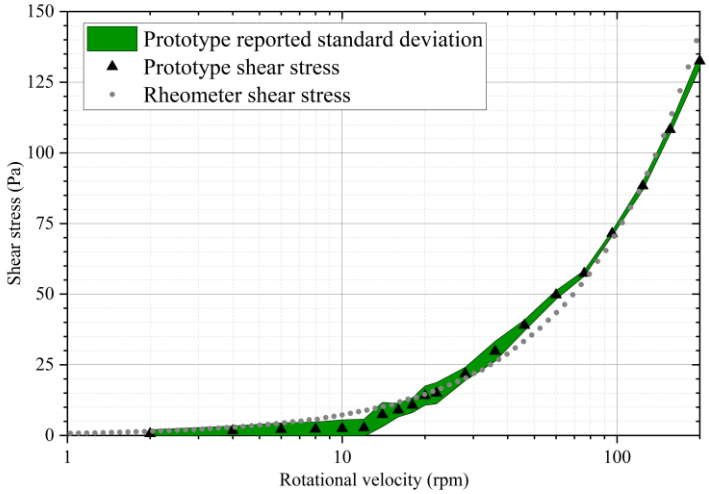

Figure A-9 Final calibration curve of the first prototype using the Vane 1 geometry [115].

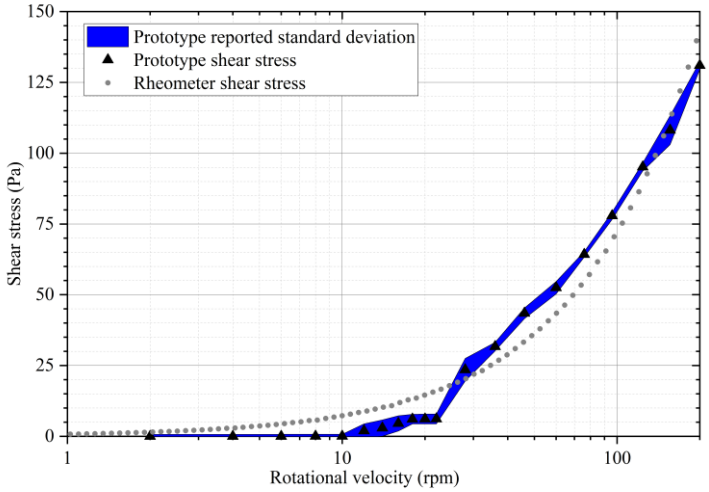

Figure A-10 Final calibration curve of the first prototype using the Vane 2 geometry [115].

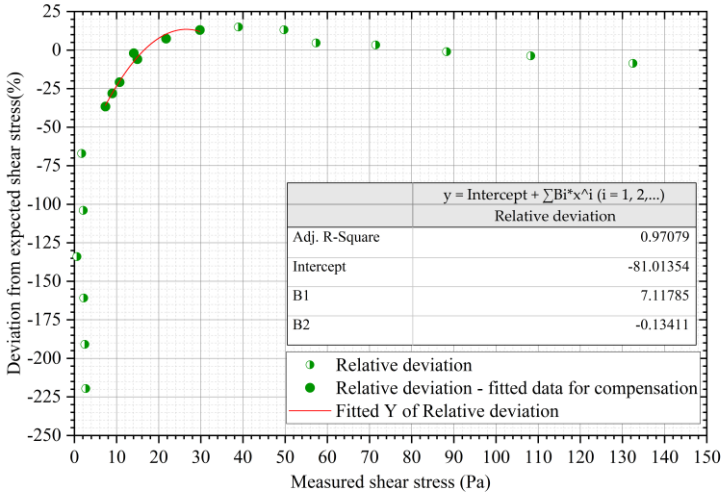

Figure A-11 Compensation curve showing results for Vane 1 including fitted function parameters [115].

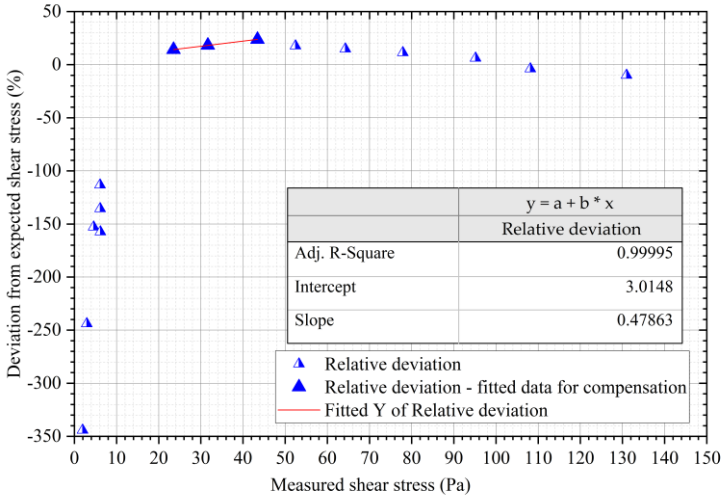

Figure A-12 Compensation curve showing results for Vane 2 including fitted function parameters [115].

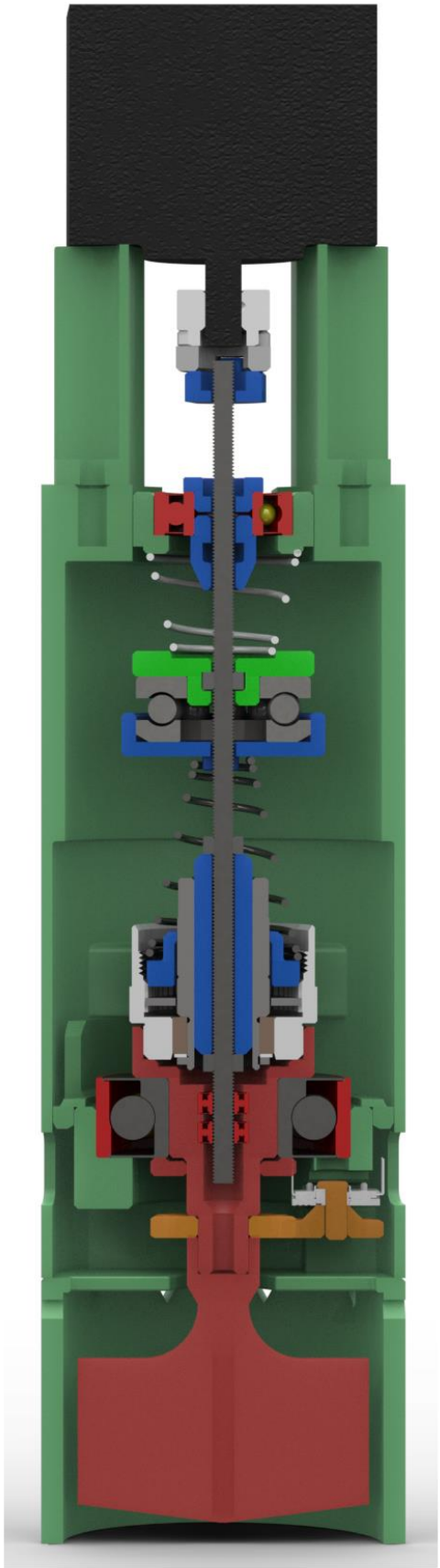

Figure A-13 Model of the shear stress ramp prototype as seen in a cross-section through the centre of the prototype.

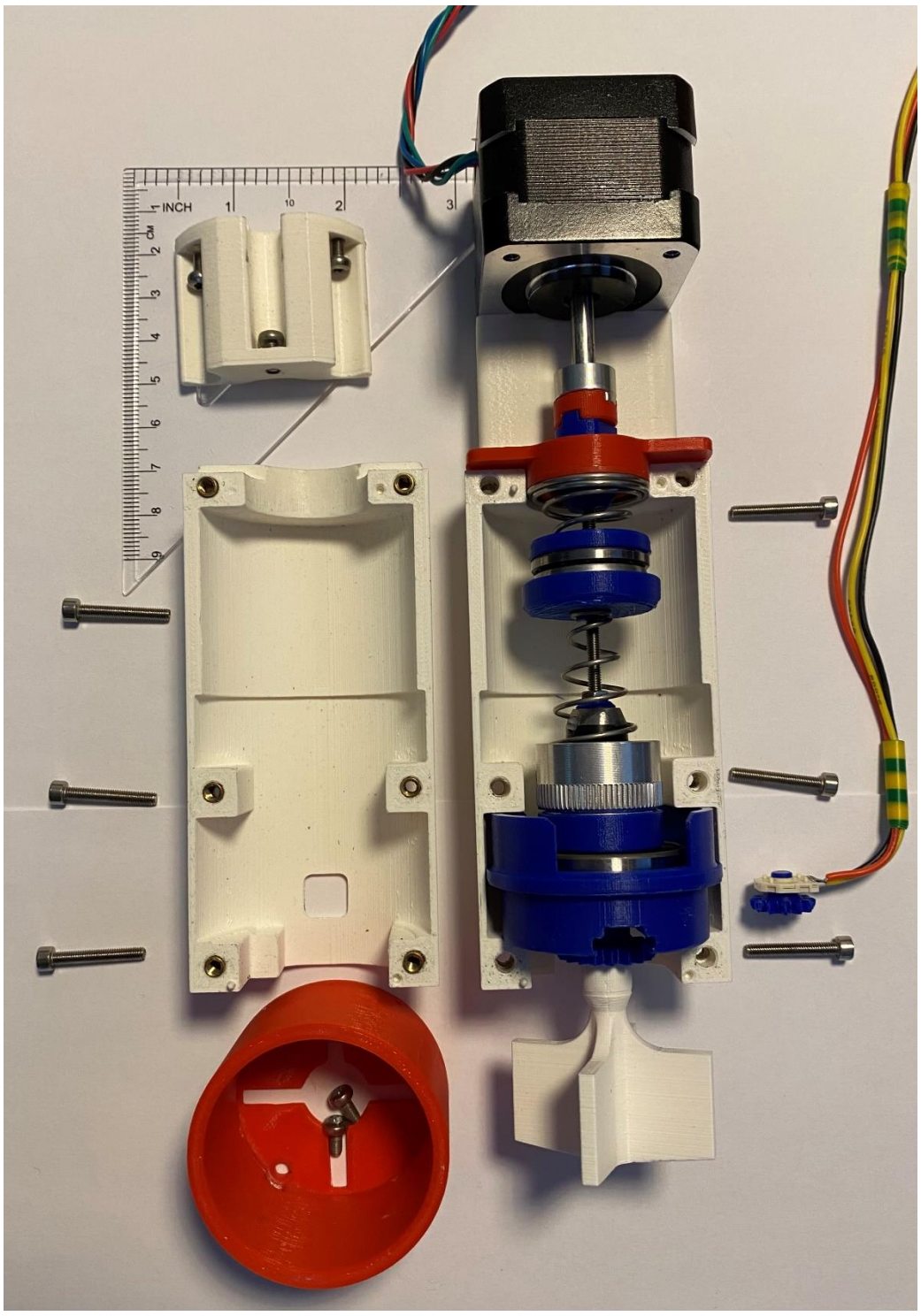

Figure A-14 Partially disassembled shear stress ramp prototype.

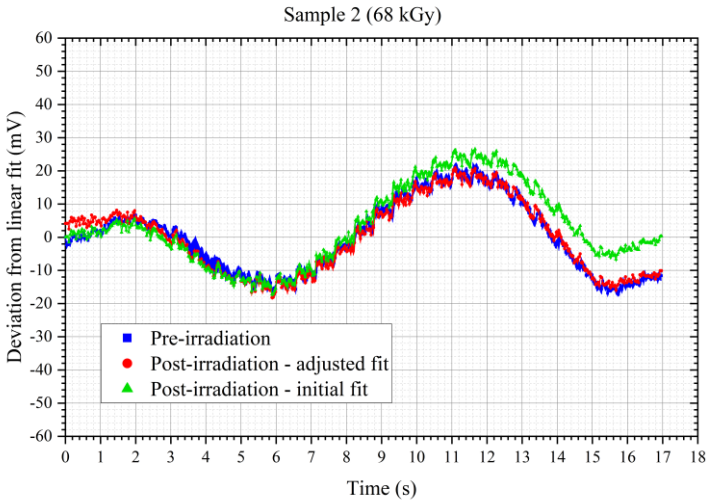

Figure A-15 Continuous turn potentiometer of the shear rate ramp prototype potentiometer radiation testing data – sample 2.

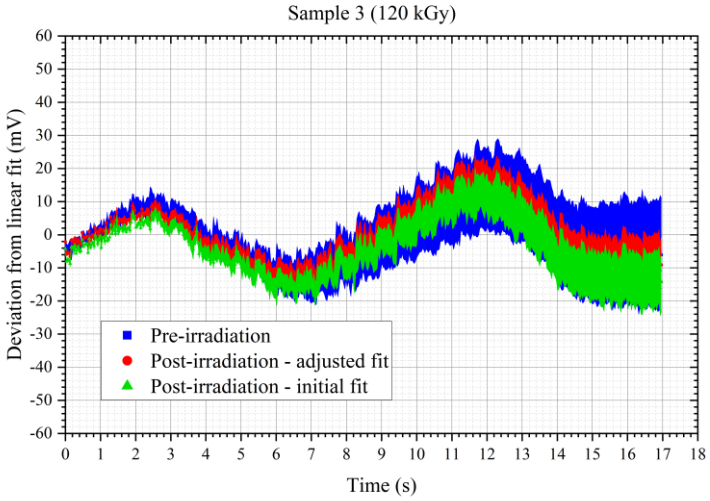

Figure A-16 Continuous turn potentiometer of the shear rate ramp prototype potentiometer radiation testing data – sample 3.

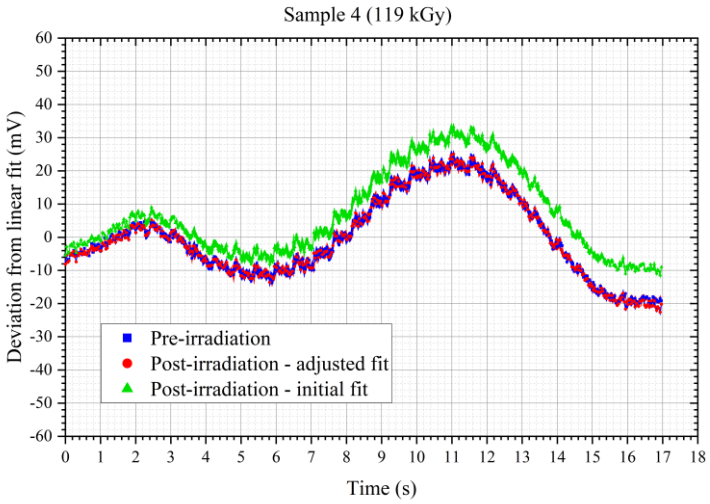

Figure A-17 Continuous turn potentiometer of the shear rate ramp prototype potentiometer radiation testing data – sample 4.

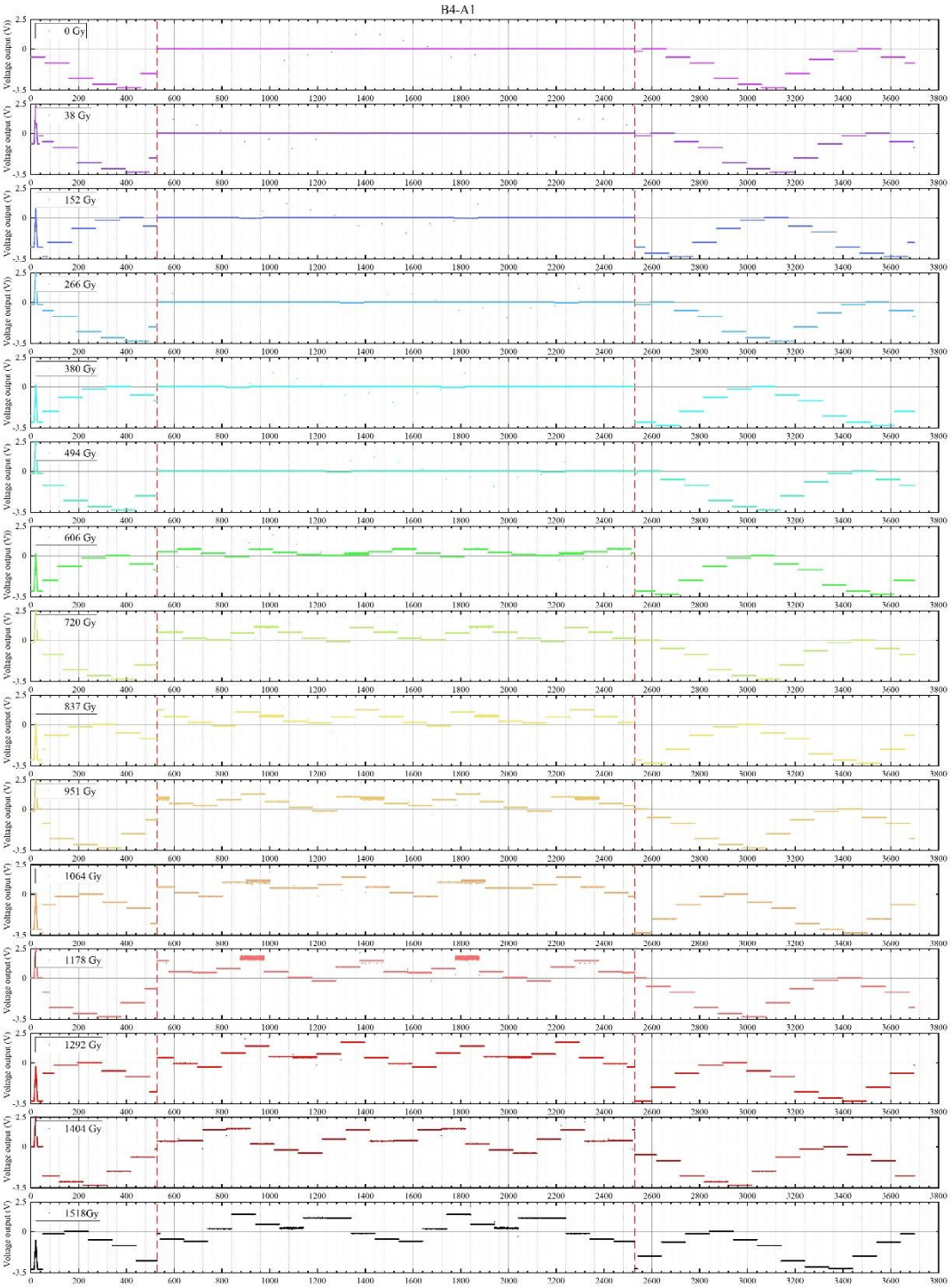

Figure A-18: Difference between voltage recorded on analog pin A1 of the sample B4 and the external reference voltage during the ADC test. Red dashed lines mark the start and end of the ADC test procedure. Between the dashed lines deviation from 0 value indicate incorrect function of the ADC.